PAUL SCHERRER INSTITUT

PSI

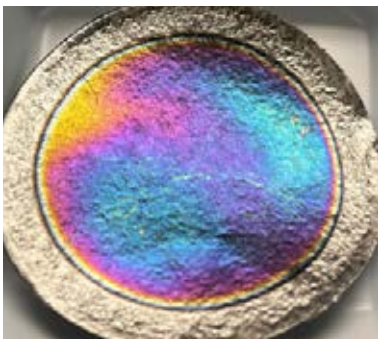

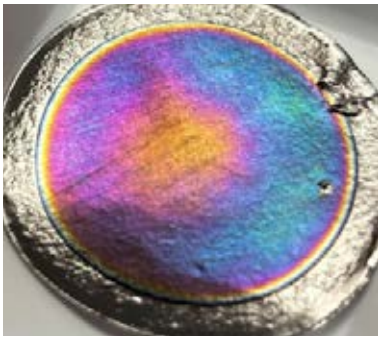

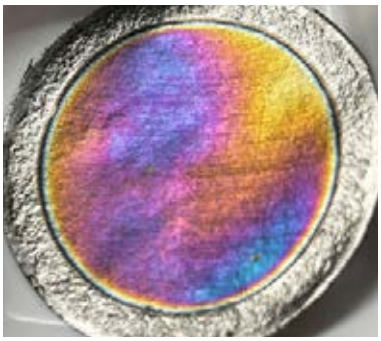

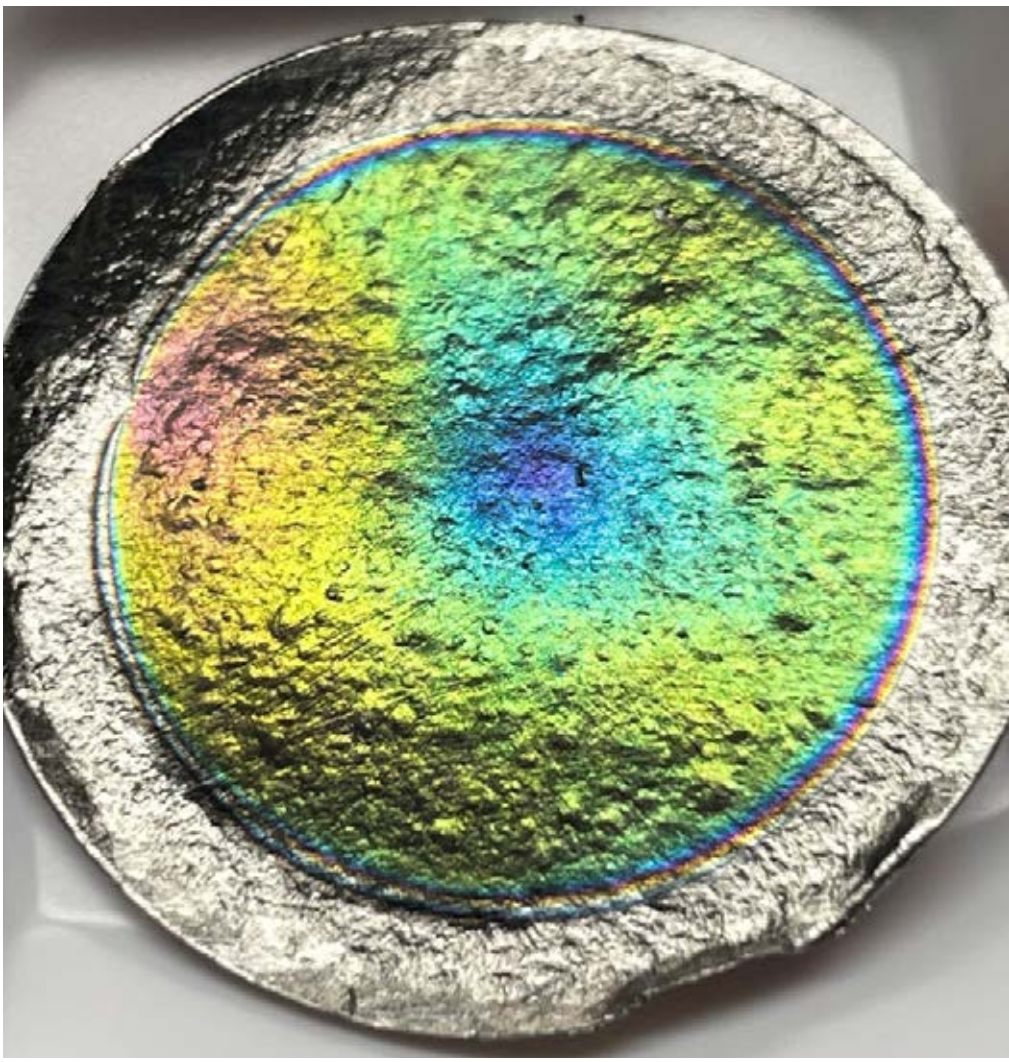

Annual Report 2022

Laboratory of Radiochemistry

Cover

Photographic images of Gd deposits obtained by molecular plating from N,N-dimethyl-formamide containing solutions. The layers are in the nm range and very homogeneous.
For details see the contribution on page 44.

PAUL SCHERRER INSTITUT

PSI

Annual Report 2022

Laboratory of Radiochemistry

Editors
Robert Eichler and Dorothea Schumann

Paul Scherrer Institut
Laboratory of Radiochemistry
5232 Villigen PSI
Switzerland
Secretariat +41 56 310 24 01
Fax +41 56 310 44 35

Reports are available from
Angela Blattmann
angela.blattmann@psi.ch
Paul Scherrer Institut
5232 Villigen PSI
Switzerland

See also our web-page
https://www.psi.ch/lrc/

Table of content

Editorial

R. Eichler (PSI&UniBern)

Dear reader,

The political happenings in year 2022 impacted the world as we knew it quite drastically. The extremely unfortunate and unacceptable warfare situation in Ukraine had significant influence also on some of our prominent scientific collaborations. There were strategic changes needed to keep working on all the scientific topics of LRC.

Please find here the annual report of LRC for the year 2022. It intends to illustrate and summarize the interesting and exciting scientific achievements and ongoing projects of our laboratory. You will find a broad multidisciplinary scientific portfolio of LRC, which is certainly also acknowledged by the motivated young generation. We attracted new bachelor, master, PhD students and Postdocs to work with us. Let me again convey a warm welcome to those who started working with us also in this year.

After the last years of the pandemic impact we all enjoyed finally going back to conferences in person, where the most interesting and collaborative discussions occur after sessions during joint lunches and dinners – much more efficient and rewarding compared to the remote attendances. In September we had the great privilege to host the 30th Conference of the International Nuclear Target Development Society (INTDS) here at PSI. Dorothea and her team did a great organizational job to provide the best environment for fruitful discussions and planned a great frame program. At all these occasions our research work was well represented even with award-winning contributions: Mario, Noemi, Nadine, Chiara and Georg - you were amongst those winners and I would like to congratulate you to the big success, which is also a great PR for LRC and the closely collaborating Center for Radiopharmaceutical Sciences (CRS).

During the recent years, we were heavily involved in preparing the radiochemistry contribution for PSI's IMPACT project recently declared by the ETH council as part of the SBFI's Roadmap of Swiss Research Infrastructures 2025-2028. The project comprises one upgrade of the muon facilities at PSI HIMB and a new radionuclide production station at the HIPA 590 MeV proton beam using spallation in conjunction with ISOL-based mass separation (pioneered at CERN ISOLDE) with the name TATTOOS. Please, have a look at the promises of what is planned here: www.psi.ch/impact.

After the success during the SCIENTIFICA 2021 organized by ETH Zurich, the Swiss radiochemistry was well represented by the members of our laboratory also this year in October during the day of the open door at Paul Scherrer Institute. Here, I would like to sincerely thank everybody who took up the challenge to so nicely explain our work to the general public. From the feedback I got after the event on several occasions, it appears that we were generally recognized as excited and very motivated people enjoying our scientific work and the research opportunities we have here at PSI. So goal achieved - well done!

LRC is considered a positive, lively and great team. Therefore, also our social happenings are always legendary! Organized by Patrick (thank you very much!) during this year's excursion we all got to know the city of Bern from totally unusual points of view during a city-wide Fox-trail challenge. At best sunny weather, we enjoyed the relaxing walks and of course the pauses at famous sightseeing places, e.g at the Rose Garden in Bern and finally the excellent and delicious Okonomiaki vs. Burger dinner at the restaurant Wartsaal. Later this year, our Christmas party took us to the Hotel Linde in Baden, where we enjoyed Bowling and Bingo followed by a great Swiss Fondue. Thank you Nadine for organizing this.

All the scientific and social success is driven by the people of LRC but it would not be possible without the true professionalism of those people at PSI, who help us on a daily basis putting our scientific and technical ideas and dreams into reality. I would like to express mere appreciation to all these people for the unconditional support of our endeavours.

Finally, and most importantly, let us hope that year 2023 brings peace. With the will and the right decisions at the right places, this dream may become reality.

For now again, enjoy reading!

Carrier-free ^{202}Tl from proton-irradiated HgO

J. Wilson (PSI&ETHZ), D. Herrmann (PSI), P. V. Grundler (PSI), N. P. van der Meulen (PSI), A. Sommerhalder (PSI), P. Steinegger (PSI&ETHZ)

Introduction

The current state-of-the-art method to investigate the chemistry of superheavy elements (SHEs) is online thermochromatography. Since SHEs are difficult to produce (low cross-sections) and generally feature short half-lives (single seconds), preparatory offline studies with lighter homologs are key to predict the likely behavior of corresponding SHEs, e.g. studies of Tl to prepare for nihonium (Z = 113) [1,2]. For these preparatory offline studies, it is essential that the desired radioisotopes are produced carrier-free and are separable from the target material. To satisfy these conditions and to utilize facilities available at PSI, carrier-free ^{202}Tl was produced at PSI's IP2 irradiation station through proton irradiation of ^{nat}HgO [3]. The concurrent production of ^{203}Hg, via, e.g. ^{204}Hg(p,pn)^{203}Hg [3] (figure 1), allows both the Hg and Tl fractions to be traced by γ-ray spectroscopy.

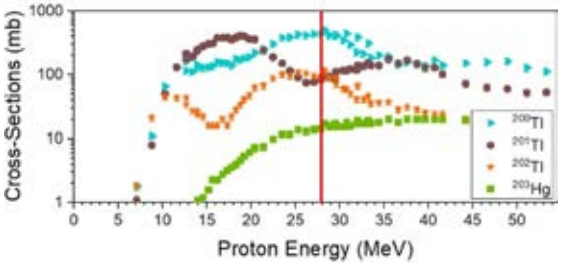

Figure 1. Selected cumulative cross-sections for different radionuclides from proton-irradiated ^{nat}HgO [3]; the red line indicates the herein chosen proton beam energy.

Proton-irradiated ^{nat}Hg can be separated from Tl by liquid-liquid extraction [4]. To avoid the dissolution of the target, the thermal decomposition of HgO into $Hg_{(l)}$ and $O_{2(g)}$ was chosen to separate ^{202}Tl from the bulk of the target material. At a decomposition temperature of around 500°C, elemental Tl remains adsorbed on a Ta surface, i.e. the crucible.

Experimental

For the target, 161 mg ^{nat}HgO was pressed into a disk (diameter: 6 mm, thickness: 0.5 mm) and placed in an anodized Al holder (> 10 µm Al_2O_3-layer; safety precaution). The target was irradiated for 1 min with a ~ 28 MeV proton beam (after Nb-degrader) at an intensity of ≈ 50 µA. After a roughly 3-week cool-down period, the target was transferred to a Ta crucible fitting within a 10 mm diameter quartz column. The target was heated at 525°C for 2 h under a 50 mL/min Ar gas flow, causing Hg to settle on the column outside the oven and leaving ^{202}Tl in the Ta crucible. In preparation of a thermochromatographic experiment, the Ta crucible with ^{202}Tl was heated in a second column for 3 h at > 900°C under a 50 mL/min Ar gas flow. The volatilized ^{202}Tl was then captured on a Ta liner beyond the oven.

Results and Discussion

The determined activities after proton irradiation were 228(5) kBq and 6.6(1) kBq for ^{202}Tl and ^{203}Hg (figure 2, spectrum 1), respectively. These values were about one order of magnitude lower than the calculated activities of 1710(210) kBq and 83(14) kBq, for ^{202}Tl and ^{203}Hg, respectively (likely due to the short irradiation time).

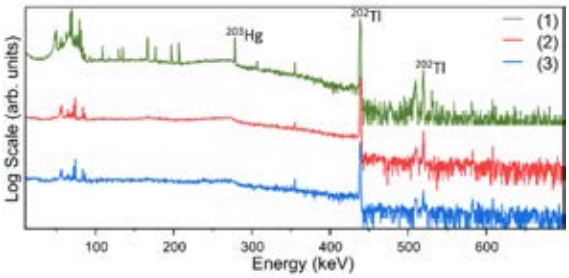

Figure 2: HPGe γ-spectra of the Ta crucible (1) before Hg-Tl separation with the target, (2) after Hg-Tl separation, and (3) after Tl transfer to the Ta foil.

The separation of ^{202}Tl from ^{203}Hg was successful (see figure 2, spectrum 2). However, a portion of ^{202}Tl was measured in the Hg fraction. 81% of ^{202}Tl could be transferred to the Ta liner (see figure 2, spectrum 3).

It should be noted that this was only a preliminary study, thus, there are still losses with each step. However, this method successfully provides carrier-free ^{202}Tl by means of a gas-phase separation of elemental Tl from the HgO target.

Acknowledgements

This project was funded by the Swiss National Science Foundation (no. 200020_196981).

References

[1] A. Serov et al., Radiochim Acta, 101 (2013).
[2] J. Wilson et al., Annual Report (2021) pp 10-11.
[3] A. Hermanne et al., Nucl Instrum Meth B, 378 (2016).
[4] B. Dutta et al., Appl. Radiat. Isotopes, 69 (2011).

Using 4H-SiC PIN-diodes for α-Spectroscopy up to 500°C and beyond

J. Wilson (PSI&ETHZ), G. Tiebel (PSI&ETHZ), M. Camarda (SenSiC), R. Dressler (PSI), D. Herrmann (PSI), P. Steinegger (PSI&ETHZ)

Introduction

A well-established method for the chemical characterization of superheavy elements (SHEs) is gas-phase adsorption thermochromatography. This method has proven successful to address radionuclides of SHEs with half-lives down to single seconds and at the one-atom-at-a-time level. Recently, the interest has shifted towards nihonium (Z=113), whose chemical species are predicted to be less volatile compared to Cn (Z=112) and Fl (Z=114) [1]. In an online thermo-chromatography experiment, this translates to a higher starting temperature of the negative temperature gradient. As the chromatography channel consists of α-detectors (i.e. their surface acts as the stationary phase in the chromatographic process), they need to cope with these increased temperature requirements. Thus far, Si PIN-diodes have been used [2], which are limited to temperatures below 50°C. However, wide bandgap semiconductors, such as 4H-SiC, are promising alternatives.

Within the past few decades, 4H-SiC has rapidly developed into an intensively investigated material for harsh radiation and temperature environments [3,4]. Because of its 3.3 eV band gap, 4H-SiC is able to operate at high temperatures [5,6]. Here, we present a series of measurements showing for the first time that an α-particle-induced stable analog signal can be extracted from 4H-SiC sensors up to 500°C and 700°C.

Experimental

All experiments were carried out *in vacuo* at pressures below 10^{-4} mbar. The 4H-SiC PIN-diodes were used as received (see figure 1, right side): Ag-soldered onto and wire-bonded to a TO-3 package for handling and operation. A custom-made Cu-enclosure was made to fit two heating cartridges, a thermocouple, and the TO-3 package with the sensor (see figure 1, left side). Aligned to the sensor was a ^{241}Am source. A charge sensitive Cx-L spectroscopic amplifier from Cividec Instrumentation GmbH was used for biasing (-150 V; Keithley 2470) and signal extraction (pulse height analysis, PHA). The waveform of individual pulses were recorded using a Tektronix Mixed Signal Oscilloscope (MSO46) with 12-bit voltage resolution and 250 MS/s sampling rate. Due to the rather thin depletion thickness of 10 µm, only a fraction of the initial α-energy was deposited in the depletion zone. This prevents quantitative α-spectrometric measurements.

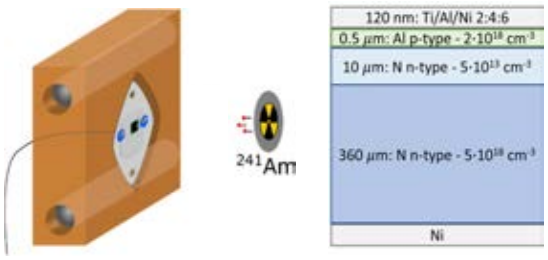

Figure 1: Left, schematic of detector setup within the Cu-enclosure with the thermocouple, 2 heating cartridges, and the TO-3 package with the sensor; right, schematic structure of the 4H-SiC PIN-diode including the metal contacts.

Two 4H-SiC-based detectors from two different batches were examined. Whereas detector 1 (batch one) was wire-bonded with Au, detector 2 (batch two) was Al-wire-bonded. Detector 2 featured improvements of the termination of the device boundaries and of the metal-to-SiC contact. Each detector was subjected to a step-wise heating protocol:

Detector 1) Heating in steps of 100°C up to 700°C (one experiment)

Detector 2) Heating in steps of 100°C up to 500°C with intermittent measurements at room temperature (two experiments)

The amplitudes of the progression of analog signals (PHA) as a function of temperature and time are reported here. The detector stability over time at high temperatures was addressed as well as repeated cycling from room temperature to these high temperatures.

Results & Discussion

Detector 1 showed a stable performance up to 300°C before deteriorating with each subsequent temperature increase (see figure 2). Besides the measurements at 400°C, the signal response remained constant within each temperature set-point. It is important to note, that even at 700°C a reduced but stable signal was recorded over the course of 48 h. The amplitudes of the analog signal recovered to their original magnitude once cooled to room temperature.

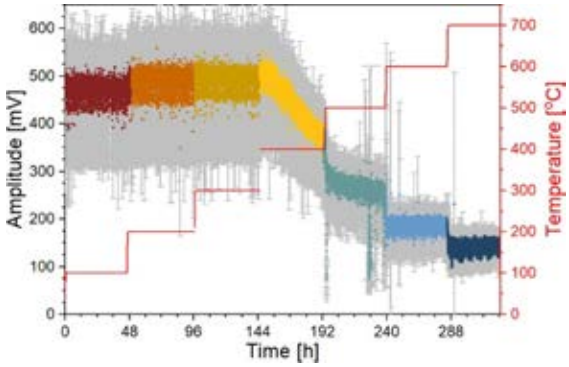

Figure 2. Amplitudes of the measured progression of analog signals as a function of the elapsed time and the applied temperature of detector 1. Change in color references an increase in temperature (right axis in red); note every point is an average of 10 traces.

The adjustments made to the second batch substantially improved the performance (see figure 3). Although not shown, the detector temperature was decreased to room temperature for 8 h after every 24 h at an elevated temperature. The slight drift in the signal amplitude will be addressed in future experiments or detector designs, respectively.

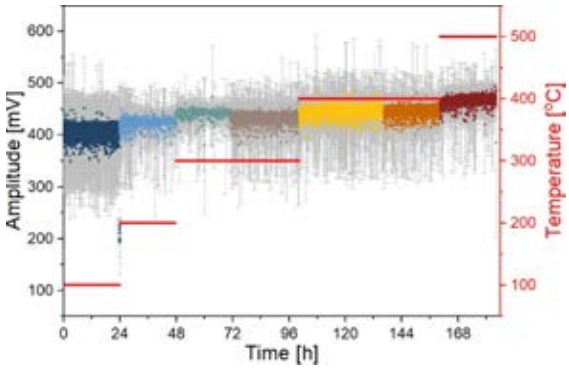

Figure 3. Amplitudes of the measured progression of analog signals as a function of the elapsed time and the applied temperature of detector 2. The measured signal amplitudes at room temperature between each temperature step (i.e. different colors; see right axis in red) are not shown; note every point is an average of 10 traces.

For quantitative α-spectroscopy with extrinsic semiconductor-based detectors, all α-particles must be stopped within the depletion zone (i.e. the lighter doped area; see figure 1, right side). As the herein used sensors have a rather small depletion layer of only 10 µm, 5.485 MeV α-particles from the ^{241}Am are only fully stopped in the heavier n-doped layer of the sensor (i.e., the substrate) beyond the depletion zone. In order to test the performance with α-particles fully stopped within the depletion zone, a 16 µm Al degrader was added to the experimental setup. Hereto, calculations with SRIM [7] indicated an implantation depth of the degraded α-particle of roughly 6 µm (i.e. within the depletion zone).

As expected, the measured signal amplitudes were comparatively reduced due to less energy being deposited in the sensing layer itself. Regardless, the performance of detector 2 was not only fully reproducible over individual experiments up to 500°C (figure 3), but lacked any drift up to 500°C (see figure 4).

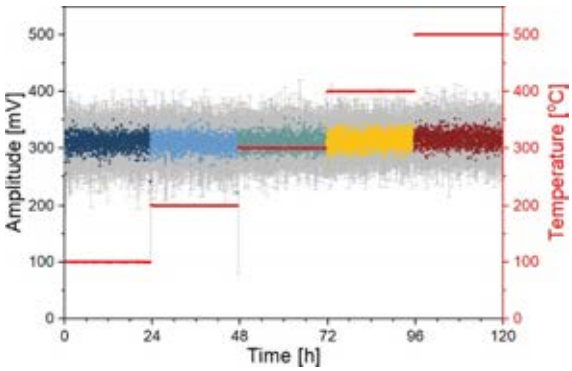

Figure 4. Amplitudes of the measured progression of analog signals as a function of the elapsed time and the applied temperature of detector 2 with a 16 µm Al degrader between the detector and the ^{241}Am source. The temperature is noted on the y-axis on the right side in red. Every point is an average of 10 traces.

In conclusion, 4H-SiC-based detectors can be operated up to 500°C without any degradation of their performance. Repeated and prolonged measurements confirmed the reliability of the detector with time and temperature.

Acknowledgements

This project was funded by the SNSF grant no. 200020_196981. Thank you to Silvan Streuli for wire-bonding the detectors multiple times.

References

[5] V. Pershina et al., Inorg Chem, 60 (2021).
[6] R. Eichler et al., Nature, 447 (2007).
[7] S. Sciortino et al., Nucl. Instrum. Meth. A., 552 (2005).
[8] J. Casady et al., Solid State Electron., 39 (1996).
[9] G. Tiebel et al., LRC Ann. Rep. (2021) pp 5-6.
[10] C. Wiess et al., Nucl. Instrum. Meth. A., 1040 (2022).
[11] J. Ziegler, Nucl. Instrum. Meth. B., 219-220 (2003).

First test of large area 4H-SiC-based detectors for α-spectroscopy

G. Tiebel (PSI&ETHZ), M. Carulla Areste (PSI), M. Carmada (SenSiC), R. Dressler (PSI), P. Steinegger (PSI&ETHZ), J. Wilson (PSI&ETHZ)

Introduction

Gas-phase adsorption chromatographic techniques enable the chemical characterization of transactinide elements ($Z \geq 104$). These elements are of particular interest for understanding the impact of relativistic effects [1]. A reliable and fast, event-by-event detection is a prerequisite to detect the associated short-lived radionuclides mainly decaying by α-emission. Detection of α-particles occurs either directly inside the chromatographic channel (thermo-chromatography), with the sensor surface of the detectors acting as the stationary phase, or at the end of an isothermal chromatography column in the form of an escape detector. Both types of employment require large area detectors covering a wide temperature range. State-of-the-art detectors for α-spectroscopy are Si-PIN diodes, however, lacking the applicability over a wide temperature range (maximum operation temperature around 50 °C). Single-crystal, chemical vapor deposited (scCVD) diamond-based detectors were successfully tested regarding their α-spectroscopic performance at elevated temperatures up to 500 °C [2-3]. However, scCVD diamonds are limited in available surface areas (i.e., 5x5 mm^2. Meanwhile, 4H-SiC-based detectors show superior properties in high-temperature applications [4] and, at the same time, have little to no restrictions in terms of available surface areas.

Here, we present the first spectroscopic measurements using 4H-SiC-based detectors with an increased active area at room temperature.

Experimental

Herein, measurements with large area 4H-SiC sensors, each with a size of 12x12 mm^2, are presented (see Tab. 1). The sensors were mounted on a custom-made printed circuit board (PCB) featuring a collimating hole with a diameter of 2 mm and placed in vacuum.

The front side of the detector facing the PCB was contacted to ground via a dedicated metal pad on the carrier. A three-line α-source (^{239}Pu, ^{241}Am, and ^{244}Cm) was placed on the back of the PCB carrier opposite the collimator at 10 mm 10 from the PCB. A copper spring, connecting the backside of the sensor to a separate metal pad on the PCB carrier, served as the contact for applying the positive bias voltage and the signal extraction (electrons). Different bias voltages were applied and the resulting spectroscopic response was measured using a charge-sensitive Cx-L spectroscopic amplifier from Cividec Instrumentation GmbH (CxL0075, 1.1 µs shaping time). A Hexagon (CAEN) multi-channel digital analyzer recorded the pre-shaped signals by trapezoidal fitting and subsequent readout of the plateau to an evaluation software. Each experiment with one bias voltage was conducted over at least a measurement time of 24 h.

Table 1: Structure of the sensors from the front side (metallization) to the backside.

Layer	Metals/ Dopant	Procedure/ Concentration
Metallization	Ti (20 nm) / Al (40 nm) / Ni (60 nm)	1 min at 950 °C
1	Al; p-type epitaxial (0.5 µm)	$2 \cdot 10^{18}$ cm^{-3}
2	N; n-type epitaxial (100 µm)	$5 \cdot 10^{13}$ cm^{-3}
3	N; n-type substrate (360 µm)	$5 \cdot 10^{18}$ cm^{-3}

Results and discussions

Spectroscopic measurements with the large-area 4H-SiC sensors resulted in baseline-separated spectra for the main emission peaks of the three-line α-source with reasonable spectroscopic resolutions of the individual peaks (see figure 1). The resolution (full width at half maximum) was determined by fitting the peaks using an exponentially modified Gaussian (one exponential tailing parameter) [5].

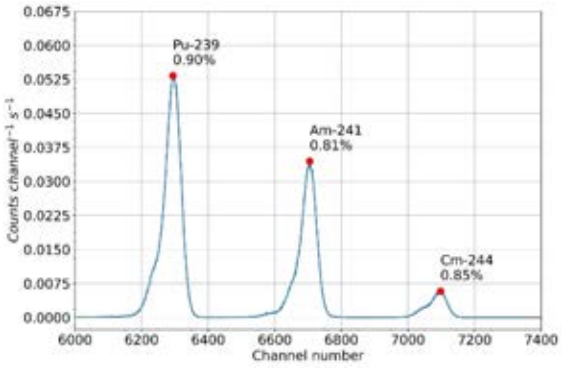

Figure 1: Example spectrum measured with a large area 4H-SiC-based detector at the lowest energy resolution at a bias voltage of + 120 V.

Expectedly, an increasing bias voltage leads to a steady increase in the channel numbers of the centroid position for all α-lines since the device is not fully

depleted (see figure 2). A higher bias voltage leads to an increasing depletion thickness, thus, allowing for an increased energy deposition in this layer [6]. This in turn leads to a higher charge carrier generation. The saturating shift in channel numbers at a higher bias voltage (> 150 V) indicates complete depletion of the sensor.

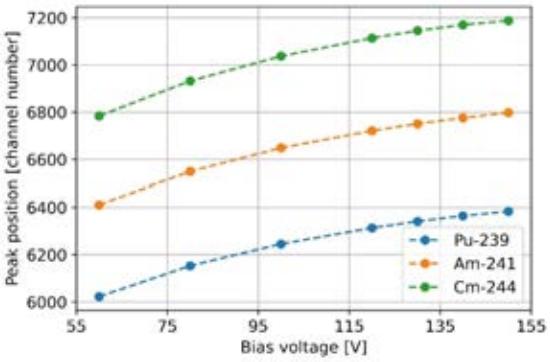

Figure 2: Peak position (measure of the energy of the energy of the impinging α-particles) as function of the applied bias voltage.

The resolution decreases as a function of the applied bias voltage due to an overall improved charge carrier collection (see figure 3). The minimum spectroscopic resolution of 0.81% (44 keV) was determined at a sensor bias voltage of + 120 V. The anew increase in resolution that occurs at bias voltages above beyond the optimum suggests electrical contacting problems on the custom-made PCB.

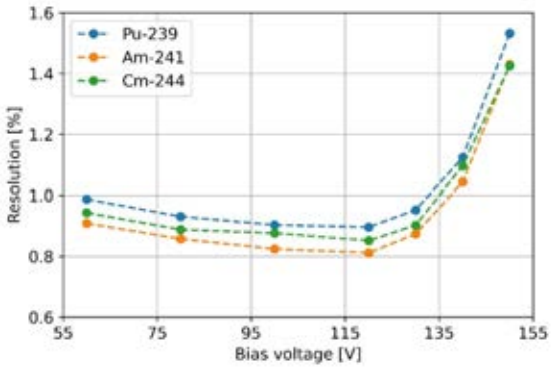

Figure 3: Spectroscopic resolution as a function of the applied sensor bias voltage.

The herein presented experiments render large area 4H-SiC-based detectors suitable for α-spectroscopy. The carrier structure requires further development to sustain higher sensor bias voltages. These large area sensors will be employed in an adsorption chromatography experiment *in vacuo* as an escape detector.

References

[1] A. Türler, V. Pershina, Chem. Rev. 113, 1237-1312 (2013)
[2] B. Kraus et al., Nucl. Instrum. Methods Phys. Res., Sect. A 989, 164947 (2021)
[3] C. Weiss et al., Nucl. Instrum. Methods Phys. Res., Sect. A 1040, 167182 (2022)
[4] J. Wilson et al., LRC Annual Report 2022, p. 4 (2023)
[5] G. Bortels, P. Collaers, Int. J. Radiat. Appl. Instrum. Part A 38, 831-837 (1987)
[6] M. Jotterand et al., LRC Annual Report 2020, 9-10 (2021)

The Big RTC at Texas A&M University as an interface for vacuum-chromatography experiments – a feasibility study

G. Tiebel (PSI&ETHZ), R. Eichler (PSI&UniBern), C. M. Folden III (TAMU CI&TAMU Chem), D. Herrmann (PSI), A. Kirkland (TAMU CI&TAMU Chem), P. Steinegger (PSI&ETHZ), E. Tereshatov TAMU CI)

Introduction

The investigation of the chemical properties of heaviest elements (transactinide elements, Z ≥ 104) is limited by the low production cross sections (one-atom-at-a-time approach), the short half-lives, and the adsorption behavior of associated chemical species on certain surfaces. Vacuum adsorption chromatography (VAC) is expected to address radioisotopes with half-lives in the millisecond regime, while, at the same time, providing generally cleaner process conditions due to the absence of a carrier gas. However, performing an experiment with nuclear reactions products (NRPs) *in vacuo* after a physical pre-separation raises a major problem, namely, the stopping (i.e. the thermalization) of NRPs prior to the chemical experiment. The direct implantation of the NRPs with kinetic energies in the MeV-range complicates their subsequent characterization due to release-kinetics-related losses caused by comparably deep implantations in a stopping matrix. Meanwhile, the shallow implantation of NRPs with kinetic energies in the keV-range in a hot catcher was successfully used to determine the gas adsorption behavior of thallium (Tl, Z = 81) on fused silica, yielding an adsorption enthalpy of $-\Delta H_{ads}^{SiO_2} = 158$ kJ mol^{-1} [1]. These studies were carried out in preparation of the chemical characterization of the heavier homolog of thallium in group 13 of the periodic table, i.e. nihonium (Nh, Z = 113). An alternative to a direct implantation is the use of a so-called gas buffer cell (GBC) to thermalize incoming NRPs through multiple interactions with a buffer gas and to guide the remaining ions towards an exit by means of electrostatic and gas velocity fields. The transition to vacuum is established through differential pumping. The GBC, equipped with a DC-only ion-beam-forming unit, is available at the Heavy Elements group of the Cyclotron Institute at Texas A&M University, USA [2].

Here, we present the results of offline experiments in which the above-mentioned Recoil Transfer Chamber (Big RTC) was tested for its suitability for a transfer at high differential pressures. These served as exploratory studies for a later envisaged IVAC experiment, requiring a transition from ≈ 100 Torr for an optimum stopping of incoming NRPs to a pressure regime of ≈ 1·10^{-4} Torr (molecular flow conditions met, i.e. the mean free path exceeds the critical dimensions of the experimental setup).

Experimental

A ^{228}Th source (25 kBq, electrodeposited and diffusion-bonded oxide on Pt backing) was placed in the high-pressure chamber of the Big RTC (see figure 1). Short-lived, positively charged ^{216}Po ($t_{1/2}$ = 144 ms) was volatilized through the prior escape and α-decay of the randomly distributed mother, ^{220}Rn ($t_{1/2}$ = 55 s), within the high-pressure chamber of the Big RTC. The ^{216}Po-ions were then guided by a DC field (i.e. established by 4 ring and 4 petal electrodes) towards the nozzle. In the low-pressure chamber (see figure 1, right side), the ions were envisaged to be extracted from the simultaneously pumped excess gas, using a Ni grid, to which a high voltage of up to -12 kV could be applied. This grid was mounted in front of a Si-PIN-detector for the detection of the α-decay of deposited ^{216}Po.

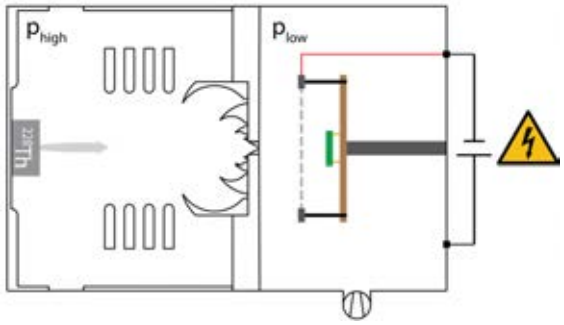

Figure 1: Experimental setup with ^{228}Th source, DC electrodes for guiding, high-voltage mesh, and the Si-PIN-detector.

To achieve larger differential pressures, the nozzle size was reduced using Kapton tape (see figure 2). The best differential pressure, meeting both mentioned requirements, was achieved with a cone-shaped funnel modification (see brown curve in figure 2).

Results and discussion

With different differential pressures between both chambers, the highest transport yield was observed at a pressure difference of 50/19 Torr (see figure 3). Two types of α-particles can be distinguished: α-particles originating from ^{216}Po-decays within the main chamber as well as those occurring on the detector (i.e. transported ^{216}Po ions). The first kind is only possible at low pressures, since only at those pressures α-particles reach the detector. Meanwhile, the transport of the short-lived ^{216}Po is gas-flow dependent, thus, requiring

a minimum pressure difference between both chambers of the Big RTC. The number of radionuclides transported directly increases with increasing pressure difference, i.e. increasing gas flow.

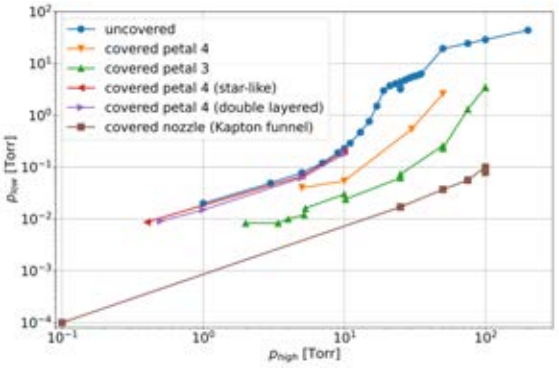

Figure 2: The pressure in second chamber (p_{low}) as a function of the pressure in main chamber (p_{high}); the plot shows a comparison of different types of Kapton tape-based coverages of the nozzle or last petals.

From a certain pressure onwards, an increasing splitting into two α-energies was observed (see figure 3). This is a result of the increasing attenuation of α-particles incident from within the main chamber by an increasing number of gas interactions. The constant presence of the peak at an α-energy of 6.8 MeV indicates a direct transport of ^{216}Po after passing an initial threshold with molecular flow conditions and peaking at the above-mentioned pressure difference of 50/19 Torr. In a second step, a voltage was applied to the Ni mesh to evaluate the extraction of ^{216}Po-ions from the main chamber at a high differential pressure $25/2.1 \cdot 10^{-2}$ Torr.

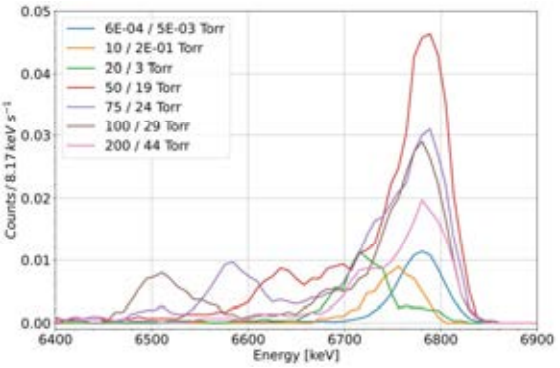

Figure 3: Transport of ^{216}Po at varied differential pressures (p_{high} / p_{low}); no voltage was applied to the Ni mesh.

Seven different voltages were applied to the mesh resulting in no measurable increase of transported ^{216}Po from the main chamber (see figure 4, black arrow). The Paschen effect [3] limited the further increase of the high voltage, which could have possibly increased the extraction yield of ^{216}Po from within the high-pressure chamber.

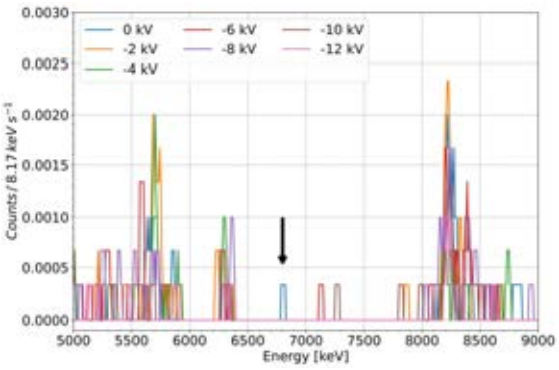

Figure 4: The transport of ^{216}Po in dependence of the applied extraction voltage on the Ni mesh; the black arrow indicates the α-energy of ^{216}Po.

In summary, the Big RTC in its current state is not suitable as an interface for a transfer of NRPs into a high vacuum apparatus. The achieved differential pressure was largely limited by the pumping power. Since major adjustments of this GBC would be necessary to fulfil the prerequisites for a VAC experiment, the focus has since shifted towards a dedicated development of a RF-GBC with a high-capacity differential pumping stage (100 mbar to 0.01 mbar). The new setup will be tested during an online experiment at the Cyclotron Institute (TAMU CI). These experiments aim at proving the capabilities of VAC in terms of attainable fast transport speeds with differently short-lived radioisotopes of mercury, i.e. using the nuclear reaction ^{144}Sm(^{40}Ar,xn)$^{184-x}$Hg [5]. The produced mercury radioisotopes with half-lives ranging from 0.02 s to 11 s have a low adsorption enthalpy on fused silica ($-\Delta H_{ads}^{SiO_2} = 40$ kJ mol^{-1} [4]), which simplifies the thermal part of operation of this proof-of-concept experiment.

References

[1] P. Steinegger et al., J. Phys. Chem. C 120, 7122-7132 (2016)
[2] M. C. Alfonso et al., Nucl. Instrum. Methods Phys. Res., Sect. A 798, 52-61 (2015)
[3] F. Paschen, Ann. Phys. 273, 69-96 (1889)
[4] S. Soverna, Attempt to Chemically Characterize Element 112, Universität Bern, (2004)
[5] D. Kamas et al., Phys. Rev. C 105, 44612 (2022)

Assessment of an ion-funnel-to-VAC system

G. Tiebel (PSI&ETHZ), P. Steinegger (PSI&ETHZ)

Introduction

Vacuum chromatography (VAC) is envisaged to be a fast and clean technique to investigate the chemical properties of heaviest transactinide elements (Z ≥ 104) with shortest-lived radioisotopes [1]. The transfer of nuclear reaction products (NRPs) from heavy-ion-induced nuclear fusion evaporation reactions behind a physical pre-separator into an evacuated environment requires a special interface, which allows for the thermalization and further provision of the remaining, charged NRPs. A preliminary experiment at Texas A&M University to determine the suitability of such an interface (Big RTC) revealed that a custom design is necessary [2]. More broadly used designs are so-called gas buffer cells (GBC), which commonly consist of a forward driving DC gradient and a focusing radio frequency (RF) ion funnel. The subsequent transport through a small nozzle (d_{min} = 0.6 mm) arises from the pressure difference between two separated chambers in front and after this orifice. The differential pressure causes the formation of a supersonic jet after the nozzle constriction towards the low-pressure side. Thereafter, an RF quadrupole (RFQ) guides the emerging ions further on (separation of the buffer gas from the ionic NRPs) [3-5].

Various software packages allow for the description of the transport of ions in electric and magnetic fields. These may be superimposed with computational fluid dynamics (CFD) calculations, thus, accounting for, e.g. temperature, pressure and velocity fields of a carrier gas. Here, we combine CFD calculations using COMSOL Multiphysics [6] with ion optical simulations accessible through the SIMION® software package for the simulation of a dedicated GBC for a VAC experiment. The modelling with SIMION® includes collision effects (e.g. with gas atoms and molecules) [7].

General parameters

All simulations were performed with 1000 ions of mass 178 u and a +2 charge state [8,9] distributed over a circular entrance plane with a diameter of 70 mm. The initial kinetic energy of each ion was estimated to be approximately 4 MeV, which is a reasonable assumption for the average kinetic energy of evaporation residues exiting a gas-filled physical pre-separator in the focal plane and penetrating through a 4 μm thin Ti-foil [10, 11]. The DC voltages of the first six ring electrodes decreased from 250 V (closer to the entrance) to 150 V (closer to the nozzle). A DC gradient between 100 V (electrode 1, large opening) and 60 V (electrode 41, small opening), superimposed with a 1 MHz RF bias of 100 V_{pp} (voltage peak-to-peak), was applied to the funnel electrodes, thus, guiding the ions towards the exit of the high-pressure chamber at 50 mbar. The bias voltage of the nozzle was kept at 62 V to avoid wall collisions of inbound ions. Meanwhile, 50 down to 45 V were applied to the electrodes in the second, low-pressure part of the setup to ensure transport towards a second orifice mimicking the entrance of, e.g. a VAC setup.

As a buffer and carrier gas, He was chosen due to its comparatively high ionization potential (i.e. minimizing neutralization losses of NRPs). Three different target pressures were defined for three different parts of the assembly (i.e. 100 mbar → $1{\cdot}10^{-2}$ mbar → $1{\cdot}10^{-4}$ mbar see figure 1).

Results and discussions

First SIMION® simulations considered only a transport driven by electric fields. No transport of ions through the orifice could be observed (see figure 1). This emphasized the importance of the supersonic jet at the nozzle, where the influence of the gas transport exceeds the driving force of the electric field.

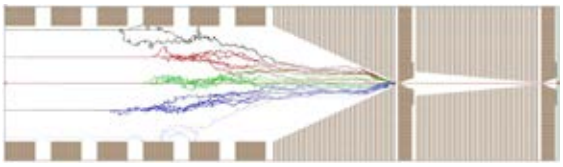

Figure 1: First simulation run considering an ion optical transport established by means of electric fields only; for reasons of simplicity, the trajectories of five ions from five starting points are shown.

The required pressure and flow fields for the given assembly were generated using the turbulent flow module of COMSOL (see figure 2). These were simulated using the mentioned pressure levels as boundary conditions. Furthermore, the immediate nozzle region was simulated with the high Mach number module, resulting in the expected supersonic gas velocities past the nozzle constriction (see figure 3). It is stressed here, that this simplification is part of the herein presented preliminary simulation approach.

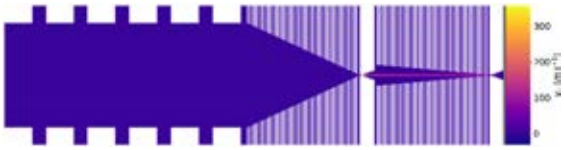

Figure 2: Exemplary heat map of the gas velocity as obtained with the turbulent flow model of COMSOL.

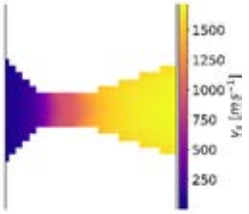

Figure 3: COMSOL simulation with the high Mach number model resulting in supersonic gas velocities in the nozzle region (≈1800 ms^{-1}).

The velocity field, as derived with the turbulent flow model, was scaled to match the supersonic velocities in the nozzle. Without the supersonic velocities within the nozzle, no transport was observed, hence highlighting once more the dominating gas-based transport over the electrostatically driven transport at this point of the setup. The formation of a supersonic gas jet requires a certain pressure difference, which is insufficient in the first experimental setting (figure 1). The eventual transfer to a VAC experiment behind a second nozzle is determined by the voltage applied to this orifice, necessitating an adjustment of its diameter to 2 mm.

SIMION® supports customization using the Lua programming language. Two scripts are readily available that implement two different gas interaction models, i.e. a diffusion-based one and hard-sphere collisions. The "statistical diffusion simulation" (SDS) model requires pressures around atmospheric conditions and superimposes random jumps within the gas (diffusion in gas) at the drift location (electric field) of the ions, thus, resulting in adjusted directional vectors. Meanwhile, the "hard-sphere collision" model (HS1) is based directly on the eponymous kinetic theory model, which describes a neutral background gas and individual collisions therein with gas atoms and/or molecules. Therefore, the computational effort for this second model is considerably higher. Since a suitably high pressure is given in the first part of the setup, the entire assembly was divided into different sections: The SDS model was used up to the last ring electrode of the ion funnel and the HS1 model thenceforth to minimize the computational time.

These two models and the adjustments described above were applied in a final simulation run resulting in the successful transport of the ions from the start and attenuation to the very end of the setup after appropriate ion optical focusing (see figure 4).

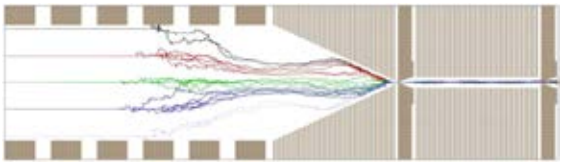

Figure 4: Final simulation run accounting for electronic transport, transport by supersonic gas-jet and increased diameter of the second orifice.

The simulated transport time ranged from ≈ 5-30 ms with an energy decrease from 4 MeV to ≈2-5 eV (at the second nozzle).

These simulations initiated the further development of a GBC for the stopping of NRPs and their subsequent, fast transfer into vacuum. Therefore, such a GBC shall be used as an interface between the focal plane of a separator and a VAC experiment. Further simulations will be directed towards the development of a customized system including a RFQ in the second part of the chamber (see figure 5). In addition, more sophisticated simulations are planned to refine especially the COMSOL simulations, since a description of large systems featuring high Mach numbers has proven to be very difficult to converge.

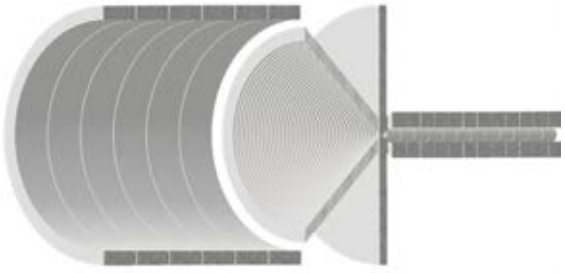

Figure 5: Sketch of the final system to be built.

References

[1] P. Steinegger et al., J. Phys. Chem. C 120, 7122-7132 (2016)
[2] Tiebel et al., LRC Annual Report 2022, p.8 (2023)
[3] J. B. Neumayr et al., Nucl. Instrum. Methods Phys. Res. Sect. B Beam Interact. Mater. At. 244, 489-500 (2006)
[4] C. Droese et al., Nucl. Instrum. Methods Phys. Res. Sect. B Beam Interact. Mater. At. 338, 126-138 (2014)
[5] V. Varentsov, A. Yakushev, Nucl. Instrum. Methods Phys. Res., Sect. A 1010, 165487 (2021)
[6] COMSOL Multiphysics 6.0
[7] SIMION® 2020, v. 2021-06-26-8.2.0.11, simion.com
[8] J. Khuyagbaatar et al., Phys. Rev. A 88, 42703 (2013)
[9] CasP version 5.2, https://www.helmholtz-berlin.de/people/gregor-schiwietz/casp_en.html, (2014)
[10] D. Wittwer et al., Nucl. Instrum. Methods Phys. Res., Sect. B 268, 28-35 (2010)
[11] J. F. Ziegler, SRIM – The stopping and range of ions in matter (2013)

Electrochemical separation of Cu from Ni and Co

P. Dutheil (PSI&ETHZ), P. Steinegger (PSI&ETHZ), M. Heule (PSI)

Introduction

Chemical separations are essential for the preparation and purification of radionuclides for radionuclide-specific analysis. Such separations usually involve the use of, e.g. ion exchange chromatography, extraction chromatography, or (co-)precipitation. A thus far poorly explored, but still promising option is controlled-potential electrolysis. Indeed, a selective electro-deposition of radionuclides from solution may provide a good alternative and a complementary approach for standard radioanalytical separations. The electro-chemical separation of electroactive from non-electroactive radionuclides in aqueous solution was already investigated earlier [1]. Therefore, we explore here the separation of Cu from Ni and Co as an example and a model system to understand key parameters for the separation of different electroactive species by electrodeposition. In addition, this is of practical relevance for analyses of samples where radioactive copper (e.g. ^{64}Cu or ^{67}Cu) or high amounts of stable copper need to be removed from the analyzed matrix (e.g. containing ^{63}Ni) [2,3].

Experimental

All solutions were prepared with $Cu(NO_3)_2 \cdot 3\,H_2O$ (≥ 99.5%, Merck), $CuCl_2 \cdot 2\,H_2O$ (≥ 99%, Sigma-Aldrich), $Ni(NO_3)_2 \cdot 6\,H_2O$ (≥ 99%, Fluka), $NiCl_2 \cdot 6\,H_2O$ (≥ 98%, Sigma-Aldrich), $Co(NO_3)_2 \cdot 6\,H_2O$ (≥99%, Fluka), $CoCl_2 \cdot 6\,H_2O$ (≥ 99%, Fluka), HCl (suprapur, Sigma-Aldrich), HNO_3 (suprapur, Sigma-Aldrich) and ultrapure water (18.2 MΩ·cm, Merck Millipore).

All electrochemical experiments were carried out using a PGSTAT204 potentiostat (Metrohm Autolab). Cyclic voltammetry (CV) measurements were recorded at a glassy carbon (GC) disk working electrode (3 mm diameter) against a Ag/AgCl/3 M KCl reference electrode and with a Pt rod counter electrode. Voltammograms were obtained at room temperature in a quiescent aerated solution in a simple undivided cell. The GC electrode was polished with alumina powder (0.3 µm, Sigma-Aldrich) suspended in ultrapure water on a microcloth to yield a clean GC surface before each experiment. For bulk electrolysis experiments, only the working electrode was exchanged to a GC rod and a stirring bar was added to the electrochemical cell. Thus, all herein reported potential values are measured against the Ag/AgCl/3 M KCl reference electrode (0.209 V vs. standard hydrogen electrode). During bulk electrolysis, about 20 mL of solution was used. To track Cu, Co, and Ni concentrations by means of ICP-OES as a function of time, aliquots of 0.5 mL were taken at regular intervals. Measurements were performed using an Agilent 5110 ICP-OES (Agilent Technologies, U.S.A.) calibrated externally for Cu (at 213.60, 324.75, and 327.40 nm), Ni (at 216.56 and 227.02 nm), and Co (at 228.61 and 238.89 nm). Calibration standards with concentrations ranging between 0.313 g/L to 5 g/L were prepared by dilution of 1000 g/L certified calibration standards (TraceCERT, Sigma-Aldrich) in 2% HNO_3.

Results and discussion

Typical voltammograms of Cu in HNO_3 are displayed in figure 1. The first cathodic peak (I_c) and its associated anodic peak (I_a) can be attributed to reduction of Cu^{2+} to Cu on the electrode and to the reverse reaction. Meanwhile, the second cathodic peak (II_c) is due to the catalytic reduction of NO_3^- at the deposited Cu [4].

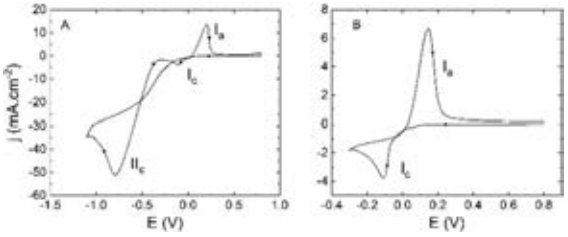

Figure 1: CVs of 10 mM Cu in 0.1 M HNO_3 at reverting potentials **A** -1.1 V, and **B** -0.3 V (at 0.05 V/s).

In HCl media, the shape of the voltammogram is changing (see figure 2) to two successive cathodic peaks I_c and II_c, which correspond to the two step reduction of Cu^{2+} to Cu^+ (I_c) and Cu^+ to Cu (II_c), with the concomitant direct reduction of Cu^{2+} to Cu also taking place at the current minima II_c [5]. This two-step mechanism is a result of the stability of the Cu(I) chlorido-complexes. The anodic peaks II_a and I_a correspond to the respective reverse reactions. Since the formation of the intermediate Cu(I) species is depending on the concentration of chloride, the position of the oxidation/reduction peaks in the voltammogram changes with different molarity of HCl (i.e. the reduction potential varies with HCl concentration).

The CVs of Co^{2+} and Ni^{2+} obtained in the same media and potential windows show no reduction peak. Therefore, the two metals will not co-deposit with Cu, if the potential applied to the electrode is in the studied potential range. The reduction potential for the selective electrodeposition of Cu can then be chosen accordingly.

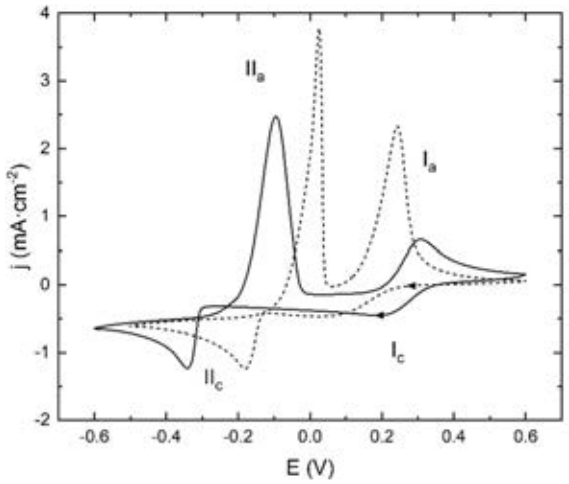

Figure 2: CVs of 10 mM Cu in 0.1 M HCl (dashed line) and 1 M HCl (solid line) at 0.01 V/s.

Controlled-potential electrolysis were carried out in mixtures of about 1 ppm Cu, Ni, and Co in 0.32 M HNO_3 and 0.1 M HCl (see figure 3 and 4). The concentrations of Cu, Ni, and Co in the electrochemical cell were monitored during electrolysis by the above-mentioned extraction of 0.5 mL aliquots at regular intervals.

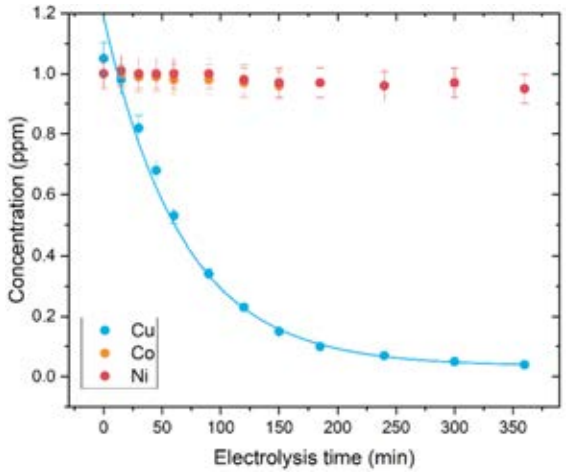

Figure 3: Concentrations changes of Cu, Ni, and Co in 2% HNO_3 during a bulk electrolysis at -0.4 V. The blue line corresponds to the best exponential fit for the copper concentration change.

The concentration of Cu is decreasing during the electrolysis, whereas concentrations of Co and Ni remain constant. In 0.32 M HNO_3, the concentration of Cu decreases by about 80% after 2 hours of electrolysis, similar results are obtained in 0.1 M HCl, where 75% of the Cu is reduced after 2 hours of electrolysis. The concentration of Cu decreases exponentially with time according to a rate constant, which corresponds to the expected behavior for controlled-potential electrolysis under diffusion-limited conditions [6].

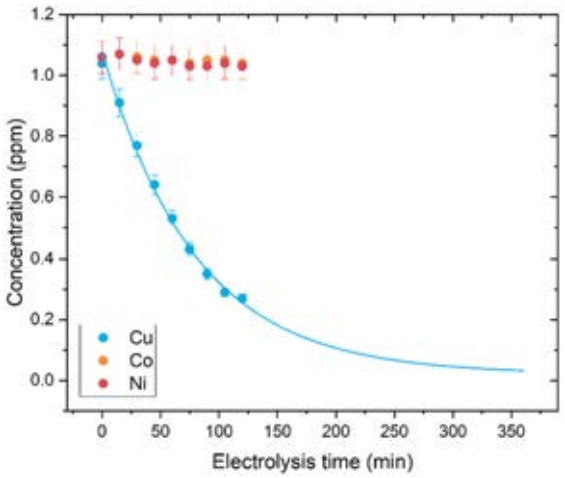

Figure 4: Concentrations changes of Cu, Ni, and Co in 0.1 M HCl during a bulk electrolysis at -0.5 V. The blue line corresponds to the best exponential fit for copper concentration change.

With the known rate constant, one can estimate the needed experimental time to reach the desired separation. In these experiments, the rate constant was in the order of $\approx 2 \cdot 10^{-4}$ s^{-1} for both reductions, which leads to rather slow electrolysis. However, in 0.32 M HNO_3 almost all Cu (96%) could be separated from the solution in 6 hours, which is already of practical relevance, and similar results are expected in 0.1 M HCl. Since the rate constant of the electrolysis is mostly fixed by the electrolytic cell configuration, the rate can be modified by changing the electrochemical cell setup. For instance, increasing the ratio of electrode surface area to volume of solution with, e.g. porous electrodes, and substantially increasing the convection in the cell should already allow reaching a timescale, which is more appealing for routine separation.

These results show that a simple voltammetric characterization of the HNO_3 and HCl systems, containing Cu, Ni, and Co, helped to implement and optimize a successful controlled-potential electrolysis procedure for the quantitative separation of Cu from Ni and Co in model solutions. The next step will focus on the application of a similar procedure for the separation of radionuclides in real samples.

References

[1] P. Dutheil et al., LRC Annual Report 2021, pp 12-13, (2022)

[2] D. Schumann et al., Radiochim. Acta, 97, pp 123-131, (2009)

[3] N. Van der Meulen et al., J. Label. Compd. Radiopharm., 62, pp 460-470, (2019)

[4] D. Pletcher et al., Electrochim. Acta, 24, pp 1253-1256, (1979)

[5] D. M. Soares et al., J. Electroanal. Chem., 532, pp 353-358, (2002)

[6] J. J. Lingane, Anal. Chim. Acta, 2, pp 584-601, (1948)

The role of lanthanoids in nuclear forensic applications

M. Hofstetter (PSI&ETHZ&SpiezLab), S. Röllin (SpiezLab), P. Steinegger (PSI&ETHZ)

Why to study lanthanoid patterns?

In geologic studies, the modification and fractionation of lanthanoid patterns are of interest in order to understand the geologic processes responsible for rock and mineral formation [4-7]. In geological terms, lanthanoids are lithophilic and thus, they are found in the earth mantle. They are classified as large-ion, lithophilic elements (LILE), which are incompatible with the main silicate and rock forming phases in the mantle and the earth crust [4-7]. This leads to the accumulation of lanthanoids in secondary phases and their fractionation from main magmatic phases. In rock, lanthanoids can be found selectively deposited in minerals, but associated partition coefficients are very selective for individual minerals [4]. Even if the electronic structure of lanthanoids (with the exception of redox-active cerium and europium) are very similar, the fractionation processes are subjected to a distribution coefficient, specific for each lanthanoid element [4,5]. It is important to note, that cerium and europium do not follow the general trend [5,7]. Europium is known to be reduced from Eu^{3+} to Eu^{2+} (thus, achieving a half-filled $4f$-shell) under conditions, such as found in hydrothermal waters [5,8]. On the other hand, the oxidation of cerium from Ce^{3+} to Ce^{4+} (thus, achieving an empty $4f$-shell) is observed under weathering conditions and high oxygen fugacities, as present on the surface of the crust and in ground water sediments [4,5]. The reduction of europium and the oxidation of cerium leads in both cases to a higher affinity towards the silicate phases and therefore to selective anomalies in the corresponding lanthanoid patterns [9].

Ore formation is often interconnected with secondary and even with late-stage remobilization and mineralization processes. These go hand in hand with further fractionation. Lanthanoids and premordial actinoids share common geochemical and orogenic properties. In fact, lanthanoids are often found together with uranium and thorium deposits, as both are incompatible with silicate phases. For the deposition of uranium and thorium, different mechanisms are responsible during secondary and late-stage ore formation [10,11]. These involve temperature [8,12], pressure [8], pH [10,12,13], redox potential [10,11], the presence of water [4,11] and the carbon dioxide availability [4] as well as stabilizing or precipitating ligands [4,12,13] and cations [14,15]. The advantage from a nuclear forensics perspective is that under these different orogenic conditions, the lanthanoids obey individual fractionation coefficients. This leads to uranium and thorium deposits with different lanthanoid patterns. Additionally, orogenesis occurs in several stages, where initially formed ore deposits are remobilized and again deposited under various conditions. Hence, this makes lanthanoid patterns an almost unique fingerprint for individual thorium or uranium ore deposits.

Development of a new method

The isolation of lanthanoid elements from uranium matrices may be carried out using an UTEVA resin (dipentyl pentylphosphonate). This resin has a specific affinity for tetravalent actinides, such as Th^{4+}, U^{4+} and Pu^{4+}. Usually the resin is filled and conditioned in a column before loading the tetravalent-actinide-containing solution. However, non-reproducible retention factors hindered an initial application of an UTEVA resin to the herein presented problem of quantifying ultra-trace amounts of lanthanoids in uranium matrices. These variations were likely a consequence of a varying column packing, even though prepacked columns are commercially available. To ensure a higher and more homogeneous saturation, the resin was directly suspended in the liquid sample (> 3 M nitric acid; see figure 1). After a short equilibration time of approximately 10 min on a shaker, the supernatant was carefully decanted after centrifugation into a new vial.

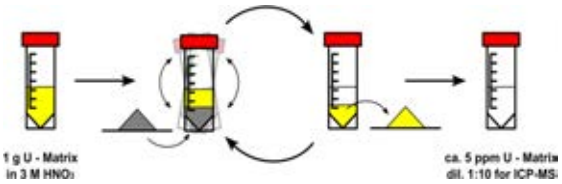

Figure 1: Uranium matrix removal by UTEVA resin.

This procedure enabled the removal of uranium from initially 1 g uranium matrix by a factor of ≈ 10^5 to ≈ 10^6, thus, resulting in a sample containing 1 - 5 ppm of the initial uranium matrix. This matrix concentration of ≈ 1 ppm is directly compatible with sector field, inductively coupled plasma mass spectrometry (sf-ICP-MS) measurements. The only drawback is found in the rather high acid concentration. To overcome this problem, a tenfold sample dilution was deemed to be an acceptable loss in sensitivity. Prior measurements at the Spiez Laboratory showed that some uranium materials can contain an extremely low lanthanoid contamination. Therefore, it was decided to subject the

new developed method to very pure uranium material and thus, to optimize it on challenging samples with lanthanoid impurities close to the detection limit.

Quantification using sf-ICP-MS

In general, with the analysis equipment available at the Spiez Laboratory, it is possible to quantify concentrations down to 1 – 0.1 ppt. Previous methods regarding the sample preparation for lanthanoid measurements were based on the dilution of the dissolved sample by a factor of up to 10^6 [13]. Hence, such a dilution leads to a loss in sensitivity and enables the quantification of trace impurities only until the ppm range. Compared with the newly developed method, involving an initial dissolution of 1 g uranium sample in 28 mL 3 M HNO_3 and a final dilution by a factor of 10, the total dilution amounted to only a factor of 280. This results in a roughly 10^3 times higher sensitivity as compared to the direct quantification. Thus, the herein presented development allows for a quantification down to ppb level. Even if a quantification is theoretically possible, various problems have been encountered during the still challenging quantification of lanthanoids in lower ppb to ppt levels. A major problem concerns memory effects of the ICP-MS upon changing sample matrices. It is hypothesized and currently investigated, that the change from the washing solution to a sample containing the analyte increases the background. Furthermore, resin-derived contamination with organic material and traces of hydrofluoric acid led to a chromatographic behavior and precipitation of the analyte in the sample introduction system. However, this problem has been overcome by avoiding hydrofluoric acid. Further, higher analyte stabilization was observed in the presence of citric acid.

Acknowledgements

We appreciate inputs from the International Technical Working Group in Nuclear Forensics, who draw our attention on UTEVA resin. Moreover, this work would not be possible without the Nuclear Division of the Spiez Laboratory. We thank the Nuclear Division in Spiez and look forward into a close collaboration between Spiez and PSI.

References

[1] M. Wilson. Igneous Petrogenesis, Springer (2007).
[2] M. R. Cicconi, et al. Magma Redox Geochemistry; AGU: (2021) pp 381 - 398.
[3] D. J. DePaolo. Neodymium Isotope Geochemistry: An Introduction, Springer (1971).
[4] C. Chauvel, Incompatible Elements, In Encyclopedia of Geochemistry Springer (2018), pp 719 - 721.
[5] R. M. Holder, et al. Geochemistry, Geophysics, Geosystems (2020), 21.
[6] H. G. Dill. Sedimentary Geology (1994), 92, 175 - 196.
[7] STI/PUB/374, IAEA (1974).
[8] TECDOC-1629 (UDEPO). IAEA (2009).
[9] M. Louvel, et al. Nat Commun (2022), 13, 1456.
[10] J. Gonzalez-Estrella, et al. Environmental Science and Technology (2020) 54, 3979 - 3987.
[11] A. K. Alwan, et al. Mineralogical Magazine (1980) 43, 665 - 667.
[12] T. J. O'Brien et al. Inorganic and Nuclear Chemistry Letters (1981) 17, 105 - 107.
[13] J. Krajkó, et al. Radiochimica Acta (2016) 104, 471 - 479.

Gas chromatographic assessment of iodine retention on zeolites: Characterization of the thermal stability of zeolites

L. Liu (PSI), K. Tokoi (UNIO), R. Eichler (PSI&UniBern)

Introduction

Isotopes of iodine are amongst the radiologically most significant radionuclides, which can be released from a severe accident in nuclear reactors. Silver-containing zeolites (Ag-Zeolites) are applied in some Filtered Containment Venting Systems (FCVS) to retain gas-phase iodine species, especially organic iodides, which are difficult to trap by other methods. Depending on the features of a specific Ag-zeolite, retention of iodine can be physical adsorption in the zeolite structure (mainly on silica surface) and/or a chemical reaction with the implemented Ag forming AgI. However, the performance of the Ag-zeolite has not been comprehensively characterized, for instance the retention efficiency at temperatures higher than 200 °C has not been verified. In the framework of the CAESIUM project (Combined Analytical and Experimental Studies of Iodine Uptake Materials), the iodine retention performance of zeolites at high temperatures will be experimentally investigated via gas chromatography methods. Here, we present the established experimental setup and the results of preparatory preliminary studies on the characterization of zeolites with radon.

Experimental

The Ag-zeolite and the pure zeolite are purchased from GemVax & KAEL and are used as received. A gas loop for the isothermal chromatography was built and a sketch is shown in figure 1. Briefly, the setup is composed of six major components. The TRACY (Trace gas Reaction Analyzer for ChromatographY, ①) gas loop is aimed at providing a clean controlled gas flow [1]. Various gases can be mixed to a desired ratio and then fed into the gas loop for the experiments. According to the need of experiments, the gas flow can either pass through a hot tantalum getter and a Sicapent® cartridge for reducing the oxygen content and the moisture, or pass through a humidifier to increase the water content. The gas flow is then connected to a ^{220}Rn source (②). ^{220}Rn gas is emanating from a ^{232}Th-organic compound, as one of its decay products. In fact, ^{232}Th ($t_{1/2}$ = 14·10^9 a) and ^{220}Rn ($t_{1/2}$ = 55.6 s) are in secular equilibrium. Therefore, ^{220}Rn will be continuously produced at a stable rate. A bypass is installed in case the ^{220}Rn source is not needed during loop gas equilibration and drying. The experiments are started then by switching the Rn source into the loop. Subsequently, the ^{220}Rn is flushed by the carrier gas through a zeolite unit (③) and is partly or fully retained on the zeolite depending on the applied temperature. The zeolite is filled into a quartz tube and immobilized by quartz wool plugs. The quartz tube is put into a steel cladding tube with Swagelok connections. Teflon tape is used to ensure the gas flow entirely through the zeolite inside the quartz tube. The whole component is inserted into an isothermal oven to heat the fixed-bed zeolite for a one-temperature-per-experiment between 25°C and 1100 °C. In order to adjust the pressure of the gas that flows through the source which will determine the volumetric flow rate, a needle valve (④) is connected to the loop. Depending on the adsorption efficiency of zeolites at different temperatures, ^{220}Rn could also pass through the zeolite-filled column. Therefore, an Ag-zeolite trap (⑤) and a charcoal trap (⑥) are placed downstream from the zeolite column to capture the residues. Efficient retention of radon by silver-enriched zeolite at room temperature was shown by Heinitz et al. [2]. The ^{220}Rn can be quantified by the activity of its decay product ^{212}Pb ($t_{1/2}$ = 10.6 h), which can easily be determined by γ-spectrometry using its characteristic γ-lines 238.6 and 300.1 keV, respectively. Since all measurements were performed in the same geometry, the count rates can be used directly for comparison.

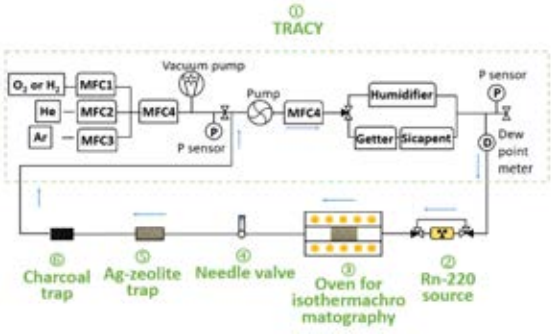

Figure 1: Sketch of the experimental setup

Results and discussions

Initially, several experiments have been performed, with only charcoal traps behind an empty column in ③ (without zeolite inside) in order to characterize the Rn source. Different amounts of activated charcoal were applied in the traps (see table 1). However, the activities measured in the traps varied. In addition, a significant amount of Rn was measured in the last trap. In fact, the used activated charcoal (Alfa Aesar) is not a

very efficient trapping agent for Rn. According to the literature, the typical radon adsorption coefficient (*k*) of activated charcoal is ~7 L/g [3]. The used amount of activated charcoal in the traps was obviously not enough for retaining all the Rn release from the source during experiment. Still, the more charcoal was used, the more activity was retained. However, due to the caused backpressure, there was a limit to the allowed charcoal amounts.

Table 1: Experimental conditions for the measured count rates of the activated charcoal trap

Amount of activated charcoal (volume × number)	**Pressure of the flow (bar)**	**Pb-212 (charcoal trap) * (a.u.)**
0.57 cm^3 ×2	0.13	293 ± 1.7
0.85 cm^3 ×2	0.13	379 ± 2.1
0.57 cm^3 ×3	0.44	332 ± 2.0
1.57 cm^3 ×2	0.15	440 ± 11

* Count rates in arbitrary units (a. u.) measured by putting charcoal traps one by one in the center of the γ-detector and assuming it is a point source.

Ag-zeolite could be an efficient trapping agent, with a *k* value up to 1820 L/g [2]. Therefore, a self-made Ag-zeolite trap (⑤ and figure 2) is added before the charcoal trap (⑥). A series of experiments were carried out to find out the needed amount of Ag-zeolite for full retention of Rn and to test the reproducibility. According to the results (table 2), 3 g of Ag-zeolite is sufficient to capture all the transported ^{220}Rn because less than 1% of ^{220}Rn is found in the charcoal trap.

Table 2: Experimental conditions for the measured count rates on the Ag-zeolite trap and on the activated charcoal trap

Mass (g)	Pressure of the flow (bar)	Pb-212 (Ag-zeolite trap)* (a.u.)	Pb-212 (charcoal trap) (a.u.)
1	0.12	321 ± 2.6	24.7
1.5	0.12	301 ± 3.1	10.6
3	0.12	369 ± 3.2	1.6
3	0.12	394 ± 4.0	1.9
3	0.11	360 ± 4.8	1.7

* Count rates in arbitrary units (a. u.)measured by putting the first centimeter (of the gas inlet side) of the Ag-zeolite in the center of the γ-detector and assuming it is a point source.

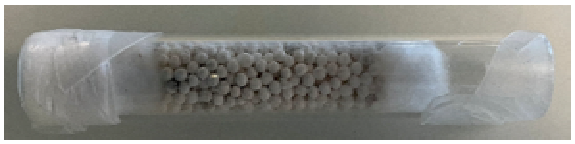

Figure 2: The Ag-zeolite trap containing 3 g of Ag-zeolite

The overall count rate delivered by the Rn source (②) and transported through an empty zeolite column to the trap is determined to 374 ± 18 a.u.. In addition, the repetitions of the experiment indicate that the overall uncertainty is about 5%, mainly from the packaging of the Ag-zeolite trap and the geometrical positioning of the trap on the γ-ray detector.

Using a Brunauer-Emmett-Teller (BET) method, the zeolite surface stability over the temperature range of the iodine investigation (between 25 °C and 800 °C) can be accessed via ^{220}Rn retention.
Experiments were firstly performed with the pure zeolite to deduce the retention of ^{220}Rn. Knowing the adsorption enthalpy of radon on silica of -20 kJ/mol, the surface-to-open-volume-ratio can be determined from gas adsorption chromatographic principles [4] (figure 3). The preliminary results indicate that the silica surface of the pure zeolite seems to equilibrate up to 500 °C.

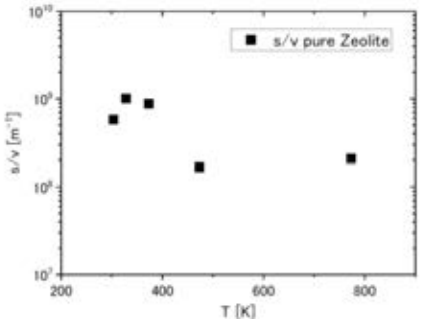

Figure 3: Determined surface-to-volume ratios for the pure zeolite

Preliminary experiments with ^{220}Rn retention on the Ag-zeolite at 200 °C and 500 °C were carried out. The results were used to evaluate the adsorption interaction of radon on metallic silver. An adsorption enthalpy of -25±2 kJ/mol was derived, which is in accordance with experimental results obtained in 2002 [5]. This entire series will be repeated with both zeolites, after they were preheated for several hours in vacuum, in He, He/O_2 and He/H_2O at 500 °C and 800 °C, in order to show the surface stability over the entire temperature range at the conditions of the envisaged iodine experiments.

Acknowledgements

This research is supported by swissnuclear through the CAESIUM project.

References

[1] P. Ionescu et al., LRC Annual Report 2021 (2022), pp. 14-15
[2] S. Heinitz et al. Room-temperature Rn-222 adsorption using silver exchanged zeolites. RADCHEM conference Mariánské Lázně 2022 (unpublished).
[3] Q. Zhou, G. Zhao, D. Xiao, S. Qiu, Q. Lei, K. J. Kearfott, Radiat. Meas. 119 (2018) 112–120.
[4] R. Eichler, B. Eichler in THe Chemistry of Superheavy Elements 2. Ed. (Eds.M.Schädel, D. Shaughnessy Springer Berlin Heidelberg 2014.
[5] R. Eichler, M. Schädel, J. Phys. Chem. B106 (2002) 5413-5420.

Adapt real temperature profiles for Monte-Carlo simulations of isothermal gas adsorption chromatography experiments

R. Dressler (PSI), R. Eichler (PSI&UniBern), P. Steinegger (PSI&ETHZ), J. Wilson (PSI&ETHZ)

Introduction

Isothermal gas adsorption chromatography is a well-established method for studying the adsorption interaction of super-heavy elements (SHEs) and their lighter homologs. These can be studied in their atomic or molecular state with surface materials serving as stationary phases [1]. One of the key components is the use of sufficiently extended isothermal temperature ranges to assess the chemical equilibrium of the reactions at the interface between the mobile and the stationary phase. From such experiments, external chromatograms (yield as a function of the isothermal set-point temperature) are obtained which can be used to derive the chemical property of interest, the enthalpy of adsorption. In order to do this, Monte-Carlo simulations (MCSs) are used to model the transport of the chemical species of interest [2]. Once more, the knowledge of the real isothermal temperature profile is important, as it determines the retention time of the species, and thus, the yield passing through the experimental setup. In general, it is not feasible to perform experiments with uniform isothermal temperature profiles (i.e. a constant and stable temperature along the entire chromatography column during the entire run time). Usually, a reaction zone with elevated temperatures is required to produce the desired chemical species. Due to technical limitations, the real temperature profile commonly deviates significantly from an ideal isothermal temperature profile. A major advantage of MCSs is that measured temperature profiles can be easily implemented, allowing for the reliable reproduction of experimental results.

Previously, experiments with on-line gas chromatography using Tl/TlOH were reported [3]. In these experiments, the applied temperature profiles (i.e. the steady-state temperature of the isothermal oven) were measured using a thermocouple with a resolution of 1 cm. The tip of the thermocouple can be positioned on the surface along the column axis with an accuracy of 2 to 3 mm. This leads to a scatter of the measured temperatures at a certain position for different isothermal set-point temperatures in the order of 15°C. Hence, crossing temperature profiles are obtained; in case of the experiments presented in [3], this was mostly observed in the region of the dip between the reduction oven and the isothermal part. For general physical reasons, such crossings are not reasonable, since a higher set-point temperature must always result in a higher temperature at every point on the entire temperature profile.

Method

To ensure that a physically consistent set of temperature profiles is generated, the measured temperature values for each individual distance x were sorted in ascending order. Using this, the enveloping profiles consisting of all minimum and maximum temperature readings, $T_{min}(x)$ and $T_{max}(x)$ respectively, were obtained.

In a first step, formula (1) was used to calculate evaluated temperature profiles $T(x, T_S)$ for each used set-point temperature T_S:

$$T(x,T_S) = T_{min}(x) + \zeta(\vartheta,\gamma)\cdot\left(T_{max}(x) - T_{min}(x)\right) \quad (1)$$

A smooth morphing function $\zeta(\vartheta,\gamma)$ (see below) interpolates different reduced set-point temperatures ϑ in the interval between T_B and T_E by applying a shape parameter γ:

$$\zeta(\vartheta,\gamma) = \begin{cases} 0 & if\ \vartheta \le -1 \\ \frac{1}{2}\cdot\left[1+\tanh\left(\frac{\gamma\cdot\vartheta}{1-\vartheta^2}\right)\right] & if\ -1 < \vartheta < 1 \\ 1 & if\ \vartheta \ge 1 \end{cases} \quad (2)$$

$$\vartheta(T_S) = 2\cdot\frac{T_S - T_B}{T_E - T_B} - 1 \quad (3)$$

Figure 1 shows the behavior of $\zeta(\vartheta,\gamma)$ for different shape parameters γ.

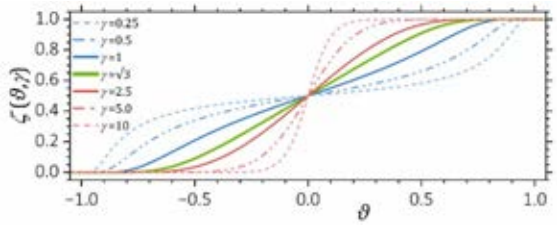

Figure 1: Morphing function $\zeta(\vartheta,\gamma)$ for different shape-parameters γ (γ=√3 is the straightest connection).

Thus, the obtained profiles $T(x, T_S)$ were used for nonlinear least squares fits of the experimental data with only three free parameters T_B, T_E and γ commonly used for all temperature profiles. Figure 2 shows the fitted profiles in comparison to the experimentally measured ones. Deficiencies of the fitting quality in the temperature range from 400 °C to 750 °C and for the maximum temperature of 950 °C are apparent.

To compensate for these deficiencies and to improve the fitting quality, the procedure was extended by introducing two additional intermediate temperature reference profiles T_{lo} and T_{med}, which were based on the average of the residual lower (3rd to 7th) and upper (8th to 12th) sorted temperature values, respectively.

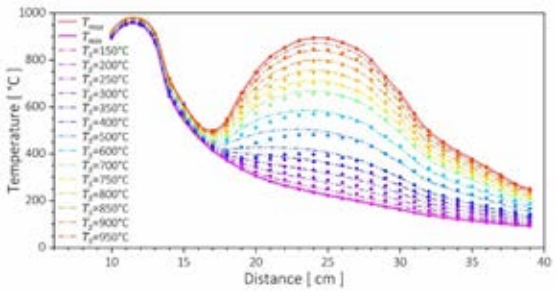

Figure 2: Evaluated temperature profiles for all used set-point temperatures T_S. The dots represent the experimental measurements and the dashed-dotted lines the fitted temperature profiles. In addition, the enveloping temperature profiles T_{min} and T_{max} are given as solid lines.

The formula for the temperature profiles now reads:

$$T(x) = T_{min}(x) + \begin{cases} \zeta(\vartheta_{lo}, \gamma) \cdot \left(T_{lo}(x) - T_{min}(x)\right) & + \\ \zeta(\vartheta_{med}, \gamma) \cdot \left(T_{med}(x) - T_{lo}(x)\right) & + \\ \zeta(\vartheta_{hi}, \gamma) \cdot \left(T_{max}(x) - T_{med}(x)\right) & \end{cases} \quad (4)$$

where the reduced temperatures ϑ_{lo}, ϑ_{med}, and ϑ_{hi} are calculated for three independent temperature regions (T_0; T_1), (T_2; T_3), and (T_4; T_5), respectively. This model fits the experimental data with in total seven free parameters - the shape parameter γ as well as the limits of all three temperature regions. The optimum fit parameters and their uncertainties are given in table 1.

Table 1: Optimum fit parameters.

Parameter	Value	Uncertainty
T_0	107°C	17°C
T_1	406 °C	17°C
T_2	297°C	15°C
T_3	822°C	15°C
T_4	696 °C	13°C
T_5	995°C	13°C
γ	1.39	0.19

Finally, Akima-Splines [4] were used to interpolate across the entire temperature profiles (see figure 3).

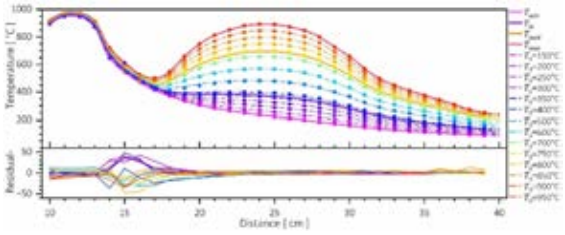

Figure 3: Temperature profiles of the Tl/TlOH experiments. In the upper panel: dots correspond to the measured temperatures whereas dashed-dotted lines indicate the evaluated temperature profiles. Also shown are the reference profiles: T_{min}, T_{lo}, T_{med}, and T_{max} (solid lines). The lower panel shows the residuals between the measured and evaluated temperature profiles (connecting lines to guide the eyes)

This guarantees a smooth connection between the sampling points, thus avoiding disturbing oscillations.

Conclusions

The presented method generates physically reasonable temperature profiles from imperfect experimental temperature measurements. This avoids artifacts in simulated external chromatograms caused by random scattering of measured temperature values. That is especially important in regions with narrow temperature distributions that are almost independent on the isothermal set-points, e.g. the dip region in the presented experiment. It also enables interpolation of measurement data not only along the chromatography column, but also across different temperature set-points which were not measured.

References

[1] M. Schädel, D. Shaughnessy (eds.), The Chemistry of Superheavy Elements, 2nd ed., Springer-Verlag: Berlin Heidelberg (2014)
[2] I. Zvara, The Inorganic Radiochemistry of Heavy Elements, Springer Science (2008)
[3] J. Wilson et al., Annual Rep. 2021 LRC, 10 (2022)
[4] H. Akima, J. Assoc. Comp. Mach. 17, 589 (1970)

Improving the quality of Ga radioisotopes to achieve high radiolabelling yields for radiopharmaceutical research

P.V. Grundler (PSI), C. Vaccarin (PSI/ETHZ), D. Beyer (PSI), C. Müller (PSI), N. P. van der Meulen (PSI)

Introduction

Two gallium radioisotopes are well established in medical imaging. The positron-emitting ^{68}Ga ($t_{1/2}$ = 68 min) is suited for Positron Emission Tomography (PET) imaging [1]. Its neighbour ^{67}Ga ($t_{1/2}$ = 78.3 h) has several γ-lines, making it suitable for Single Photon Emission Computed Tomography (SPECT) imaging and, in the case of preclinical studies, as a longer-lived surrogate for ^{68}Ga. Commonly, ^{68}Ga is obtained from generators loaded with ^{68}Ge ($t_{1/2}$ = 271 d) from which it can be eluted. Since the supply of generators is struggling to meet the demand, the development of ^{68}Ga production with medical cyclotrons is actively pursued, using liquid [2] or solid targets [3].

When produced directly by accelerators [4], both radioisotopes need to be separated from their respective target materials (natural or enriched Zn), which are present in massive excess ($1{\cdot}10^6$:1 for ^{68}Ga). To be able to achieve the labelling of peptides and other targeting vectors at high molar activity, trace metal impurities, which can compete with the gallium radionuclides for the chelating site, must be minimized. The requirements for ^{67}Ga as citrate for inflammation imaging are less stringent in this respect, since generous excess of citrate is not problematic [5] and can compensate for the presence of larger amounts of trace metal impurities. Thus, the quality of the commercially available ^{67}Ga, although sufficient for successful inflammation imaging, is often insufficient to allow high radiolabelling yields of peptides and other targeting vectors.

Besides the zinc target material, further metals (environmental contamination or irradiation side products) need to be removed. One of the most critical impurities is iron, since its ionic radius, in the trivalent state, is very similar to the one of trivalent gallium [6], thus, making its separation challenging.

The aim of this work was to develop a rapid purification method to provide pure gallium radionuclides to ensure labelling of vectors at high molar activity. This applies equally to commercially sourced ^{67}Ga or ^{68}Ga produced onsite with a cyclotron.

Experimental

The ^{67}Ga used in the present investigations was sourced commercially as a solution in HCl (Curium, Petten, NL). For the purification, a macroporous absorbent resin (Amberchrom CG161M, Dupont US) was used. For the final concentration and dispensing at a defined pH an extraction resin (TK 200, Triskem F) was used.

To an aliquot of the ^{67}Ga solution, $TiCl_3$ was added as reductant [7] and the solution strongly acidified with HCl. When passing this solution through a CG161M resin column, the ^{67}Ga was retained, whereas the impurities were eluted with 7.0 M HCl. The ^{67}Ga was then eluted using less concentrated HCl. This eluate was then loaded on the TK 200 column. The activity was eluted from this column with a minimal volume of 0.1 M HCl. The pH-adjusted purified ^{67}Ga solution was then used to radiolabel various compounds, including DOTATOC. For quality control, HPLC was used to assess the achievable radiolabelling yield of DOTATOC as a standard vector compound (figure 1).

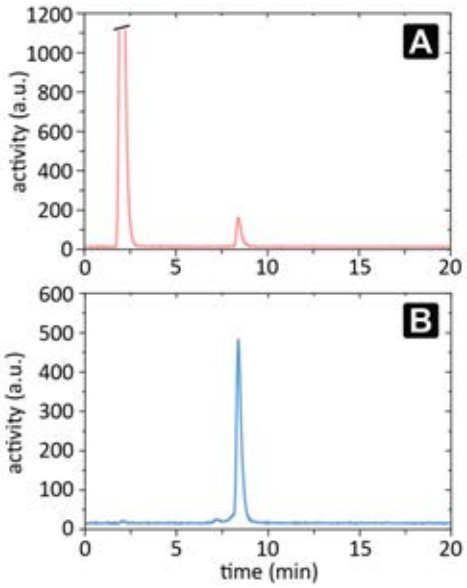

Figure 1: Chromatograms of DOTATOC labeled with ^{67}Ga, batch 2 of table 1. Retention time free activity: 2.2 min, retention time labeled DOTATOC: 8.2 min. **A** before purification, labelling yield 14% at 25 MBq/nmol. **B** after purification, labelling yield >99% at 100 MBq/nmol.

Results

Figure 1 strikingly illustrates the improvement in labelling yield achieved by the purification procedure.

Table 1 below shows the radiolabeling yield of ^{67}Ga before and after purification as determined by HPLC. Before the purification procedure even with a 30 to 75 fold excess of chelator (50 MBq of ^{67}Ga correspond to ≈34 pmol vs 1 nmol DOTATOC) the labelling yield was very poor. Whereas afterwards, with only a 15 fold excess of DOTATOC the labelling was close to quantitative.

Table 1: Radiolabelling yields achieved with ^{67}Ga before and after the purification procedure (n/d not determined).

Batch #	1	2	3	4
As received				
Molar activity ^{67}Ga MBq/nmol DOTATOC	25	25	50	20
Radiolabelling yield %	14	2	22	28
After purification				
Amount recovered /processed	250 /450	620 /1010	1223 /1495	1720 /1921
Molar activity ^{67}Ga MBq/nmol DOTATOC	25	100	100	100
Radiolabelling yield %	99	94	99	100
3 days after purification				
Molar activity ^{67}Ga MBq/nmol DOTATOC	n/d	50	n/d	n/d
Radiolabelling yield %	n/d	99	n/d	n/d

Thanks to its rapidity, the same purification procedure was applied to the recovery of ^{68}Ga from ^{68}Zn targets irradiated with the Injector 2 cyclotron at PSI, with encouraging results as to separation yield and radiochemical purity.

Conclusions & outlook

A significant improvement of the radiolabelling yield for peptides and other targeting vectors has been achieved enabling the preparation of $^{68/67}$Ga-based radioligands at high molar activity. This is an essential requirement for imaging of targets expressed at moderate levels as high amounts of unlabelled targeting vectors would compromise the visualization of the structures of interest.

The suitability of this method for direct recovery of ^{68}Ga from irradiated ^{68}Zn targets has been demonstrated and further work will focus on the streamlining of the procedure to allow reliable routine production.

Acknowledgements

We thank Alex Sommerhalder for his support with the irradiations and handling of the targets at PSI's IP2.

References

[5] I. Velikyan, Theranostics 4 (2014) 47.
[6] M.E. Rodnick et al, EJNMMI Radiopharm. Chem. 5 (2020) 25.
[7] S. Braccini et al, Appl. Radiat. Isot. 186 (2022) 110252.
[8] F. Szelecsényi et al, Nucl. Instrum. Methods Phys. Res. Sect. B 234 (2005) 375.
[9] P. Hoffer, Journal of Nuclear Medicine 21 (1980) 282.
[10] R. Shannon, Acta Crystallograph. Sect. A 32 (1976) 751.
[11] N.P. van der Meulen & T.N. van der Walt, Z. Naturforsch. B 62 (2007) 483.

The automated purification of ^{161}Tb and subsequent production of [^{161}Tb]Tb-DOTA-LM3 for clinical use

C. Favaretto (PSI&ETHZ), P.V. Grundler (PSI), Z. Talip (PSI), J.R. Zeevaart (Necsa), S. Landolt (PSI), D.E. Schmid (PSI), S. Geistlich (PSI), C. Müller (PSI), R. Schibli (PSI&ETHZ), N. P. van der Meulen (PSI)

Introduction

^{161}Tb ($t_{1/2}$= 6.95 d, $E\beta^-_{av}$= 154 keV (100%)) [1,2]) shows similar decay characteristics and chemical behavior to ^{177}Lu, which is currently regarded as the "gold standard" of targeted radionuclide therapy. However, ^{161}Tb has proven to be therapeutically superior than ^{177}Lu on a preclinical level because of its co-emission of conversion and Auger electrons (AE) [3]. Specifically, [^{161}Tb]Tb-DOTA-LM3 is a promising new therapy for neuroendocrine neoplasms based on an AE emitter combined with a somatostatin receptor antagonist [4], which was proposed for a clinical study. In this work, the introduction of ^{161}Tb into clinical practice was addressed; in particular, in order to be used in the clinical trial, both the production of the radionuclide and the ^{161}Tb-radiopharmaceutical must adhere to a specific quality standard, defined by the Good Manufacturing Practice (GMP) guidelines. Efforts were put into the development of a protocol towards an automated purification of ^{161}Tb and a GMP-compliant production of [^{161}Tb]Tb-DOTA-LM3.

Experimental

^{161}Tb production was carried out via the ^{160}Gd(n,γ)^{161}Gd→^{161}Tb nuclear reaction and separated from the target material with a previously-established method [5]. ^{161}Tb was further purified under GMP conditions using an Eckert & Ziegler automated-cassette-module system (figure 1) and a customized cassette (figure 2). The quality of the labeling solution obtained was evaluated in terms of identity, radionuclidic purity (RNP) and apparent molar activity (AMA), in order to validate the suitability for its clinical use. Moreover, using this labeling solution and the same automated module, the production of the final medicinal product [^{161}Tb]Tb-DOTA-LM3, compliant with GMP principles, was developed and validated. Analytical procedures for the quality control (QC) with the use of high-performance liquid chromatography and gas chromatography techniques were developed and used to demonstrate the suitable quality of the final product. Additional efforts, including validations of production process and analytical methods, as well as sterility evaluation and process controls, were required to establish a fully GMP-compliant process.

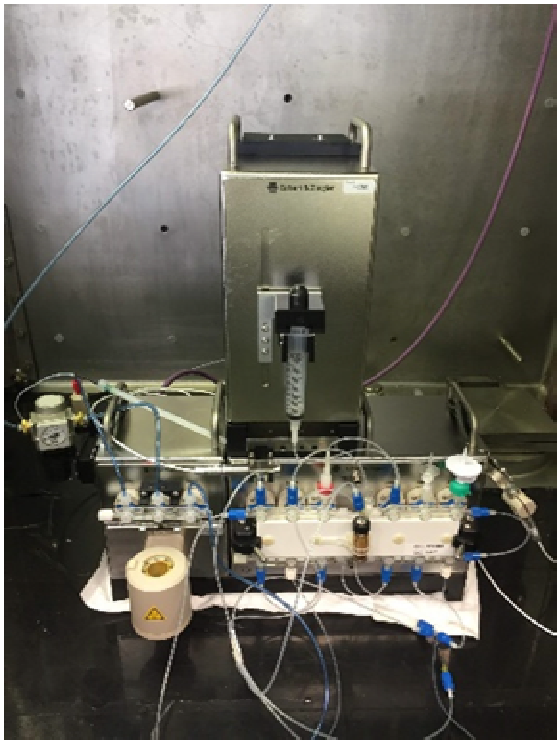

Figure 1. Eckert & Ziegler Modular- Lab Pharm Tracer fully automated cassettes synthesis system.

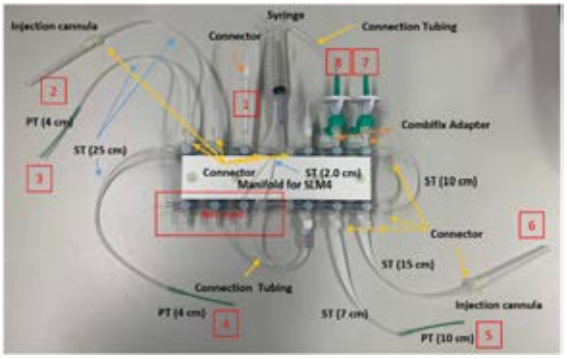

Figure 2. Specially-designed cassette for ^{161}Tb automated purification process. ST (x cm): silicon tubing (length); PT (x cm): peak tubing (length); 1: column with LN3 resin; 2: waste (1) vial; 3: final ^{161}Tb radioactive precursor vial; 4: waste (2) vial; 5: ^{161}Tb RLS vial; 6: water ultrapure vial; 7: HCl 0.01 M vial; 8: HCl 0.05 M vial.

Results and discussion

The ^{161}Tb automated purification process resulted in up to 7.4 GBq of ^{161}Tb in 1.2 mL, with RNP ≥ 99.9% and AMA at 100 MBq/nmol with radiochemical purity (RCP) ≥ 95.0%. The purification method was validated for the range of activity that would be used in the initial part of the clinical trial (0.5 to 1 GBq/dose). With the purified ^{161}Tb obtained, an automated production of [^{161}Tb]Tb-DOTA-LM3 was performed for the first time with activities up to 4.5 GBq in 20 mL and also validated for the same range of activity, demonstrating the product's suitability for the initial phase of its clinical use. The chromatographic methods developed for the QC were shown to be suitable for their intended use and the synthesis batches demonstrated good quality of the product, with RCP ≥ 95% up to 24 hours, negligible level of impurities and acceptable level of ethanol (≤ 7%). Further sterility and process controls, including a matrix-based bubble point test, a Limulus Amebocyte Lysate (LAL) test and a bioburden test, proved the aseptic manufacturing procedure.

References

[1] N. Nica, Nuclear Data Sheets, 160, (2019).
[2] T. Duran et al., Appl Radiat Isot, 159, (2020).
[3] C. Muller et al., EJNMMI, 41, (2014).
[4] F. Borgna et al., EJNMMI, 49:4, (2021).
[5] N. Gracheva et al., EJNMMI Radiopharmacy and Chemistry, 4:12, (2019).

Production cross sections of thulium radioisotopes with an 18 MeV medical cyclotron for the production of thulium-167

E. Renaldin (PSI&UniBern), G. Dellepiane (AEC-LHEP&UniBern), S. Braccini (AEC-LHEP&UniBern) N. P. v.d. Meulen (PSI), R. Eichler (PSI&UniBern), Z. Talip (PSI)

Introduction

Nuclear medicine is focusing on novel and efficient techniques for treating cancer by means of imaging and therapy. In particular, targeted radionuclide therapy (TRT) shows appealing characteristics in targeting tumor cells, while sparing healthy tissues [1]. This goal is achieved using pharmaceuticals labeled with β- or α-particles or Auger-electron emitting radionuclides. The latter are suitable to tackle small or single-cell tumors due to their short range and high Linear Energy Transfer (LET) [2]. In this context, ^{167}Tm is an Auger-electron emitter with a 9.25-day half-life that emits an intense 208 keV (I_{abs} = 42 %) γ-ray, which can also be used for Single-Photon Emission Computed Tomography (SPECT). However, the biological effects of Auger electrons should be thoroughly investigated to assess their potential for medical applications.

In a previous report [3], the authors presented the ^{167}Tm cross section measurements using enriched ^{167}Er and ^{168}Er oxides. In this study, we particularly focused on the improvement of the experimental ^{165}Tm and ^{168}Tm cross sections data.

Materials and methods

The targets consisted of erbium oxide powder deposited on a 4 mm diameter pocket of an aluminum coin for cross-section measurements and 6-mm diameter 300 μm thick discs for production tests (details can be found in [3]). Irradiations were performed at the Bern medical cyclotron laboratory [4] providing 18 MeV proton beams. This facility is equipped with a solid target station (STS) for research on non-conventional medical radionuclides and with a beam transfer line (BTL) ending in a separate bunker, where cross-section measurements are performed by means of a specific target station [5].

The excitation function of the ^{167}Er(p,x)^{165}Tm reaction was, again, explored to determine the potential problem of large ^{166}Tm co-production. This short-lived radionuclide has a γ–emission at 194.7 keV (I_{abs}=0.83 %), which produces a coincidence sum peak at 242.9 keV with an X-ray of thulium: 48.2 keV (K-L_2, I_{abs}=28 %). As a result, the cross-section measurement of ^{165}Tm was distorted due to the overlapping between its main γ- line of 242.9 keV (I_{abs}=36 %) and the coincidence peak. Therefore, the γ–ray spectrometry measurements were performed, starting at least 2 days after the end of bombardment (EoB) to achieve complete decay of ^{166}Tm. The same process was also applied for the following test measurements, which were repeated for the thick targets.

The authors also focused on the improvement of ^{165}Tm and ^{168}Tm production cross-section measurements from enriched ^{168}Er oxide. In this case, four measurement points were repeated and another measurement point added for 12.6 MeV proton energy to assess the cross-section trend at the coulomb barrier.
In both cases, additional γ–ray spectrometry analyses were performed to improve the counting statistics for the ^{168}Tm activity measurements, thus, reducing the error.

Results

The figures 1, 2 and 3 show the comparison of the experimental results with theoretical calculations retrieved from TENDL 2019 [6].

The additional experiments resulted in a better agreement between experiment and theory (figure 1 and 2).

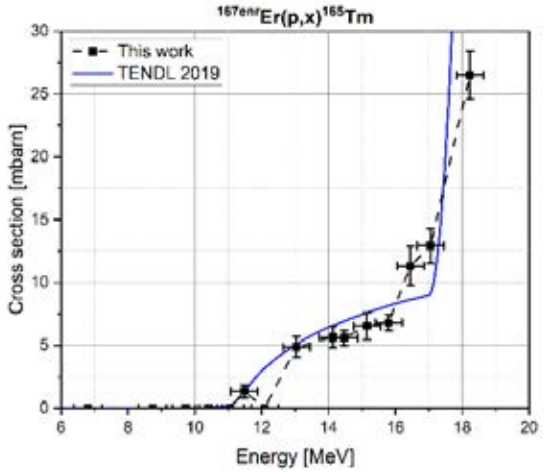

Figure 1: Comparison of experimental and theoretical production cross section of the ^{167}Er(p,x)^{165}Tm reaction.

In particular, the repetitions of ^{165}Tm cross-section measurements from $^{167}Er_2O_3$ confirmed our hypothesis. The experimental results clearly describe the contribution of both nuclear reactions: ^{166}Er(p,2n) and ^{167}Er(p,3n).

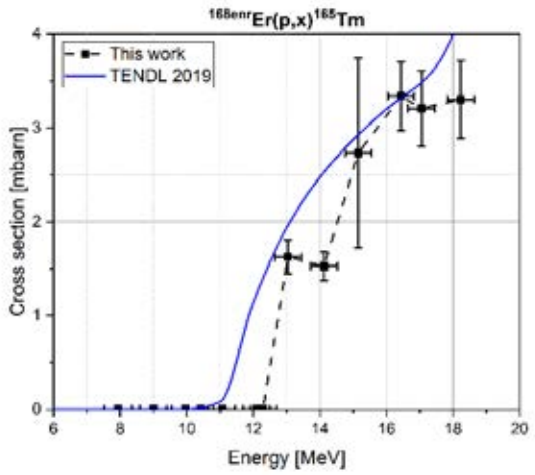

Figure 2: Comparison of experimental and theoretical production cross section of the ^{168}Er(p,x)^{165}Tm reaction.

Figure 3 illustrates the ^{168}Tm production cross section, whose main contribution is due to the ^{168}Er(p,n) nuclear reaction. TENDL 2019 data slightly underestimates the experimental cross sections between 11 – 13 MeV.

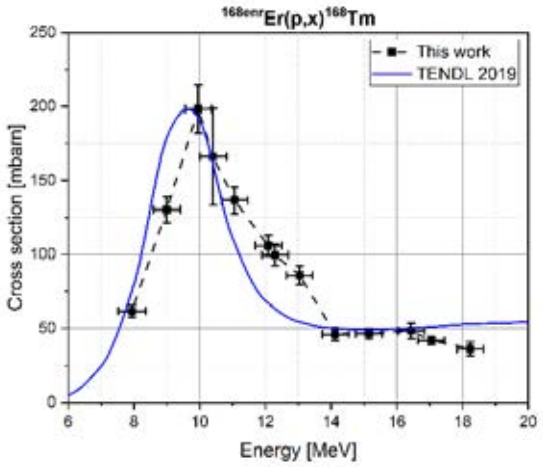

Figure 3: Comparison of experimental and theoretical production cross section of the ^{168}Er(p,x)^{168}Tm reaction.

Table 1: Experimental and theoretical ^{167}Tm production yield results for the proton-irradiated $^{167}Er_2O_3$ targets in the beam transfer line (BTL).

Inlet proton energy [MeV]			12.6
Production yield [MBq/μAh]	Target 1	Exp.	2.3 ± 0.5
		Th.	*(2.7 ± 0.3)*
	Target 2	Exp.	2.6 ± 0.5
		Th.	*(2.9 ± 0.4)*

The calculated nuclear cross-section results were, then, tested by comparing the theoretical and experimental integral production yields. Experimental production yield tests were performed for two targets using the beam transfer line (BTL) [7]. Table 1 shows the comparison between the experimental and theoretical results.

Conclusions and outlook

The experimental results were compared with theoretical predictions obtained with TENDL 2019, showing good agreement for the ^{167}Tm production.
The experimental results obtained were also used to calculate the nuclear cross sections contributing to the thulium radioisotopes production. Moreover, we tested the numerical cross-section data comparing experimental and theoretical production yields from proton-irradiated enriched ^{167}Er and ^{168}Er oxides. The production of ^{167}Tm using enriched ^{168}Er results in higher production yields and improved radionuclidic purity, declaring it the best candidate for ^{167}Tm production with low-energy proton beams. Additional irradiations with thick targets have been planned using a solid target station (STS) installed in the cyclotron bunker at Bern University Hospital. In this case, μA-proton currents and an efficient cooling system will be employed to test the production yields with longer irradiation time periods.

Acknowledgements

This research was partially supported by the Swiss National Science Foundation (SNF Grants Number: CRSII5 180352 and 200021_188495), and the European Union's Horizon 2020 research and innovation programme under grant agreement No. 101008571 (PRISMAP - The European medical radionuclides programme).

References

[1] C. Mothersill and C. B. Seymour *J. Nucl. Med.*, vol. 47, no. 6, pp. 899–900, 2006
[2] A. Ku et al., *EJNMMI Radiopharm. Chem.*, vol. 4, no. 1, 2019, doi: 10.1186/s41181-019-0075-2
[3] E. Renaldin *et al.*, *Annu. Rep. 2021 Lab. Radiochem.*, pp. 44–45, 2021
[4] S. Braccini *AIP Conf. Proc.*, vol. 1525, no. April 2013, pp. 144–150, 2013, doi: 10.1063/1.4802308
[5] T. S. Carzaniga *et al.*, *Appl. Radiat. Isot.*, vol. 129, no. July, pp. 96–102, 2017, doi: 10.1016/j.apradiso.2017.08.013.
[6] A. J. Koning et al. *Nucl. Data Sheets*, vol. 155, pp. 1–55, 2019, doi: 10.1016/j.nds.2019.01.002
[7] G. Dellepiane, "Cross section measurements of thulium radioisotopes with an 18 MeV medical PET cyclotron for an optimised Er-165 production," 2023 in preparation

Radionuclide Development: Behind the scenes in 2022

N. P. van der Meulen (PSI), Z. Talip (PSI), P.V. Grundler (PSI), C. Favaretto (PSI), C. C. Hillhouse (PSI), E. Renaldin (PSI/UniBern)

PRISMAP

The Radionuclide Development group has had a busy 2022, with regard to preparation and contribution towards large projects. The team has been working feverishly as part of the EU H2020 PRISMAP - The European medical isotope programme [1], as a partner in three work packages and the leader of one. The IP2 irradiation station and SINQ neutron source at PSI is being utilized towards the provision of non-commercial radionuclides deemed interesting for nuclear medicine applications. These nuclides are produced and sent to laboratories that intend to utilize them for preclinical, and potentially clinical, application. Currently, the Radionuclide Development group has been requested to produce ^{161}Tb, ^{155}Tb and $^{44/43}$Sc towards the success of this particular work package. Group members have also been extremely active in the work package aiming to harmonize and characterize radionuclides towards clinical application. A position paper with regard to standards towards clinical translation was prepared [2]. Over this period, Dr. Zeynep Talip has also been leading the radiolanthanide development work package.

^{161}Tb clinical translation

^{161}Tb is a radionuclide, developed by this group, which appears to be taking the nuclear medicine world by storm. Following the success of our research (in collaboration with the Nuclide Chemistry group of Center for Radiopharmaceutical Sciences - CRS), the industrial sector has shown great interest in commercializing the nuclide. In the meantime, the Radionuclide Development group as part of CRS is involved in a phase 0/1 clinical study with the University Hospital Basel, as part of a SNF project headed by Prof Damian Wild. To this end, our group has been active in developing a protocol towards the radio-pharmaceutical manufacture of ^{161}Tb-DOTALM3, the radiopharmaceutical to be applied to patients in this project. This has involved the characterization of product as well as the validation of production processes. Once this laborious process was completed, the data was compiled into a dossier, which was submitted to Swissmedic and BAG for evaluation in mid-October 2022. BAG and Swissmedic have both, subsequently, approved the application, making this the first radiometal successfully developed in Switzerland towards clinical translation.

IMPACT and TATTOOS

As mentioned in the Editorial from our Laboratory Head at the beginning of this report, LRC (including Radionuclide Development) is heavily involved in IMPACT (Isotope and Muon Production using Advanced Cyclotron and Target technologies) - a new Swiss Research Infrastructure proposal submitted by PSI, in collaboration with University of Zurich (USZ) and University Hospital Zurich (USZ). This will ensure the production and full exploitation of unprecedented intensities and quantities of muons and radionuclides at the High Intensity Proton Accelerator (HIPA) facility towards advancements in particle physics, chemistry, materials science, life sciences, medicine, as well as clinical research. It entails the construction of two new target stations and beamlines at HIPA, thereby, extending the existing infrastructure. The first aims to increase muon intensities by up to 100-fold for experiments in particle physics and materials science (High Intensity Muon Beams - HIMB), while the second (Targeted Alpha Tumour Therapy and Other Oncological Solutions - TATTOOS) aims to provide a wide range of previously elusive radionuclides suitable for advanced cancer treatments towards potential clinical studies. TATTOOS will take advantage of the 590 MeV, high intensity proton beam at HIPA to induce spallation reactions on heavy-element targets. When coupled to online mass separation, TATTOOS will provide a variety of medically relevant and other interesting radionuclides at an unprecedented quantity. The Conceptual Design Report for this mammoth endeavour can be found at [3].

References

[1] PRISMAP, https://www.prismap.eu/
[2] Decristoforo et al., Standards for clinical translation. https://doi.org/10.5281/zenodo.6599180
[3] IMPACT Conceptual Design report, https://www.psi.ch/en/media/71845/download

Nuclei as open quantum systems: A near-threshold proton-emitting resonance in ^{11}B

Y. Ayyad (IGFAE&USC), W. Mittg (MFRIB), T. Tang (FRIB), B. Olaizola (CERN), G. Potel (LLNL), N. Rijal (FRIB), N. Watwood (FRIB), H. Alvarez-Pol (IGFA&USC), D. Bazin (MSU&FRIB), M. Caamaño (IGFAE&USC), J. Chen (ANL), M. Cortesi (MSU&FRIB), B. Fernandez-Dominguez (IGFAE&USC), S. Giraud (MSU&FRIB), P. Gueye (MSU&FRIB), S. Heinitz (PSI), R. Jain (MSU&FRIB), B.P. Kay (ANL), E.A. Maugeri (PSI), B. Monteagudo (MSU&FRIB), F. Ndayisabye (MSU&FRIB), S.N. Paneru (MSU&FRIB), J. Pereira (MSU&FRIB), E. Rubino (MSU&FRIB), C. Santamaria (MSU&FRIB), D. Schumann (PSI), J. Surbrook (MSU&FRIB), L. Wagner (MSU&FRIB), J.C. Zamora (MSU&FRIB), V. Zelevinsky (MSU&FRIB)

Introduction

Nuclei can be described as open quantum systems: a weakly bound ensemble of nucleons coupled to an external environment. The open quantum system nature of nuclei emerge when we move towards the drip lines or when the nucleus is highly excited. Under such conditions, the properties of near-threshold states of the nucleus are defined by the intricate interplay between its bound part and the continuum. This coupling may manifest through very specific resonances via the appropriate reaction channel. As the system becomes gradually less bound, many-nucleon correlations may manifest through the formation of particle clusters via narrow resonances in the vicinity of the particle emission threshold, such as the famous Hoyle state in ^{12}C [1]. Therefore, reactions with radioactive (and also stable) isotope beams populating narrow resonances are the doorway to unify reaction and structure models.

One of the most recent cases of exotics near-threshold resonances was observed in the β-decay of the neutron-rich halo nucleus ^{11}Be into ^{10}Be+p. Its low neutron separation energy, Sn<782 keV, allows for the emission of a proton after β-decay, although, with a very low probability. Because of the small Q value of the reaction, protons are emitted with very low energy (200 keV), making its detection a real challenge. This counterintuitive process was observed at TRIUMF by implanting ^{11}Be ions in the prototype Active Target Time Projection Chamber [2], a gaseous detector with very low detection threshold. The branching ratio of this process was found to be much larger than theoretical predictions (10^{-6}) but consistent with previous indirect measurements [3]. The plausible explanation lies in the shape of the proton energy distribution: the decay proceeds via a narrow-resonance in ^{11}B at 11.45 MeV of about 15 keV of total width and slightly above the proton separation energy (11.23 MeV). Soon after the branching ratio was determined, many theoretical works tried to reproduce the result [4-6] without reaching a consensus with the experiment. Although there is a widespread agreement on the existence of the resonance, the properties of the resonance, and in particular, the value of the branching ratio, are still under a hot debate. To clarify the situation, more experimental effort is required. If such resonance exists, it should be populated with the inverse reaction: ^{10}Be+p resonant scattering. We performed such experiment in inverse kinematics using a reaccelerated beam at the Facility For Rare Isotope Beams (FRIB) of the Michigan State University (MSU) [7].

Experiment

To form the resonance in the ^{10}Be+p system in inverse kinematics, a pure beryllium beam with 350A keV of energy was reaccelerated and sent to a thick CH_2 target (9.6 μm). The beam source was prepared from material produced at the Paul Scherrer Institut (PSI) from proton-irradiated carbon [8]. The target also acted as a secondary electron emitter using an aluminium layer of few nm. The electrons produced by the interaction of the beam with the target were deflected to a Microchannel Plate that provided a start signal for particle identification. The beam was gradually stopped inside the target to cover the region of interest of the resonance. Only elastic scattered protons escaped from the target in forward direction. A 1 mm thick and 35 mm effective diameter single-sided silicon detector (Micron MSD035) was placed around 10 cm downstream of the target to measure forward scattered protons and α-particles from the ^{7}Li+α decay, the predominant decay mode of ^{11}B. Particles were identified via the Time-of-Flight and Energy correlation. The silicon detector was calibrated using a proton beam of different energies (down to 250 keV in the laboratory frame) and α particles from a ^{228}Th source. The reaction energy was corrected by the energy loss of the particles in the target.

Results and discussion

Figure 1 shows the excitation function for the ^{10}Be(p,p) reaction channel together with the R-Matrix calculation performed with AZURE2 [9]. The effect of the resonance can be seen clearly as an interference pattern on the ^{10}Be+p Coulomb scattering. The inferred width, energy and the spin-parity for this resonance of 16±3 keV, 171±20 keV, 1/2+ respectively, are in very

good agreement with the resonance observed in Ref. [2], thus confirming its nature.

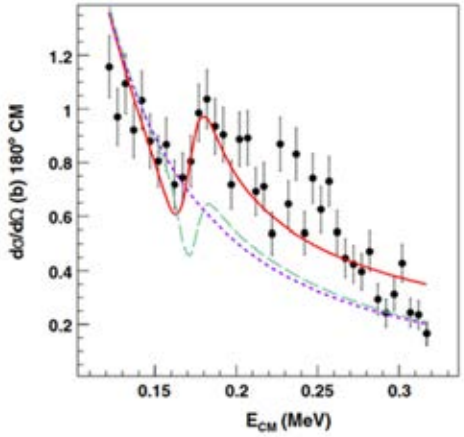

Figure 1: Excitation function for the ^{10}Be(p,p) reaction at 350A keV (dots). The solid and dashed lines represents the R-Matrix fit for J=1/2+ and J=1/2-. The dotted line refers to the Coulomb scattering cross section.

However, there are some important differences. The partial width for the proton decay branch amounts to 4.5±1.5 keV of the total width, as inferred from the R-Matrix fit. This indicates a missing branching ratio to α branch that could not be determined in this experiment because of the low intensity of the beam. In addition, the energy of the resonance is about 20 keV lower than the previous result. Both, the energy and width of the resonance are critical and very sensitive parameters for the calculations to reproduce the β-delay proton emission branching ratio. A direct measurement of the ^{10}Be(p,α) with a complete determination of the branching to different excited states in ^{7}Li is required to clarify the situation.

In conclusion, we have observed a near-threshold proton-emitting resonance in ^{11}B via the ^{10}Be(p,p) reaction at 350A keV. An R-matrix calculation was used to deduce the energy, spin parity, and resonance width, in good agreement with the values inferred in β-delayed proton emission of ^{11}Be. This is a strong indication that the exotic decay proceeds via this intermediary state, explaining the relatively large branching ratio observed. The results also suggest that the resonance has a sizable decay width to the α+^{7}Li channel.

Acknowledgements

This work is based on the research supported in part by the Spanish Ministerio de Ciencia, Innovación y Universidades. This work has received financial support from Xunta de Galicia (Centro singular de investigación de Galicia accreditation 2019-2022), by European Union ERDF, and by the "María de Maeztu" Units of Excellence program MDM-2016-0692 and the Spanish Research State Agency. Y. A. acknowledges the support by the Spanish Ministerio de Economía y Competitividad through the Programmes "Ramón y Cajal" with the Grant No. RYC2019-028438-I. This material is based upon work supported by the Department of Energy National Nuclear Security Administration through the Nuclear Science and Security Consortium under Awards No. DE-NA0003180 and/or DE-NA0000979, by the National Science Foundation, USA under Grants No. PHY-2012040, PHY-1565546, and PHY-1913554, and by the U.S. Department of Energy, Office of Science, Office of Nuclear Physics under grant no. DE-SC0020451 and Contract No. DE-AC02-06CH11357. This work was performed under the auspices of the U.S. Department of Energy by Lawrence Livermore National Laboratory under Contract No. DE-AC52-07NA27344.

References

[1] F. Hoyle, Astrophys. J. Suppl. Ser. 1, 121 (1954).
[2] Y. Ayyad et al., Phys. Rev. Lett. 123, 082501 (2019).
[3] K. Riisager et al., Physics Letters B, 732, 305-308 (2014).
[4] J. Okołowicz, M. Płoszajczak, and W. Nazarewicz.Phys. Rev. Lett. 124, 042502 (2020).
[5] M. C. Atkinson, P. Navrátil, G. Hupin, K. Kravvaris, and S. Quaglioni. Phys. Rev. C 105, 054316 (2022).
[6] N. Le Anh, B. Minh Loc, N. Auerbach, and V. Zelevinsky. Phys. Rev. C 106, L051302 (2022).
[7] Y. Ayyad et al. Phys. Rev. Lett. 129, 012501 (2022).
[8] S. Heinitz, D. Kiselev, N. Kivel, and D. Schumann, Appl. Radiat. Isot. 130, 260 (2017).
[9] R. E. Azuma, E. Uberseder, E. C. Simpson, C. R. Brune, H. Costantini, R. J. de Boer, J. Görres, M. Heil, P. J. LeBlanc, C. Ugalde, and M. Wiescher, Phys. Rev. C 81, 045805 (2010))

Cluster states in carbon isotopes $^{13-15}$C studied with the ^{10}Be+^{9}Be reactions

M. Milin and D. Nurkić (UZ), S. Heinitz (PSI), E.A. Maugeri (PSI), D. Schumann (PSI), P. Čolović (IRB), D. Jelavić Malenica (IRB), N. Soić (IRB), M. Uroić (IRB), N. Vukman (IRB), S. Cherubini (LNS-INFN), A. Di Pietro (LNS-INFN), P. Figuera (LNS-INFN), L. Lamia (LNS-INFN), G. Pizzone (LNS-INFN), S. Romano (LNS-INFN), C. Spitaleri (LNS-INFN), A. Tumino (LNS-INFN)

Introduction

Clustering of nucleons into two or more groups within an atomic nucleus is nowadays accepted as a common and essential feature of structure of light nuclei [1]. The basic building block of cluster states is the α-particle. Configurations based on two-α or three-α underlying structures are recently in the focus of many experimental and theoretical studies of beryllium and carbon isotopes, respectively. The role of additional (valence) neutrons to such states is yet to be fully understood, making new experimental results for neutron rich isotopes of these elements highly desirable [2].

The ^{9}Be isotope has been chosen as the reaction target because of the known existence of a cluster structure ^{5}He+^{4}He inside its ground state. One step or two-step pick-up reactions of these cluster onto the radioactive ^{10}Be beam particles would result in the creation of the sought ^{14}C or ^{15}C isotopes, which could then be studied via its sequential decay into several different channels.

The ^{14}C nucleus is being particularly thoroughly studied in the last decade, starting with an early attempt to systematize its spectroscopy [3], through experiments investigating sequential decay reactions [4-6], to the very recent studies based on the ^{10}Be+^{4}He resonant elastic scattering [7-9]. The obtained experimental results are far from being consistent and one of the goals of this experiment is to help to resolve this inconsistency.

The existing experimental data on ^{15}C, on the other hand, is limited to more or less basic information on the low-lying states, below the α-decay threshold. A few papers discuss also higher lying states [10], but results on α-clustering have not been reported yet. The aim of the performed experiment was to obtain new experimental data that would help creating a consistent model of clustering in neutron rich carbon isotopes.

Experiment

The experiment was performed with the ^{10}Be beam from the LNS Tandem accelerator (Catania, Italy) at the beam energy of 54.3 MeV. The beam was made from the material containing radioactive ^{10}Be, obtained through the collaboration between LNS and PSI – the produced (radioactive) ^{10}Be beam was of excellent quality, well focused and having rather high intensity (>3 enA), providing experimental data of interest with good statistics. Details on the beam production can be found in ref. [11].

Self-supporting ^{9}Be targets with thickness of 400 μm/cm^2 were used, as well as a highly segmented detector set-up consisting of 4 double sided silicon strip detectors, DSSSDs, covering large solid angle and allowing the detection of two- and three-particle coincidences with large statistics.

The experimental setup consisted of four highly segmented telescopes covering polar angles from 20◦ to 90◦, which enable particle identification using traditional ΔE-E techniques. The E stage of the telescope was a double-sided silicon strip detector divided into 16 strips at each side, while the ΔE part was single-sided with 16 strips. A typical ΔE-E identification plot for just one strip is given in figure 1.

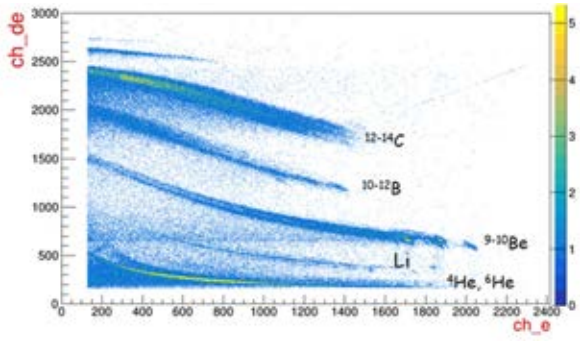

Figure 1: ΔE-E identification plot for one strip.

Results and discussion

The main goal of the proposed experiment is obtaining new spectroscopic information on the ^{14}C and ^{15}C states of predominately cluster character. Those should be populated through the α-particle (or ^{5}He) pick-up by the ^{10}Be projectiles, followed by sequential decay into different channels.

The analysis of the data is still in progress, but indications of a couple of interesting results are already seen. First of all, we do see the population of the ^{14}C high-lying states and their sequential decay into the ^{10}Be+^{4}He channel – the corresponding statistics seem

to be rather high and final extraction of these results are expected soon. Another clear result is the ^{10}Be+^{9}Be elastic and inelastic scattering and corresponding (partial) angular distributions. Here we present the final results for the ^{13}C nucleus, the carbon isotope of interest with the lowest excess of neutrons.

The ^{13}C states are populated in this experiment through the ^{9}Be(^{10}Be,^{6}He) α-transfer reaction – population of low lying states was suppressed due to their low spins and Q-value matching conditions. Figure 2 shows the ^{13}C excitation energy spectrum from the ^{6}He+^{4}He coincidences (with third particle, ^{9}Be, coming from the ^{13}C decay, being undetected).

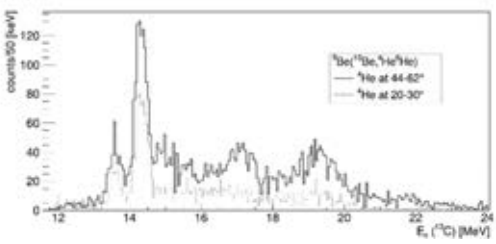

Figure 2: ^{13}C excitation energies from the ^{6}He+^{4}He coincident events

A pronounced selectivity seen in that spectrum is only marginally caused by the detection efficiency, so it should be a signature of the α-cluster character of the state at E_x= 14.13 MeV. The state is suggested [12, 13] to have J^{π}= 5/2^{-}, so it is not clear how it fits to the systematics [13,14] of the ^{13}C cluster states, since at that high excitation energies members of the rotational bands with cluster character are supposed to have higher spins (e.g. the 13.41 MeV state is suggested to have 7/2+ [6] or 9/2^{-} [13]). Further work is needed to clarify that point.

Other topics, like decays of ^{14}C and ^{15}C states by ^{6}He emission (which is clearly seen in figure 1), will be studied in later analysis. The quality of the data, together with large obtained statistics, implies the possibility of extracting many additional interesting new results, for the first time obtained with the radioactive ^{10}Be beam.

Acknowledgements

This work has been supported by the Croatian Science Foundation under project no. IP-2018-01-1257, by Scientific Center of Excellence for Advanced Materials and Sensors and by ENSAR2 Grant Agreement nb. 65400.

References

[1] M. Freer et al., Rev. Mod. Phys. 90, 035004 (2018)
[2] W. von Oertzen, M. Freer and Y. Kanada-En'yo, Phys. Rep. 432, 43 (2006)
[3] W. von Oertzen et al., Eur. Phys. J. A 21, 193 (2004)
[4] N. Soić et al., Phys. Rev. C 68, 014321 (2003)
[5] M. Milin et al., Nucl. Phys. A 730, 285 (2004)
[6] P.J. Haigh et al., Phys. Rev. C 78, 014319 (2008)
[7] M. Freer et al., Phys. Rev. C 90. 054324 (2014)
[8] A. Fritsch et al., Phys. Rev. C 93, 014321 (2016)
[9] H. Yamaguchi et al., Phys. Lett. B 766, 11 (2017)
[10] H.G. Bohlen et al., Eur. Phys. J. A 31, 279 (2007)
[11] P. Figuera et al., Nucl. Instr. Meth. Phys. Res. A 972, 164120 (2020), 43
[12] M. Freer et al., Phys. Rec. C 84, 034317 (2011)
[13] I. Lombardo et al., Phys. Rev. C 97, 034320 (2018)
[14] M. Milin, W. von Oertzen, Eur. Phys. J. A 14, 295 (2002)

Preparation and quantification of a ^{41}Ca sample

K. Kossert (PTB), M. Veicht (PSI&EPFL), J. Wilson (PSI&ETHZ), D. Cvjetinovic (PSI), I. Mihalcea (PSI), D. Schumann (PSI)

Introduction

The long-lived isotope ^{41}Ca decays with a half-life of $(9.94\pm0.15)\cdot10^4$ y [1] and is a reliable tool for geophysical applications such as radiometric age determination in the range of 10^5 to 10^6 years [2]. In addition, it plays an important role in astrophysics when trying to improve the understanding of the s-process nucleosynthesis of isotopes from sulphur to calcium. However, carrier-free amounts of ^{41}Ca are required for corresponding investigations to detect α-particles and protons produced by (n,α) and (n,p) reactions. Therefore, neutron activation of the stable ^{40}Ca cannot be used for sample production in this case [3,4].

Sample source

In the frame of the SNSF-funded project SINCHRON, considerable amounts of non-carrier added radionuclides were produced by irradiating metallic vanadium with high-energetic protons in dedicated positions of the SINQ target [5]. In addition to the actually targeted nuclide ^{32}Si, fractions of the scientifically interesting isotopes ^{44}Ti, ^{26}Al, and ^{41}Ca were also obtained in the course of the project. Details of the radiochemical separations are described in [5,6]. In order to determine the total amount of ^{41}Ca obtained within this campaign, an aliquot of the ^{41}Ca fraction was sent to the Physikalisch-Technische Bundesanstalt Braunschweig (PTB) for activity determination using Liquid Scintillation (LS) counting.

LS counting

For the LS measurements at PTB, a custom-built triple-to-double coincidence ratio (TDCR) counter was used. In addition, a Wallac 1414 spectrometer and a Tri-Carb 2800 TR spectrometer were used to apply the CIEMAT/NIST efficiency tracing (CNET) method. Details about these systems and further references can be found in a recent publication [7].

Results and discussion

^{41}Ca decays by electron capture and the subsequent atomic relaxation leads to the emission of low-energetic electrons and x-rays. As a consequence, the LS counting efficiencies are rather low and ^{41}Ca decay events contribute only to the low-energy part of related LS spectra [1,8].

Figure 1 shows an example of an LS spectrum recorded with the Wallac spectrometer in February 2022. The spectrum is compared with a spectrum of a pure ^{41}Ca solution [1]. While the pure ^{41}Ca sample has only the expected peak at very low channel numbers, our sample also has a significant contribution at higher channel numbers, which is likely due to one or more β-emitting radionuclides. Figure 1 also contains a spectrum from a pure ^{45}Ca LS sample, which matches well with the spectrum shape. In general, the TDCR method was found to be considerably more suitable than the CNET method in the case of ^{41}Ca [1,8]. However, such an impurity hampers an accurate activity determination by means of the TDCR method. Nonetheless, since the activity of the reference sample is well known from TDCR measurements, we can roughly estimate the activity of the LS sample (309(31) Bq) and determine the ^{41}Ca activity concentration (10.5(11) kBq/g) of the sample provided by PSI. Note that this approach requires that the ^{41}Ca LS samples have a similar quench level, which is important since the ^{41}Ca spectrum contains a number of single electron events. The single electron peak does not change its position when quenching a sample.

The estimated activity is stated for the reference date January 1, 2022. The relative uncertainty was estimated to be roughly 10% (k=1). A consistent result was obtained when applying the CNET method.

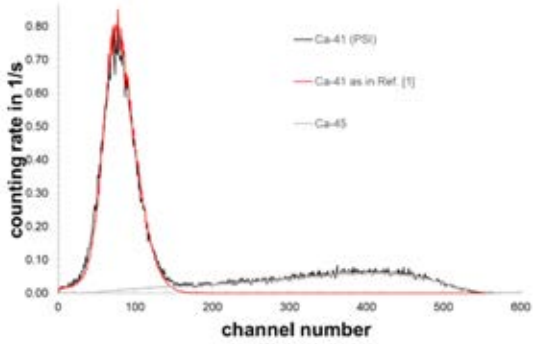

Figure 1: Spectra of the LS sample, which contains ^{41}Ca and ^{45}Ca. Spectra of pure ^{41}Ca and ^{45}Ca solutions are also shown.

We could not definitely identify the impurity at the high channel number. However, a new measurement of the same LS samples in October 2022 resulted in a significant reduction (more than a factor of 2.5) of the spectrum content. This indicates that at least one impurity has a relatively short half-life, thus supporting the hypothesis that ^{45}Ca ($t_{1/2}$=162.64(11) d, [9]) is present in the sample.

The ^{41}Ca activity concentration determined above corresponds to about $5\cdot10^{16}$ atoms per gram of

solution. With a total amount of roughly 3 MBq, we have around $2 \cdot 10^{19}$ atoms available, which we can provide for dedicated astrophysics experiments. However, a final characterization of the radioactive impurities as well as the content of stable Ca isotopes (preferably by inductively coupled plasma mass spectrometry) is still pending.

Acknowledgements

This project is funded by the Swiss National Science Foundation (SNSF) as part of SINCHRON (No. 177229) and received additional financial support from the European Union Horizon 2020 program under Marie Skłodowska-Curie grant agreement No. 701647.

References

[1] G. Jörg et al., Geochim. et Cosmochim. Acta, 88 (2012) 51-65.
[2] R. Michel et al., Radiochim Acta 87 (1999) 47
[3] S. Vermote et al., Physical Review C 85 (2012) 015803.
[4] C. Wagemans et al., Physical Review C 57 (1998) 1767-1770.
[5] J.M. Wilson et al., Radiochim. Acta (2023) https://doi.org/10.1515/ract-2022-0072.
[6] M. Veicht et al., Radiochim. Acta 10 (2022) 809
[7] K. Kossert et al., Appl. Radiat. Isot. 188 (2022) 110362.
[8] K. Kossert et al., Radiochim. Acta 97 (2009) 1-8.
[9] Bé, M.-M., et al., Monographie BIPM-5: Table of radionuclides, (Vol. 7, A = 14 to 245). Bureau International des Poids et Mesures, Sèvres, (2013) ISBN-13 978-92-822-2248-7.

Removal of Rh from Rh/Si mix in HCl/HNO3 matrix

D. Cvjetinovic (PSI), M. Veicht (PSI&EPFL), D. Schumann (PSI)

Introduction

Within the ongoing SINCHRON project, worldwide unique quantities of ^{32}Si have been produced and purified for the purpose of ^{32}Si half-life redetermination measurements. Production of ^{32}Si was achieved by using a high intensity proton beam available at PSI to irradiate a series of V-discs and induce spallation reactions. Besides ^{32}Si, several other valuable radionuclides were also produced as spallation products, including ^{26}Al, $^{41/45}$Ca and ^{44}Ti/^{44}Sc. A comprehensive radiochemical scheme detailing the purification and separation of ^{32}Si was developed and implemented by the Isotope and Target Chemistry group (ITC) at LRC [1]. Recovery and purification procedures for ^{26}Al, $^{41/45}$Ca and ^{44}Ti/^{44}Sc have also been developed and are currently pending publication.

Additional quantities of ^{32}Si are available at LRC in the form of a ^{32}Si/^{101}Rh radionuclide mix in 0.05M/0.05M HCl/HNO_3 solution that require development of a novel separation procedure. Complete separation of these radionuclides would be very beneficial for both current and new research. In literature, different resin-based separation schemes have been successfully applied to recover Rh from either HCl or HNO_3 matrix [2,3]. However, such a separation has not been reported for a mixed HCl/HNO_3 matrix. The reason behind this lies in the fact that Rh forms several different Cl^- and NO_3^- complexes [4,5], present in both cationic and anionic forms, making it difficult to apply a single ion-exchange resin for a one-step Rh recovery.

In this study, we tested the possibility of using a chelating anion exchange resin Purolite S 985 to separate Rh from Si by either varying the HCl/HNO_3 ratio or by changing the solution matrix to HCl/HF. Testing was done using the cold batch static model. ICP-OES was used to quantify and subsequently calculate the mass distribution coefficient (D) for both Rh and Si.

Experimental

The sorption of Rh and Si by the Purolite S 985 resin from the acidic solutions was measured after equilibration of a known volume of Rh/Si standard solution with a pre-weighed mass of resin. In short the procedure consisted of: weighing 50±2 mg of native resin into 2 mL plastic vials; addition of 0.5 mL of corresponding acid solution into the vial; vial shaking for 30 min; addition of 1 mL of a standard solution of 50 ppm Rh/ 50 ppm Si into the vials; shaking for 16 h; centrifugation of vials; removal of 0.5 mL of supernatant; dilution with 4.5 mL of 2% HNO_3; ICP-OES measurement of Rh/Si concentration. All measurements were done in a triplicate. The mass distribution coefficient (D, mL/g) was defined and calculated using equation (1) for both Rh and Si:

$$D = \frac{C_0 - C}{C} * \frac{V_{mL}}{m_g} \quad (1)$$

where C is the element concentration after contact with the resin (as determined by ICP-OES); C_0 is the initial element concentration, prior to resin contact; m_g is the resin mass in g; V_{mL} is the solution volume (1.5 mL). The D values are given as a mean of three measurements and all solutions and standards were freshly prepared prior to the measurement.

Results and discussion

Logarithmic values of mass distribution coefficients for Rh and Si are presented in table 1. It is shown that Rh adsorption in HCl is behaving as described in the literature [2]. Similar adsorption behaviour of Rh is observed in HNO_3 solutions as well, while Si adsorption is slightly higher compared to HCl solution.

Table 1: Mass distribution coefficients for Rh and Si in different acidic matrixes.

Matrix	C(M)	LogD(Rh)	LogD(Si)
HCl	0.01	3.97	0.21
	0.05	4.06	0.08
	0.10	2.22	0.02
HNO_3	0.01	3.98	0.33
	0.05	3.83	0.14
	0.10	2.25	0.17
HCl/HNO_3	0.01/0.05	4.18	0.40
	0.05/0.05	2.26	0.42
	0.10/0.05	2.22	0.40
HCl/HF	0.05/0.10	2.34	2.91
	0.10/0.10	2.33	2.79
	0.20/0.10	2.28	2.69

D values for Si significantly change when measured in an HCl/HNO_3 mix, compared to the same pH values of single acid solutions. Si shows increased adsorption under these conditions while D(Rh) seems to behave similar. This data indicates that the 0.01 M/0.05 M HCl/HNO_3 matrix composition seems to be a good candidate for dynamic column tests since Rh sorption is significantly higher than for the stock solution

(0.05M/0.05M HCl/HNO_3) while Si sorption is similar. Nevertheless, for future dynamic tests it should be extremely important to investigate the "ageing" effect on the Rh chloro complexes, since they are quite inert and it takes around 8-12 weeks [2,4] for the equilibrium to be established. Combined with the "ageing" effect and the presence of NO_3^- ions in the stock solution, a large array of possible Rh complexes can be present, as shown in table 2.

Table 2: Presumed Rh complexes in stock solution.

Cl^- complexes (C < 0.5M)	**NO_3^- complexes (C < 0.5M)**
$[Rh(H_2O)_2Cl_4]^-$	$[Rh(H_2O)_5(NO_3)]^{2+}$
$[Rh(H_2O)_4Cl_2]^{2+}$	$[Rh(H_2O)_4(NO_3)_2]^+$
$[RhCl_9]^{3-}$	$[Rh(H_2O)_3(NO_3)_3]$
after "ageing"	$[Rh(NO_3)_3]$
$[Rh(H_2O)Cl_5]^{2-}$	
$[Rh(H_2O)_3Cl_3]$	

Investigation of Rh sorption in HCl/HF mix has not yielded any promising results, since both Rh and Si behave rather similar, as can be seen from D values in table 1, making it impossible to separate Rh from Si. This is unfortunate since a matrix change to HCl/HF would be easily implemented in the existing radiochemical separation scheme, described in [1], following the evaporation to dryness step.

Conclusions

Promising results obtained from the static model indicate that it might be possible to separate Rh from Si in an HCl/HNO_3 mix using Purolite S 985 resin. Further investigation using cold dynamic tests and hot $^{32}Si/^{101}Rh$ stock solution are needed to provide the definitive answer. Considering that our $^{32}Si/^{101}Rh$ stock solution has been stored for more than a year, an "ageing" effect might also heavily influence the result. Purolite S 985 shows highest selectivity towards Rh anionic complexes and therefore the existence of any cationic or neutral species could hinder the Rh sorption.

Acknowledgements

This research was funded by the Swiss National Science Foundation (SNSF) as part of SINERGIA (No. 177229). The authors are grateful to the UK representative office of the Purolite Corporation for providing the Purolite S 985 resin.

References

[1] M. Veicht et al. Radiochim. Acta, 109(10), (2021) pp. 735-741
[2] O. N. Kononova et al. Hydrometallurgy 105.3-4, (2011). pp. 341-349.
[3] S. H. Lee & H. Chung, J. Nucl. Sci. Technol, 37(3), (2000), pp. 281-287.
[4] V. I. Shlenskaya, O. A. Efremenko, & S. V. Oleinikova, et al. Russ Chem Bull 18, (1969), pp. 1525–1527.
[5] D. Vasilchenko et al. Eur. J. Inorg. Chem 2016.23 (2016), pp. 3822-3828.
[6] S. Watanabe, et al. IOP Conference Series: Materials Science and Engineering. Vol. 835, (2020)

Measurement of the beta spectrum of ^{171}Tm

F. Juget (IRA), M. van Dijk (EPFL), E. A. Maugeri (PSI)

Introduction

The double focalising magnetic spectrometer at EPFL consists of a hemispherical magnet used for the measurement of the electron and positron emission spectra from radioactive sources [1]. The beta spectrum of a ^{171}Tm source, prepared at PSI, was investigated in the energy range of 33 keV to its end-point. Previously, only the beta decay to the exited state of ^{171}Yb was measured using the coincidence with the deexcitation γ-ray line [2-4]. For this work, the end-point energy has been evaluated, and several considerations about the theoretical shape of the spectrum are under investigation.

Experimental

The double focalizing magnetic spectrometer deflects the electrons from a source toward a detector over a deflection angle of 180° selecting the energy while simultaneously focussing in both horizontal and vertical planes and thus optimizing the collection on the detector (figure 1). The magnetic spectrometer used in this work is described in more details in [1].

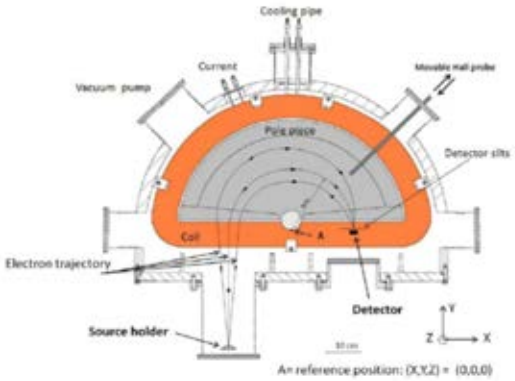

Figure 1: Schematic top view diagram of the spectrometer

For the measurement of the ^{171}Tm spectrum, a silicon detector with an active thickness of 500 μm is used. A Labview®-based acquisition system records the amplitude of the pulse height in the detector, which corresponds to the energy deposited by the electron. An offline analysis uses a window around the full energy deposition peak to select only electrons which deposited their whole energy in the detector (see [1] for more details). To reduce the background and the backscattering in material around the source location, a 5 mm thick Plexiglas cylinder is placed around the source with a hole of 1 cm diameter in front of the source.

The energy calibration and resolution of the detector is performed using conversion electrons at 45.01, 75.38, 240.41, 266.87, 320.03 respectively, from a ^{133}Ba source. The energy resolution is obtained using the sigma of the Gaussian fit of each peak. The sigma-dependence with the energy is fitted using the following relation: $\sigma_E = P_1\sqrt{E} + P_0.\mathrm{E} + P_2$. As the resolution is energy-dependent, an algorithm based on the method detailed in [5] is applied to correct the measured spectra in the offline analysis.

The efficiency of the spectrometer is calculated using a ^{60}Co source for which the energy spectrum can be precisely calculated. The ratio between the measured spectrum and the theoretical spectrum gives the relative efficiency versus the energy. Figure 2 shows the obtained efficiency compared to the one obtained using a ^{204}Tl source.

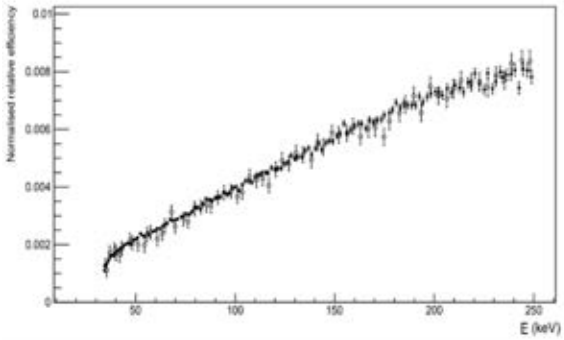

Figure 2: Efficiency versus energy obtained with ^{60}Co (black points) and ^{204}Tl (open points) spectra (left).

^{171}Tm was produced by thermal neutron irradiation of ^{170}Er at the high-flux research reactor Institut Laue-Langevin, France, and chemically separated at PSI following the method described in [6]. A source was prepared by drop deposition and drying on a support as described in [1]. The activity of the source is around 50 kBq.

Results and discussion

The spectrum shape is measured from 33 keV to 110 keV with steps of 2 mA of current, which corresponds to around 0.25 keV, during 72 min per step. Figure 3 gives the obtained spectrum after reconstruction with the efficiency obtained with the ^{60}Co source and corrected for the energy resolution. A Gaussian fit on the two electron conversion peaks gives the mean energies 56.66(16) and 64.60(21) keV, respectively (figure 3), which has to be compared with the expected energy between 56.2-57.8 keV for the

first peak and between 64.3-65.2 keV for the second peak [7].

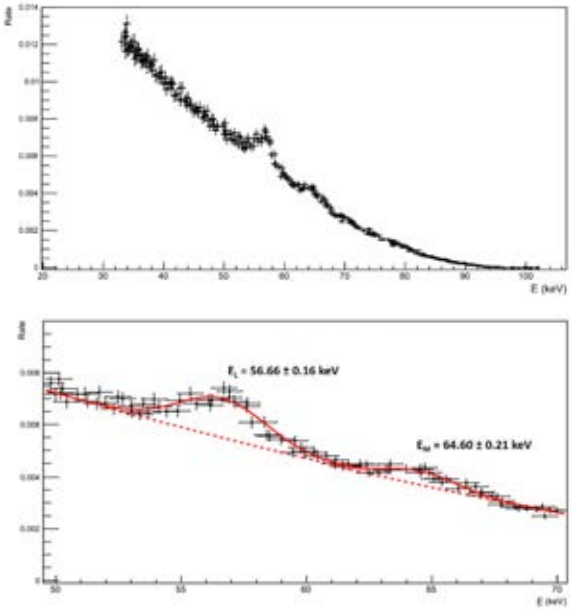

Figure 3: Measured spectrum of ^{171}Tm (top). Zoom on the two electron conversion peaks with the Gaussian fit.

The beta spectrum can be described using:

$$N(W)dW = K.F(W,Z).p.W.(W_0 - W)^2.C(W).X(W).r(Z,W)dW \qquad (1)$$

Where W is the total energy, W_0 the maximum energy of the beta spectrum, K is a constant, F(Z,W) the Fermi function, C(W) is the shape factor, X(W) the corrections for screening and exchange effects and r(Z,W) accounts for the atomic overlap effect. In the case of ^{171}Tm, considering the ξ-approximation, the shape factor correction is taken as C(W) = 1. The X(W) correction was calculated as described in [8-10]. The r(Z,W) correction was calculated as described in [11] and can be written as

$$r(Z,W) = 1 - \frac{1}{W_0 - W}.0.286155. \qquad (2)$$

Following the Kurie plot procedure [12], equation (1) can be rewritten as:

$$\sqrt{\frac{N(W)}{F(W,Z).p.W.C(W).X(W)}} = K\sqrt{(W_0 - W)^2 - 0.286155.(W_0 - W)} \qquad (3)$$

where K and W_0 can be obtained with a fit procedure and therefore infer the value of the maximum kinetic energy of the beta spectrum, E_{max}. Figure 4 gives the Kurie plot with the obtained fit in the energy range 33-95 keV. The obtained value of E_{max} is 97.62 keV and the uncertainties are under evaluation.

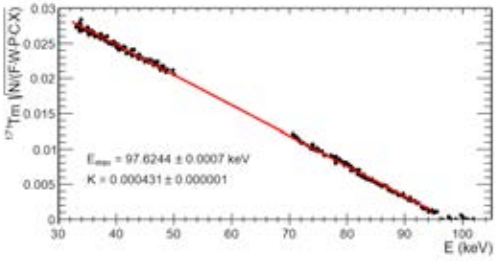

Figure 4: Kurie plot using the equation (2) with a fit from 33 keV to 95 keV. The uncertainty corresponds to the fit only.

The results presented here are still preliminary and further analysis is in progress in particular to calculate the end-point energy and its uncertainty and to compare the obtained experimental spectrum with the calculated shape using theoretical assumptions.

Acknowledgements

This experiment would not have been possible without the generous loan of ^{171}Tm from Carlos Guerrero (Univ. Sevilla), the neutron irradiation of ^{170}Er implemented by Ulli Köster (ILL Grenoble) and the radiochemical separation performed by Stephan Heinitz (PSI, now SCK-CEN Mol).

References:

[1] F. Juget et al., Nuclear Inst. and Methods in Physics Research A 942, 162384 (2019)
[2] W. G. Smith et al., Phys. Rev. 107, 1314-1315 (1957)
[3] R. L. Robinson, PhD thesis, Indiana University (1958)
[4] Hansen, G. (1964). Experimental investigations of decay schemes of deformed nuclei. Danish Atomic Energy Commission, Risø Reports Vol. 1964 No. 92
[5] D. E. Wortmann et al., Nuclear and Instrument Methods 26, 257-262 (1964)
[6] S. Heinitz et al., Radiochim. Acta, 105 (10), 801-811 (2017)
[7] https://www-nds.iaea.org/relnsd/vcharthtml/VChartHTML.html
[8] X. Mougeot et al., Phys. Rev. A90, 012501 (2014)
[9] E. Aprile et al., Phys. Rev. D 102, 072004 (2020)
[10] S. J. Haselschwardt et al., Phys. Rev. C 102, 065501 (2020)
[11] L. Hayen et al., Rev. Mod. Phys. 90, 015008 (2018)
[12] P. Kurie et al., Phys. Rev. 49, 368-381 (1936)

First attempts of molecular plating of potassium on carbon backing

E.A. Maugeri (PSI), J. Huber (PSI&ETHZ), M. Veicht (PSI&EPFL), N. Cerboni (PSI&ETHZ), A. Vögele (PSI)

Introduction

The primordial, long-lived isotope ^{40}K ($t_{1/2}$ = 1.25 x 10^9 y) originates from nucleosynthesis processes in massive stars, where it is produced in the slow neutron capture process during helium core and carbon shell burning phases [1]. It is produced by neutron capture from stable ^{39}K, and destroyed mainly by $^{40}K(n,\alpha)$ reactions, and to a lesser extent via $^{40}K(n,p)$ and $^{40}K(n,\gamma)$ reactions. Notably, ^{40}K is one of the main isotopes responsible for heat generation in earth-like exoplanets [2] due to the energy release occurring during its β-decay (so-called radiogenic heating). Radiogenic heating is essential to sustain the crustal recycling (e.g., plate tectonics), hence the initial quantity of ^{40}K in an exoplanet impacts on its habitability.

Data on $^{40}K(n,\alpha)$ and $^{40}K(n,p)$ cross sections at astrophysical neutron energies are scarce, thus a new measurement of these important reactions is planned at the high flux beam line EAR-2 at the n_TOF facility [3]. A key element for performing this measurement is the challenging manufacture of a ^{40}K target (about 80 µg) homogeneous and thin enough to let both α and proton particles through without substantial energy loss before being detected.

We report here on the first attempt at producing a potassium target with the above-mentioned characteristics.

Currently, only ^{40}K with a maximum enrichment of 16.1% is commercially available at relatively high costs. This imposes target production methods with high yields, among which molecular plating (MP) was chosen for the test experiment reported here. MP is an electrochemical method where the target element is deposited as a molecular compound from an organic electrolyte [4]. This method has allowed obtaining uniform and homogenous thin films of actinides [5], lanthanides [6], and alkaline earth metals [7-9], with almost quantitative yields. This has been the first time, to the best of our knowledge, that MP is used to produce thin films of potassium.

Experimental

The used MP set-up, described in detail in [7], was a two-electrodes cell characterized by an inner diameter of 20 mm, which defined the area of the plated layer. The backing plate was a 27 mm diameter and 0.75 mm thick glassy carbon disk. ^{nat}K, in the form of KCl, was used instead of the more expensive ^{40}KCl. Considering that the final target should have a ^{40}K density area of about 6.4 µg cm^{-2} and that the previously estimated MP yield was about 80%, the quantity of starting ^{nat}KCl was calculated as about 300 µg.

Homogeneity of the deposited layer and yield of the MP were monitored using trace amounts of the γ-emitting isotope ^{42}K ($t_{1/2}$=12.36 h). In particular, the starting 300 µg of ^{nat}KCl (≥99%, Merck®) was irradiated with thermal neutrons ($2.07 \cdot 10^{16}$ neutrons cm^{-2}) at SINQ for 50 min, producing about 50 kBq of ^{42}K.

The plating solution was prepared solubilizing the irradiated KCl in 10 µL of 0.01 M HCl (37%, Merck®) and dissolving the obtained solution in 10 mL of N,N-dimethylformamide (anhydrous 99.8%, Merck®).

The MP parameters, current density and deposition time, were previously defined through preliminary tests, as 0.8 mA cm^{-2} and 90 min, respectively.

The surface morphology of the deposited film was characterized by scanning electron microscopy (SEM; ZEISS NVision-40). Images were taken at 50x and 750x magnification. The distribution of potassium in the deposited layer was investigated by radiographic imaging with the GE Typhoon™ FLA 7000 Imaging Plate Reader, having a spatial resolution down to 25 µm, in combination with reusable Fujifilm imaging plates BAS-SR. The deposition yield was calculated measuring the ^{42}K activity in the plating solution before and after the experiment, using a Canberra coaxial HPGe-detector. The Genie2000® software package was used to analyse the obtained data.

Results and discussion

Potassium was successfully plated, probably as KOH, onto the glassy carbon disk with a deposition yield of 85%.

The obtained film looked bluish to the naked eye, indicating a thickness of some tens of nanometres. When exposed to standard temperature and pressure, the film turned greyish, revealing the deposited compound's hygroscopy.

The SEM image taken in the central area of the sample at 50x magnification, figure 1, indicates an overall homogeneous deposited film, resembling the roughly and scratchy surface of the glassy carbon backing.

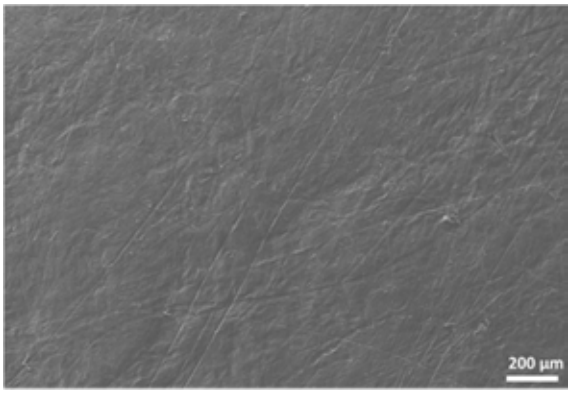

Figure 1: SEM image, taken at 50x magnification, of the molecular plated layer

The SEM image taken in the same area of figure 1, at 750x magnification, figure 2, reveals a scaly deposition, which, noteworthy, does not result in cracking and flaking of the deposited layer, proving the stability of the obtained layer.

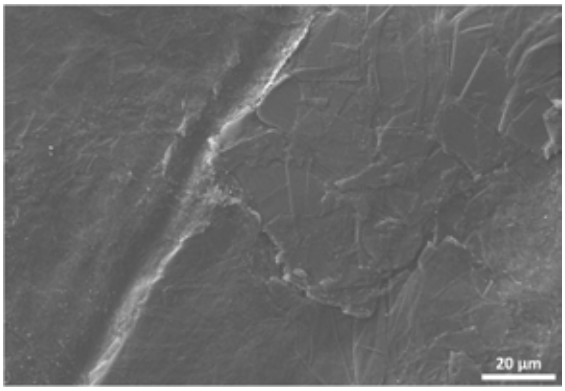

Figure 2: SEM image, taken at 750x magnification, of the molecular plated layer

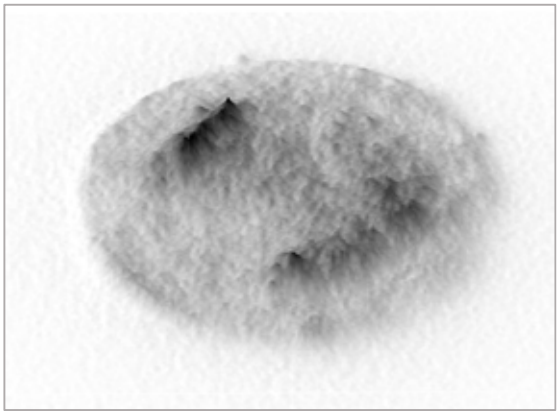

Figure 3: Radiographic imaging of the molecular plated layer

Figure 3 shows the radiographic imaging of the plated layer, indicating a rather uniform spatial distribution of potassium, although one area, characterized by higher activity (darker area) is clearly visible.

The formation of this local concentration of potassium activity is most probably due to the static conditions used during the molecular plating.

Conclusions

It was proven that potassium can be molecular plated on carbon backing. However, the experimental procedure must be improved to obtain higher deposition yields. The molecular plating method allows yield usually above 95%, indeed. It is also essential to get a better distribution of potassium in the deposited layer, for instance, by stirring the plating solution either with an ultrasonic tip stirrer, as suggested in [6], or using a rotating disk anode [10]. Considering the hygroscopic nature of the deposited material, it is necessary to perform the molecular plating in a glovebox with a low level of water.

Acknowledgement

The work is partially funded by EC Horizon 2020 (Grant agreement 847552 — SANDA — NFRP-2018).

References

[1] M. Pignatari et al., Astroph. J. Suppl. S. 225, 24 (2016)
[2] E.A. Frank et al., Icarus 243, 274 (2014)
[3] C. Lederer-Woods et al., Proposal to the ISOLDE and Neutron Time-of-Flight Committee, CERN-INTC-2022-047/INTC-P-645 (2022)
[4] W. Parker et al., Nucl. Instr. Meth. 16, 355 (1962)
[5] J. Runke et al., J. Radioanal. Nucl. Chem. 299, 1081 (2014)
[6] Z. Talip et al., Anal. Chem. 93, 10798 (2021)
[7] E.A. Maugeri et al., JINST 12, P02016 (2017)
[8] LRC 2023 Annual Report
[9] W. Parker et al., Nucl. Instr. Meth. 26, 314 (1964)
[10] M.T. Crespo, Appl. Radiat. Isot. 70, 210 (2012)

Targets for the muX experiment

J. Huber (PSI&ETHZ), N. Cerboni (PSI&ETHZ), M. Veicht (PSI&EPFL), E. A. Maugeri (PSI), A. Knecht (PSI) and the muX collaboration

Introduction

Muonic atoms are the bound state between a negative muon and an ordinary nucleus. They can be readily produced by stopping a negative muon beam in the desired target material. Once stopped, the muon is quickly captured by one of the neighbouring nuclei and cascades down from an initial high orbital to its ground state. In the last part of this cascade, X-rays with characteristic energies corresponding to the difference in binding energy between the two levels of the transition are emitted. Since muons are 207 times heavier than electrons, these energies are around 207 times higher than corresponding energies in electronic atoms. Additionally, with the muon orbiting the nucleus as well 207 times closer than a corresponding electron, the sensitivity to properties of the nucleus, such as its charge radius, is greatly enhanced. The absolute charge radius of a nucleus and other properties can thus be measured with high precision by analysing the muonic X-rays emitted during the cascade.

Within the muX collaboration, a development program has been completed over the past few years, which enables muonic atom spectroscopy using HPGe detectors for heavy, radioactive elements that are available only in microgram quantities [1]. The production of the corresponding targets in the order of $\mu g/cm^2$ pose a formidable challenge as contaminations have to be reduced to negligible levels in order to not prevent the muons from forming a muonic atom with the desired nucleus. A successful measurement of a ^{248}Cm target, produced in the radiochemistry group of the University of Mainz through a combination of drop-on-demand (DOD) and molecular plating (MP) with a total mass of 15 µg, was completed in 2019 [2]. However, several attempts of measuring muonic X-rays from a ^{226}Ra target, the main goal of the muX collaboration, were so far unsuccessful.

For these reasons, tests with barium targets were performed in 2022 with different amounts ranging from 5 to 50 µg. The barium targets were produced in the laboratory of radiochemistry at PSI by molecular plating [3].

Experimental

The used MP set-up [4] is a two-electrodes electro-chemical cell characterized by a top cylinder with an inner diameter of 16 mm connected with a base containing a copper cathode. The backing plate, used as substrates for the barium deposition, is a 16 mm diameter and 1 mm thick glassy carbon disk, which is placed on the top of the cathode. An O-ring guarantees the sealing between the two parts, cylinder and base. The anode, made coiling a 1 mm thick palladium wire into a spiral with a final diameter of about 15.5 mm, faces the cathode at a distance of about 10 mm. The molecular plating experiments were performed in "constant current mode". MP parameters, such as voltage, current density and deposition time were previously defined through preliminary tests to maximize the deposition yield while producing thin, uniform and homogenous films.

Homogeneity and yield of these test experiments were monitored using trace amounts of the γ-emitting isotope ^{133}Ba.

Results and discussion

Figure 1 shows a radiographic imaging of a test sample, obtained with a GE Typhoon™ FLA 7000 Imaging Plate Reader with spatial resolution down to 25 µm in combination with reusable Fujifilm imaging plates (IP) BAS-SR. The result shows a rather homogeneous spatial distribution of ^{133}Ba over the entire sample surface, except at the rim region, where two areas can be distinguished, one characterized by higher activity with respect to the whole sample, and the other one with lower activity.

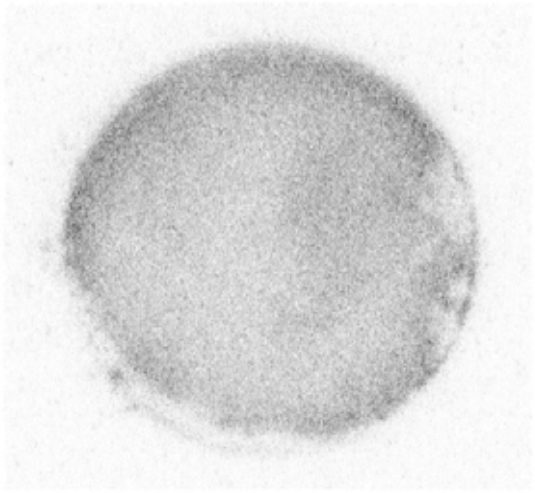

Figure 1: Radiographic image of a Ba molecular plated film, doped with ^{133}Ba.

The targets were tested in the muX setup during the beamtime of 2022. Figure 2 shows the measured muonic X-ray spectra from the 5 µg target.

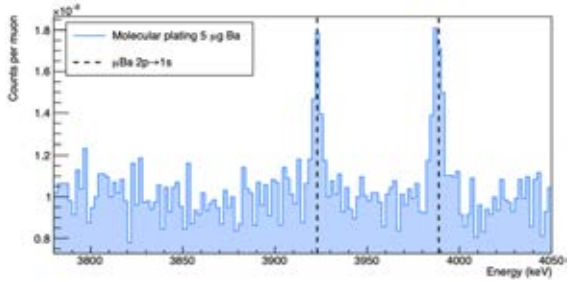

Figure 2: Energy spectrum of the region around the 2p→1s transition of muonic barium for the 5 µg target. The muonic X-rays could clearly be detected with good signal to background ratio.

Nice peaks with good signal to background ratio from the 2p→1s transitions in muonic barium could be detected even for this low target mass comparable to the maximum amount allowed for ^{226}Ra. This constitutes the first time in the history of the muX experiment that such a low mass target produced by radiochemical methods could be successfully measured – despite several attempts using MP and DOD techniques – and marks a major milestone towards the successful measurement of a ^{226}Ra target and the corresponding first extraction of its charge radius and quadrupole moment.

The collaboration between muX and the LRC of PSI will continue with the preparation of ^{226}Ra targets for the next beamtime and exciting new radioisotopes and prospects in the future.

Acknowledgements

We thank all the members of the muX collaboration for their efforts. The measurements would not have been possible by the generous loan of germanium detectors from the Technical University Munich (Germany) and Joint Institute for Nuclear Research Dubna (Russia) and the detectors and equipment from the MIXE collaboration.

References

[1] A. Adamczak et al., arXiv:2209.14365 (2022).
[2] A. Adamczak et al., SciPost Phys. Proc. 5, 022 (2021)
[3] W. Parker and R. Falk, Nucl. Instr. Meth. 16, 355 (1962).
[4] E. A. Maugeri et al., JINST 12 (02), P02016 (2017).

Reduction of metallic holmium from ionic liquids – a proof of concept

N. Cerboni (PSI&ETHZ), E. Bidari (TUBAF), P. Dutheil (PSI&ETHZ), N. Frenzel (TUBAF), M. Pannach (TUBAF), G. Frisch (TUBAF), P. Steinegger (PSI&ETHZ), E. A. Maugeri (PSI)

Introduction

The need for precise and controlled dosimetry has grown due to recent developments regarding the use of novel radiolanthanides (e.g., ^{155}Tb, ^{161}Tb, ^{161}Ho) for targeted therapy with Auger electrons [1]. So far, only few electron spectra of Auger-emitting radioisotopes of lanthanides (Lns) have been experimentally determined [2]. One of the main challenges concerns the source production. The method for source preparation should provide (1) thin films with a uniform Lns surface distribution in order to minimize self-absorption and hence, peak broadening in the Auger electron spectra, (2) a high chemical purity to reach highest specific activities, and (3) high yields, due to the expensive provision of needed radionuclides.

Herein, we propose the electrolytic deposition of thin films of metallic Lns as a promising approach for the source production for Auger electron spectroscopy. Since Lns have a very negative standard reduction potential (i.e. between - 2 $V_{vs.SHE}$ and - 2.5 $V_{vs.SHE}$ [3]), aqueous electrolytes cannot be used. These low potentials would strongly favor the hydrogen evolution reaction at the cathode and, thus, disturb the deposition process. In addition, metallic Lns readily react with water, forming hydroxides or oxides. These problems may be circumvented by using ionic liquids (ILs) as an alternative for aqueous electrolytes. In fact, amongst other properties, ILs possess large electrochemical stability windows [4], which allow for the required low potentials, enabling a complete Ln reduction. The challenging task of electrodepositing metallic Lns has been only studied for a limited number of elements [5]. This work focuses on the electrochemical deposition of thin films of metallic Ho from ILs. These preliminary results represent the basis for further, in-depth investigations of this system.

Experimental

Studies on the electroreduction of Ho in 1-butyl-1-methylpyrrolidinium bis(trifluoromethyl-sulfonyl)imide ([BMP][NTf_2], IoLiTec, 99%, figure 1) were performed at the TU Bergakademie Freiberg (TUBAF). All experiments were carried out in a glovebox under an inert N_2 atmosphere (H_2O and $O_2 \leq 0.1$ ppm). The IL was dried under vacuum at 80 °C for 6 h prior to usage.

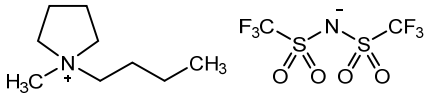

Figure 1: Structure of [BMP][NTf_2]

$Ho(NTf_2)_3$ was synthesized by a ligand exchange reaction in order to increase the solubility of Ho in [BMP][NTf_2]. To do so, Ho_2O_3 (0.5 mmol, Sigma Aldrich, ≥ 99.9%) was suspended in 5 mL H_2O and mixed with a solution of $HNTf_2$ (2.97 mmol, Sigma Aldrich, ≥ 95%) in 5 mL H_2O in a three-necked flask, while stirring and heating at 80 °C overnight. Subsequently, the water and any excess of $HNTf_2$ were removed from the clear solution, under vacuum at 80 °C, resulting in a white powder (yield: 0.8451 g, 79.5%). After transferring the product into the glovebox, a 0.1 M solution of $Ho(NTf_2)_3$ in ca. 2.5 g of [BMP][NTf_2] was prepared. The H_2O content of the pure and Ho-containing IL was analyzed by coulometric Karl-Fisher titration (C20, Mettler Toledo) prior and after each electrochemical experiment. As working electrode (WE), an Au wire (1 mm diameter) was used for the deposition. For all presented experiments, a Pt wire counter electrode and an Ag wire quasi-reference electrode (QRE) were used in combination with a potentiostat (Gamry Instruments, Interface1000). In addition, the deposition process was monitored by means of an electrochemical quartz microbalance (EQCM, Gamry Instruments, eQCM 10M) with an EQCM Au electrode (ICM, ca. 5 mm diameter). This experiment allowed for the simultaneous measurement of both current, as in cyclic voltammetry (CV), and mass change as a function of the applied voltage.

The surface morphology of the resulting deposits was analyzed by scanning electron microscopy (SEM, Tescan Vega SB) operated with a secondary electron detector at 10 kV accelerating voltage. Subsequently, energy-dispersive X-ray spectroscopy (EDX, Si(Li) INCAx-sight, Oxford Instruments) was used to investigate the elemental composition of the deposits.

Results and discussion

The water content greatly influences the electrochemical properties of ILs and, thus, needs to be minimized and carefully monitored. The water content of the pure and the Ho-containing IL was 197.0 ppm and 2627.3 ppm, respectively. This suggests that the Ho

salt still contained coordinating water, which was only released upon dissolution.

To better understand the deposition process, EQCM experiments were performed for both the [BMP][NTf_2] without and with Ho (figure 2). In order to compare the two QCM responses, water was added to the pure IL, to match the water content of Ho-[BMP][NTf_2]. It is worth noting that the QRE showed some electrochemical instability and, hence, the potentials of different measurements could not be compared directly. For the pure IL, a reduction peak and a small decrease in mass are visible at – 1.1 $V_{vs.\ Ag\ wire}$, which could be attributed to the reduction of water to hydrogen. The decomposition of the IL starts at ca. – 2.1 $V_{vs.\ Ag\ wire}$, which is correlated to a second and more pronounced mass decrease up to – 2.6 $V_{vs.\ Ag\ wire}$. This is in disagreement with previous CV studies of dry [BMP][NTf_2] (not reported here), where the decomposition starts at ca. – 3 $V_{vs.\ Ag\ wire}$. This unexpected behavior may come either from the addition of water to the IL or because of the instability of the QRE. However, more experiments need to be carried out in order to understand this behavior. After that, the mass starts to increase with further lowering of the applied potential before returning to its initial value once the potential is reverted to 0 $V_{vs.\ Ag\ wire}$. No significant oxidation peak is found, which indicates an electrochemically irreversible decomposition of the IL into soluble species, which reversibly adsorb to the electrode. The reversibility of this process is confirmed by EDX analysis after the EQCM experiment (figure 2, bottom left), where no significant amount of deposited material was detected on the electrode surface.

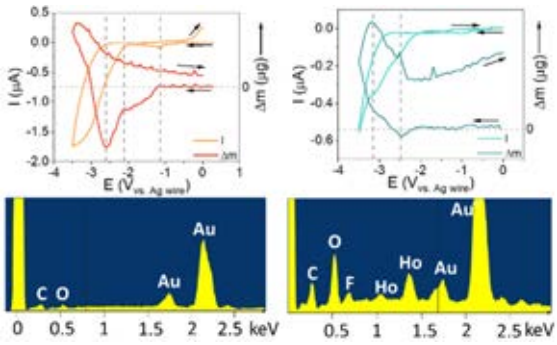

Figure 2: EQCM responses recorded at 50 mV s^{-1} for the pure [BMP][NTf_2] with addition of water (*left*) and Ho-[BMP][NTf_2] (*right*) and the corresponding EDX spectra of the used Au WE.

The EQCM experiment of Ho-[BMP][NTf_2] does not show the same behaviour of the pure IL between 0 and – 2 $V_{vs.\ Ag\ wire}$, even though the water content is similar. Probably, the water coordinated to Ho does not reach the electrode at this scan rate, while for the water added as pure contaminant s, IL is most probably "unbound" and can be reduced. At – 2.5 and – 3.1 $V_{vs.\ Ag\ wire}$ two reduction peaks, correlated with a mass increase, can be seen. These could be attributed to the simultaneous reduction of metallic Ho and the degradation of the IL. As in case of pure [BMP][NTf_2], no oxidation peaks are encountered while returning to 0 $V_{vs.\ Ag\ wire}$. However, the mass difference increased from the start to the end point, which indicates an electrochemically irreversible formation of a deposit. In fact,the elements Ho, C, O and F were clearly identified by means of EDX on the electrode surface after the EQCM experiment (figure 2, bottom right). Ho complexes were possibly produced upon the reaction of metallic Ho with decomposed IL.

Using the data obtained from the CV during the EQCM experiment, an electrodeposition of Ho was attempted by applying a constant voltage of - 3.1 $V_{vs.\ Ag\ wire}$ on Ho-[BMP][NTf_2] for 1.5 h. Indeed, a black deposit was obtained, which changed to white upon washing with dry acetone. A SEM and EDX analysis (figure 3) revealed a rough morphology of the formed deposit. This may be attributed to the washing and subsequent oxidation of the deposit. Meanwhile, the EDX spectrum proves the presence of Ho, which indicates its successful deposition. However, the deposit also contains C, O, F and S, which possibly come from the co-deposition of Ho complexes either formed upon decomposition of the IL, or from the washing procedure and handling in air.

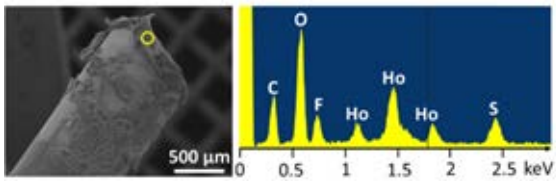

Figure 3: SEM image (*left*) of the Au wire after applying – 3.1 $V_{vs.\ Ag\ wire}$ for 1.5 h to Ho-[BMP][NTf_2] and the EDX spectrum (*right*) of a selected area (yellow circle).

Conclusions and outlook

Ho was successfully deposited from [BMP][NTf_2] on a Au WE. However, there is a simultaneous decomposition of the IL, which leads to a co-deposition of various Ho compounds in the formed deposit. Future experiments will focus on the influence of water and electrode material on the deposition and on more reliable CV measurements of Ho-[BMP][NTf_2]. Thus, the gathered knowledge would greatly help identifying experimental conditions which may prevent the decomposition of IL and facilitate the reduction-deposition of metallic Ho. Finally, the deposit will be characterized by means of X-ray photoelectron spectroscopy, which will allow for the identification of the oxidation state of deposited Ho.

References

[1] D. Filosofov et al., Nucl. Med. Biol. 94, 19 (2021)
[2] T. Vylov et al., Catalogue of radionuclide LEES; Dzhelepov (2003)
[3] P. Vanysek, CRC handb. chem. phys. 8 (2000)
[4] M. Freemantle An introduction to ILs; RSC (2010)
[5] A. P. Abbott et al., Annu. Rev. Mater. Res. 43, 24 (2013)

Systematic studies of molecular plating of gadolinium

J. Huber (ETHZ), N. Cerboni (PSI&ETHZ), M. Veicht (PSI&EPFL), P. Steinegger (PSI&ETHZ), E. A. Maugeri (PSI)

Introduction

For many nuclear and nuclear astrophysics experiments, such as half-life and nuclear reaction cross section measurements, it is important to be able to produce thin, uniform targets with a method allowing high deposition yield. Molecular plating (MP) is an electrochemical method with high yields for the deposition of thin and homogeneous films of elements with a reduction potential exceeding the stability window of water [1, 2]. Thus, it is applicable to lanthanides and actinides alike, which are among the most investigated elements in the mentioned research fields. Although MP is an over 80-years old method, the underlying chemical reactions are scarcely known. It is assumed that the water present in the plating solution gets reduced to hydrogen and hydroxide. The formed hydroxide ion then reacts with the metal cation forming a metal hydroxide which insoluble in the organic solvent and, thus, precipitating as a thin layer [3]. Here, we report on systematic studies aimed at furthering our understanding of the influence of the different constituents of the plating solution on the resulting electric current during the MP of gadolinium on glassy carbon backings.

Experimental

The used two-electrodes setup is described in detail in [5]. The plating solution investigated in this work consisted of three main constituents: (1) 10 mL of N,N-dimethylformamide (DMF), an organic solvent allowing to produce smooth surfaces with high yields [4], and (2) 0.5 mg of $GdCl_3 \times 6\ H_2O$, previously dissolved in (3) 10 µL of 0.01 M HCl. As a backing, a glassy carbon foil with a thickness of 0.75 mm and 27 mm in diameter was used. The MP experiments were performed in potentiostatic mode, i.e. applying a constant potential of 100 V for a defined time of 120 min while recording the output current. Each experiment was performed with different combinations of plating solution constituents (table 1) and was repeated twice, with and without mechanical stirring.

In the first experiment, Exp_1, the potential was applied to 10 mL of pure DMF. In the second experiment, Exp_2, 10 µL 0.01 M HCl were added to the 10 mL of DMF. Exp_3 was performed dissolving about 0.5 mg of $GdCl_3 \times 6\ H_2O$ in 10 mL of DMF. All components were included in Exp_4, i.e. the Gd salt, dissolved in 10 µL 0.01 M HCl, was added to 10 mL DMF. The water content in DMF, which may influence the output current, was determined by coulometric Karl-Fischer (KF) titration with a C10S titrator (Mettler Toledo).

Table 1: Composition of the different plating solutions. The water content of the solution is composed of the measured amount in DMF and the calculated amount in the mineral acid. The contribution from the crystal water was not significant and thus neglected.

Experiment code	Plating solution	Water content in the plating solution
Exp_1	10 mL DMF	5.4 mg
Exp_2	10 mL DMF, 10 µL 0.01 M HCl	15.4 mg
Exp_3	10 mL DMF, $GdCl_3 \times 6\ H_2O$	5.4 mg
Exp_4	10 mL DMF, $GdCl_3 \times 6\ H_2O$ dissolved in 10 µL 0.01 M HCl	15.4 mg

The deposited layers resulting from Exp_3 and Exp_4 were analysed by scanning electron microscopy (SEM). The deposition yields of these experiments were determined by inductively coupled plasma optical emission spectroscopy (ICP-OES) on the plating solution.

Results

The titration of the DMF resulted in a water content of 0.54 mg/mL. The current trend of both Exp_1 and Exp_2 did not differ significantly depending on the stirring, and was constant at about 0.15 mA (see figure 1 a and b).

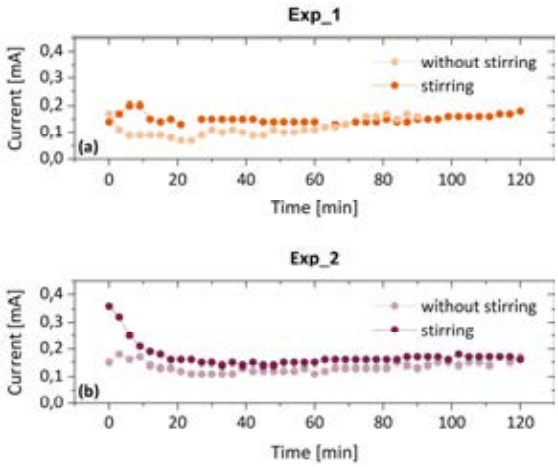

Figure 1: Panel (a): current trends of Exp_1. Panel (b): current trends of Exp_2. Both experiments with and without stirring.

The measured average current of Exp_3 (see figure 2 a), was about one order of magnitude higher than during

the first two experiments, namely 1.5 mA. The current trend increased, with no significant difference due to the stirring, before saturating after 45 min.

The current measured during Exp_4 (see figure 2 b), was slightly higher than the one encountered in Exp_3, i.e. about 2 mA. In this case, the current was rather highly influenced by the stirring, being slightly higher for the experiment with static conditions. The trend observed during Exp_4 could be divided into three sections, i.e. (1) an increase during the first 40 min, (2) a constant phase followed by (3) a second, flatter increase, after 80 min. This trend was less pronounced for the unstirred experiment.

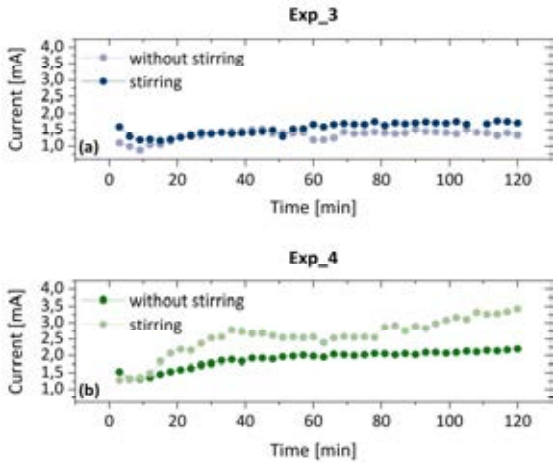

Figure 2: Panel (a): current trends of Exp_3. Panel (b): current trends of Exp_4. Both experiment with and without stirring.

The deposition yields of Exp_3 and Exp_4 were almost quantitative (about 99.9%). The photographic images, (see figure 3) showed that the layers resulting from Exp_3 and Exp_4 were in the nanometer range [6] and very homogeneous, independently of the stirring conditions and the presence of the mineral acid.

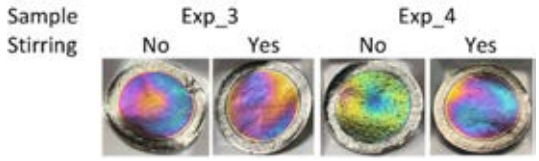

Figure 3: Photographic images of the plated Gd samples.

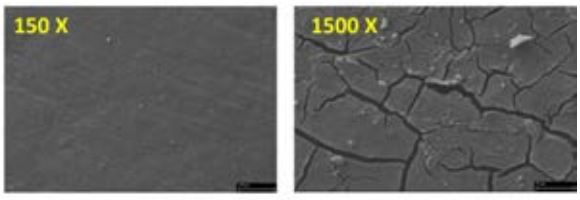

Figure 4: SEM images of the stirred Exp_4. Left image: 150 magnification, right image: 1500 magnification.

The SEM images of the stirred sample from Exp_4 (see figure 4) revealed a smooth deposited layer, having only few, not interconnected cracks, thus, indicating a good adherence of the deposited material on the carbon backing. Similar results, not presented here, were obtained for Exp_3.

Discussion

Exp_1 and Exp_2 were performed to measure the current resulting from applying 100 V to the organic solvent only and as well to the combination of the organic solvent and the mineral acid, respectively, to see if this current could be influenced by stirring. Our assumption, based on existing literature [2, 7], was that the measured current would mainly result from the reduction of water. In this respect, the obtained results confuted this hypothesis. In fact, the currents measured in the first two experiments were almost identical, although the water contents of Exp_2 was about three time higher than the one in Exp_1. Furthermore, the current measured in Exp_1 and Exp_2 was about one order of magnitude lower than the one encountered Exp_3 and Exp_4 despite similar water contents. The main difference between the first and the last two experiments was the presence of $GdCl_3 \times 6\ H_2O$ in the latter two. This indicates that the current produced during a MP is independent on the water content, at least in the herein used concentration range, and it is correlated with the presence of the metal salt. To the best of our knowledge, this has been the first time that a correlation between the current occurring during MP and the presence of the metal salt, which has been always considered as electrochemically inert, was proven.

The observed differences between the stirred and not stirred plating solutions of Exp_4 could be due to kinetic factors induced by faster diffusion in the stirred experiment. More experiments need to be performed to give a univocal interpretation of the trend observe during Exp_4, such as identify in which step Gd is deposited.

Another important result of this study is the confirmation that MP is a valid method for the production of thin and homogenous film of lanthanides, with very high yields.

Acknowledgement

The work is partially funded by EC Horizon 2020 (Grant agreement 847552 — SANDA — NFRP-2018).

References

[1] N. Trautmann, et al., Nucl. Instrum. Meth. 282, 102 (1989)
[2] A. Vascon, JGU, PhD dissertation, (2003)
[3] P. G. Hansen e al., J. Inorg. Nucl. Chem. 12, 30 (1959)
[4] G. De Bodin De Galembert, EPFL, Master thesis (2021)
[5] E. A. Maugeri et al., JINST 12, P02016 (2007)
[6] A. J. Antonczak et al., Appl Phys A 115, 1003 (2014)
[7] Y. He et al., J. Alloys Compd. 878, 160393 (2021)

Distribution of Tb in the intermetallic Tb-Pd compound produced via coupled reduction

B. Szekér (PSI&ETHZ), N. Cerboni (PSI&ETHZ), C. C. Hillhouse (PSI), P. V. Grundler (PSI), N. P. van der Meulen (PSI), R. Dressler (PSI), E. A. Maugeri (PSI)

Introduction

Intermetallic compounds (ICs) are of great interest in irradiation experiments, where they are used as target material and need to withstand high stress levels. They have various advantages over other targets, such as high thermal and electrical conductivity, high chemical and mechanical stability. ICs are solids made of at least two elements with a well-defined stoichiometry and structure that differs from the structure of their constituents [1]. The formation of ICs is only possible between elements differing considerably in size and electronegativity. ICs can be obtained following different methods [2]. This work implemented the procedure suggested by Usoltsev [3], i.e. molecular plating (MP) followed by coupled reduction (CR), for producing the intermetallic Tb-Pd. The samples obtained with this procedure were then characterized in terms of distribution of Tb by means of α-spectrometry. A homogeneous distribution of Tb would suggest a complete reaction and the formation of a regular structure, indicating the formation of envisaged IC. However, this would not be a definitive and univocal proof of the IC formation, which can only be given through a crystallographic investigation, as reported elsewhere in this annual report [4].

Experimental

The production of the intermetallic Tb-Pd (atomic ratio Tb/Pd = 0.008) can be divided into two parts, as depicted in figure 1.

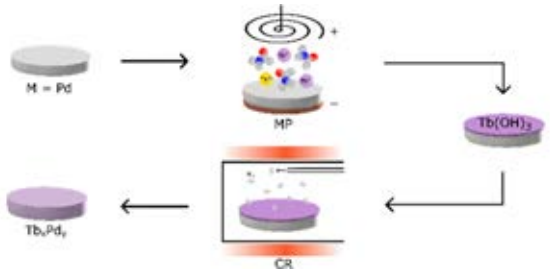

Figure 1: Scheme of Tb-Pd production. First, Tb is molecular plated (MP) as $Tb(OH)_3$ onto a Pd disk. The formation of the Tb_xPd_y IC is then achieved by CR.

First, a Pd disk (25 µm thick) was coated with a molecular compound of Tb via MP [3,5]. Tb was then reduced, via CR, to its elemental state at about T_{max} = 1100 °C, under hydrogen atmosphere, while diffusing into the Pd and forming the new crystalline structure.

Three samples were produced applying different heating times at maximum temperature, namely 5 min, 120 min and 240 min. The α-emitting radionuclide ^{149}Tb (half-life = 4.1 h), produced at the ISOLDE facility at CERN and purified at PSI, was used as tracer to investigate the distribution of Tb in the resulting samples.

The α-spectra of the three samples were measured after MP from the plated side (here referred to as "top") and after CR from both the formerly plated and the opposite side (here referred to as "bottom"). It is important to note that we only gain insight into the first 6 µm of both sides of the sample, which correspond to the range of α-particles from ^{149}Tb (4.08 MeV) in Pd. In order to extrapolate the distribution of Tb, simulations were carried out to best mimic the measured α-spectra. These simulations were performed with the Alpha Spectrum Simulation software (AASI) [6]. The detector parameters in AASI were calibrated with a ^{148}Gd/^{244}Cm (3.27 MeV/5.90 MeV) standard source.

Results and Discussion

The spectra of the three samples were very similar. For this reason, only the spectra relative to the sample heated for 240 min at T_{max}, hereafter Exp_240min, are presented here. The measured and simulated spectra after MP are reported in figure 2. The spectrum was simulated considering a layer with a homogeneous distribution of Tb (black line), present as hydroxide.

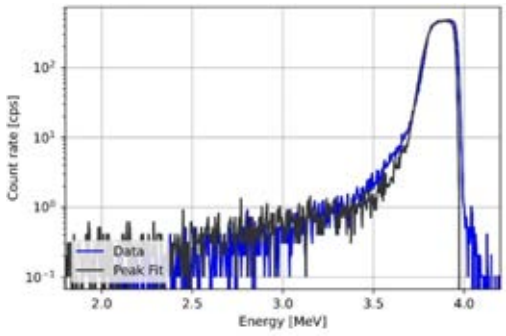

Figure 2: Measured (blue line) and AASI simulation (black line) α-spectrum of the sample Exp_240min after MP.

However, only 94% of the total counts were covered by this simulation. This discrepancy was solved by considering a second and much thinner layer, made of organic compounds, formed during the MP on the top of the main layer. Based on the simulations, the

thickness of the Tb coating after MP was 0.49 µm for Exp_240min. Similar results were obtained for the other two samples. Figures 3 and 4 show the spectra after CR, from the top and the bottom of the sample, respectively. Also in this case, both spectra were simulated considering two distinct layers. The main layer, representing the first 6 µm of the obtained sample, was simulated with an exponential distribution (Low Energy Fit in figure 3). The second layer, corresponding to a thin film formed on both top and bottom of the sample, was simulated with a homogeneous distribution (Gap simulation, in figure 3).

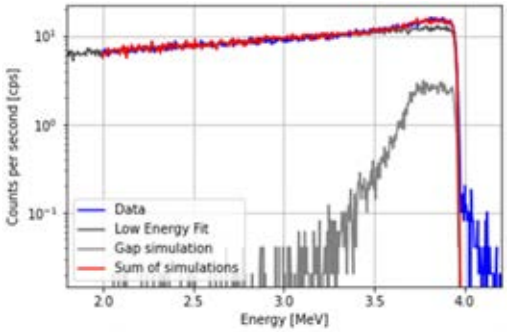

Figure 3: Measured (blue line) and simulated (gray lines) α-spectra of the sample Exp_240min after CR measured from the top. The red line corresponds to the sum of the simulated spectra.

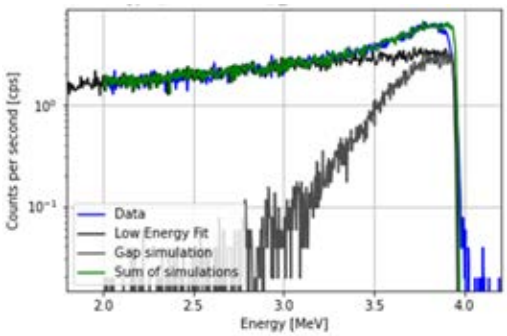

Figure 4: Measured (blue line) and simulated (gray lines) α-spectra of sample Exp_240min after CR measured from the bottom. The green line corresponds to the sum of the simulated spectra.

One important feature of the exponential distribution is the so-called mean penetration depth (MPD). This parameter gives insight into how fast the concentration of Tb decreases in the obtained sample and is defined as the distance from the surface at which the concentration of the Tb atoms in the IC reaches $1/e$ of the concentration on the surface. The evolution of this parameter plotted against the heating time at T_{max} for the three experiments, figure 5, indicates that the distribution of Tb is not completely homogeneous for all the three samples. Figure 6 shows the ratio between the number of Tb atoms in the first µm from the bottom and top of the three samples. This ratio is larger for the sample heated at T_{max} for 120 min, and decreases for the sample that was left in the furnace at T_{max} for 240 min. Indeed, one would expect that this ratio increases with the heating time and approaches the value of 1. One possible reason for the decrease of the ratio for sample Exp_240min, is the poor adherence of the layer molecular plated onto the Pd, proven by scanning electron microscope investigations (not reported here). This probably hindered the contact between Tb and Pd, thus, the formation of an intermetallic compound, leaving the top surface with a relatively higher concentration of "unreacted" Tb.

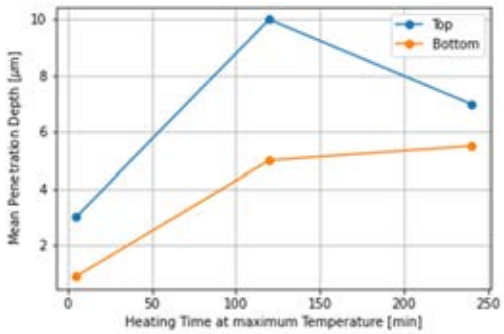

Figure 5: Mean penetration depth as a function of the heating time at T_{max}.

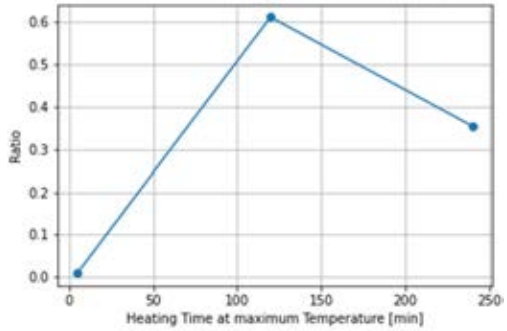

Figure 6: Ratio of Tb in the bottom 1 µm to the Tb in the top 1 µm as a function of the heating time at T_{max}.

In order to be more conclusive about the development of the MPD and the ratio presented above, more experiments must be performed at different heating times. It is also necessary to improve the applied MP method to obtain more reproducible results and to ensure better contact between Tb and Pd.

Acknowledgement

The work is partially funded by EC Horizon 2020 (Grant agreement 847552 — SANDA — NFRP-2018).

References

[1] V.S. Marakatti, et al., Prog. Solid. State Ch , 52, 1 (2018)
[2] Intermetallic Compounds-Principles and Practice Vol. 3: Progress. J. H. Westbrook, R. L. Fleischer (2002)
[3] I. Usoltsev et al., Nucl. Instrum. Meth. A 691, 5 (2012)
[4] N. Cerboni et al. LRC Annual Report 2022, p .42 (2023)
[5] G. De Bodin de Galembert, Master Thesis (2021)
[6] T. Siiskonen, et al., Nucl. Instrum. Methods Phys. Res. 550, 425 (2005)

Evaporation of tellurium from liquid lead-bismuth eutectic studied using the transpiration method

A. Ivan (RATEN-ICN&UPit), J. Neuhausen (PSI), V. Zobnin (PSI&ETHZ), A. Vögele (PSI)

Introduction

Due to their advantageous safety properties (high boiling point, low vapour pressure, high heat capacity, retention of radionuclides, etc.), heavy metals like lead or lead-bismuth eutectic (LBE) are particularly appealing for use as coolants in the development of Gen IV nuclear reactors [1]. One of the most important processes in a lead-cooled fast reactor (LFR) is the behaviour of the hazardous radioactive elements that volatilize from the liquid metal. Such impurities will be formed in the liquid metal by coolant activation or from the fission products in case of an accident. Such processes have an important role in the assessment of the radioactivity released under normal or accidental conditions, and thus in the licensing process of the nuclear facility. Therefore, there is an obvious need to investigate the release behaviour of these radionuclides from the liquid metal.

One of the most problematic radionuclides that are produced in a LFR system is polonium, in particular the ^{210}Po isotope, which due to its high radiotoxicity is difficult to use in experiments. Tellurium is the lighter homologue of Po, which has been often used as a surrogate due to its similar chemical characteristics [2-4]. Thus, having a good understanding of the behaviour of Te may help in studies of polonium chemistry. Another reason for studying the volatility of Te is its production in fuel in a fission reactor.

In this work, the release of Te from a dilute solution in unreduced LBE in an inert gas atmosphere (He) was studied using the transpiration method.

Experimental

The sample used in the experiments was prepared using LBE supplied by the Belgian Nuclear Research Centre in Mol (SCK·CEN) which was mixed with neutron activated Te so that the final sample would have a mole fraction x_{Te} of about $8 \cdot 10^{-3}$ and a specific activity of approx. 100 kBq/g. For activation, elemental tellurium (ca. 10 mg) was sealed into a fused silica ampule that was encapsulated in an aluminium capsule and irradiated for 30 days in the PNA (Preparative Neutron Activation) facility at SINQ. Small pieces of LBE were mixed with the n-irradiated Te in a quartz tube, previously cleaned with a H_2O_2/H_2SO_4 mixture and dried in an oven at 120 °C. The ampule was sealed under a vacuum (≈10^{-4} mbar) and placed in a furnace set at 900 °C for approximately 5 days. In order to reach homogeneity, the ampule was heavily shaken from time to time during heating. After mixing, the ampoule was quenched from 1000 °C to room temperature in a water bath. To determine the initial activity, three small pieces of approximately 0.025 g each and from different spots were cut and dissolved in 4 mL of 7 M HNO_3. γ-ray spectroscopic measurements were performed using a calibrated HPGe-detector. The solutions were measured directly on the detector keeping the same geometry for which the efficiency was determined. The results showed that the homogeneity of the initial sample was not ideal. The average activity of the 3 pieces had a standard deviation of ±20%. This uncertainty of the starting activity makes up for a substantial part of the total uncertainty of the evaluated Henry constant data.

The transpiration method is a well-known method developed for the measurement of the vapour pressure of pure elements or volatile components of multi-phase alloys [5]. At LRC it has been adapted for the determination of the vapour pressure of volatiles in liquid metals. In the transpiration experiments described here, a flow of He is flushed over a metallic LBE-Te sample at a rate assuring a near saturation of the carrier gas with vapours released from the sample heated at a constant temperature throughout the experiments. The vapours are transported away from the sample position by the flowing gas. The amount of Te vapour that condenses in the colder part of the set-up was determined by γ-spectrometry and correlated to the initial activity to determine the Henry constant for the apparent evaporation equilibrium of Te from LBE.

The transpiration experimental set-up consists of a quartz tube in which the evaporation takes place [6]. The tube is placed in a tubular furnace mounted on a movable support so that it can be moved directly to the sample after it has reached the desired temperature. The set-up is located inside an inert gas glovebox. The in- and outlet of the transpiration tube is connected to a gas loop that assures a flow of purified gas over the sample. The dew point was measured with a Mitchell PURA-OEM120 dew point meter and was stable at approx. - 85 °C throughout the experiment series. The temperature range of the experiments performed for the volatilisation of Te was from 220 °C up to 600 °C. Different durations were chosen to ensure measurable amounts of Te are evaporated. After the

experiments, the gas flow is stopped and the furnace is moved away from the sample. The sample was fast-cooled using an air blower to avoid the enrichment of the dissolved species at the sample's surface. Furthermore, two small pieces were cut from the sample for measuring the remaining activity. However, due to the inhomogeneity of the sample after the experiment and the small differences to the starting activity, the activity difference could not be used for calculating the Henry constant. The quartz tube was washed 6 times using basic and acidic solutions for measuring the evaporated activity according to the following washing scheme: 1x4 mL 4 M NaOH, 1x4 mL H_2O, 3x4 mL 7 M HNO_3; 1x4 mL Aqua regia. The activity in each washing fraction was measured using efficiency-calibrated γ-spectrometers and the evaporated activity was calculated as the sum of all the activity measured.

The Henry constant can then be determined from the measured activities using the following equation [7]:

$$K_{H(Te-LBE)} = -\ln\left(1 - \frac{A_{evap}}{A_{before}}\right) \cdot \frac{m_{LBE} \cdot RT}{M_{LBE} \cdot \dot{V}t} \quad (1)$$

where: *Aevap/before* is the activity evaporated from the sample and the initial activity, respectively; *mLBE* – mass of LBE used in the experiments (g); *R* – the universal gas constant (J/molK); *T* – the standard temperature at which the volumetric flow was measured (K); M_{LBE} – molar mass of LBE (g/mol); $\dot{V}$ – carrier gas flow (m^3/s); *t* – experiment duration (s).

Results and discussions

For the evaluation of the volatilisation of Te from molten LBE using the transpiration method five experiments were performed at a temperature from 220 °C up to 600 °C and from 1 hour to 3 weeks, respectively. The results obtained are presented in figure 1 and compared to the relevant literature data. Comparing the Henry constant data to the vapour pressure of pure tellurium it can be stated that there is a rather strong retention of Te in LBE. The results obtained in the present study for the Henry constant of Te in LBE at temperatures between 600 and 400 °C are close to those expected extrapolating the data of [2] to lower temperatures. It can be noticed that at temperatures below 400 °C a deviation from the high temperature behaviour occurs. This behaviour is similar to that observed for polonium in LBE under similar conditions [9]. In order to study this deviance with more precision, more experiments should be performed in the temperature range between 300 °C and 500 °C. For polonium, the deviation towards higher Henry constants at low temperatures was found to be correlated with a surface layer causing enhanced Po evaporation [10].

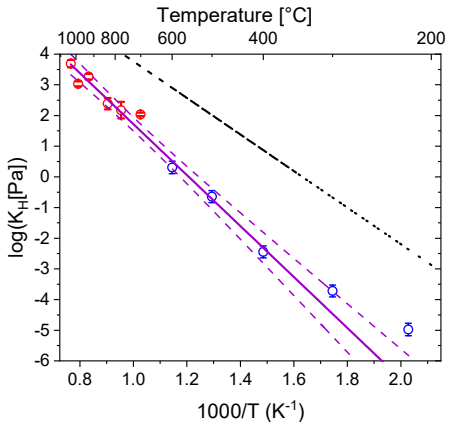

Figure 1. Henry constant of Te evaporated from LBE. Blue circles: this work; Red circles: data from [2] measured at a mole fraction x_{Te} of approx. 10^{-12}; black dashed line: vapor pressure of pure Te [8]; violet lines: linear fit of all data with T ≥ 400 °C (95% confidence interval shown as dashed lines)

Future studies on the LBE-Te system within the PASCAL project will aim at clarifying whether the same mechanism also occurs in this system. Finally, it should be noted that the uncertainties of the Henry constant data obtained in the present study are rather large, in the order of 30 to 40%. This results mainly from the uncertainty in the starting activity, which for the present samples was high because of a rather strong inhomogeneity of the Te-distribution in the LBE samples. A more precise determination of Henry constant data would require the availability of samples with better homogeneity. Thus, efforts on future studies will also be put into developing better preparation methods.

Acknowledgements

This work was funded by the PASCAL project under EURATOM HORIZON2020 Grant Agreement No. 945341. This work was further supported by the IAEA training program TC-ROM9038 fellowship EVT2105664-0001-ROM.

References

[1] IAEA, Liquid Metal Coolants for fast reactors cooled by sodium, lead, and lead-bismuth eutectic, Vienna, Austria: Nuclear Energy Series n° NP-T-1.6 (2012).
[2] J. Neuhausen et al., Radiochim. Acta 92, 917 (2004)
[3] J. Buongiorno et al., Nucl. Technology 147, 406 (2004)
[4] S. Ohno et al., J. Nucl. Science & Tech. 43, 1359 (2006)
[5] C. Alcock et al. Phys. Ch. Proc. Met. Part 1, (1959)
[6] J. Neuhausen, Chimia 74, 976 (2020)
[7] B. Gonzalez et al, J. Nucl. Mat. 450 299 (2014)
[8] L. S. Brooks, J. Am. Chem. Soc. 74, 227 (1952)
[9] M. Rizzi et al., J. Nucl. Mat. 450 304 (2014)
[10] B. Gonzalez et al, J. Rad. Nucl. Chem, 302 195 (2014)

Evaporation of tellurium from liquid lead-bismuth eutectic studied using the thermosublimatography method

V. Zobnin (PSI&UniBern), A. Ivan (RATEN-ICN&UPit), J. Neuhausen (PSI), A. Vögele (PSI), R. Eichler (PSI&UniBern)

Introduction

In this article, the sublimatography approach to study tellurium release from a lead-bismuth eutectic (LBE) melts is described. For a more detailed introduction into metal-cooled IV Gen reactors and study of fission and activation products properties see the report on transpiration experiments on similar samples [1].

The sublimatography method is based on evaporation of melt components with their further condensation in a negative temperature gradient of a chromatographic tube. The key difference of this method from thermochromatography is the macroscopic amount of substance, which forms a multilayer coverage on the column surface. That allows to characterise the sublimation process with macroscopic thermochemical parameters as sublimation enthalpy and entropy (ΔH_{subl} and ΔS_{subl}) and hence to identify the volatile species of tellurium which form in vapors over LBE melts from their deposition temperatures.

Experimental

The experiments on the volatilisation of Te from LBE were conducted in a He (5.0 grade, 99.999%) flow in a gradient tube furnace with a starting furnace where evaporation took place. Helium was additionally purified using a column filled with Sicapent® moisture absorber. A dew point meter (Michell Easydew) was applied to monitor water vapour content. In the experiment with moist helium, the gas flow passed through a gas washing flask filled with water. Sublimation took place in a quartz glass tube (d_{inn} = 5 mm). A charcoal filter was placed at the end of the quartz glass tube to prevent contamination. The temperature gradient along the furnace was measured before the experiments. It ranged from 1000 °C down to room temperature with an almost linear part in a range of 900 – 130 °C (g = -15.2 K/cm).

The LBE-Te sample preparation is described in the aforementioned report [1]. Elemental tellurium of natural isotopic composition (ca. 10 mg) was activated during a 30 days session in the Preparative Neutron Activation facility at SINQ (PSI). The isotope ^{123m}Te ($T_{1/2}$ = 119.2 days) was used as an indicator for γ-spectrometry via 159 keV photopeak.

Two experiments were performed using LBE samples doped with activated Te, one in a dry He atmosphere and one in a moist He atmosphere. The flow rate was 50 mL/min, controlled and regulated by a mass flow controller.

Small chunks of LBE-Te (≈30 mg) were placed in a stainless steel boat and positioned at the entrance of the starting furnace until the temperature in the gradient oven would reach the pre-set value. When the temperature reached 1000 °C the sample was pushed into the middle of the starting furnace and left for 1 hour. After the evaporation period, the sample was rapidly removed from the oven and the gas flow stopped. The sample was then removed from the set-up, dissolved in 7 M nitric acid and the remaining activity was measured by γ-spectrometry.

The quartz column was measured using an HPGe-detector with a 1 cm circular window lead collimator yielding a distribution of the Te-activity over the length of the column.

The deposition temperatures of different species can be calculated using the following equation [2]:

$$T_d = \frac{\Delta H^0_{subl}}{\Delta S^0_{subl} - R \cdot ln \frac{m \cdot RT}{M \cdot \dot{V} t \cdot P_0}} \quad (1)$$

where:

T_d	deposition temperature (K);
ΔH_{subl}	sublimation enthalpy (J/mol);
ΔS_{subl}	sublimation entropy (J/mol·K);
P_0	standard pressure (Pa);
M	mass of the compound (g);
R	the universal gas constant (J/molK);
T	the standard temperature at which the volumetric flow was measured (K);
M	molar mass of the compound (g/mol);
$\dot{V}$	carrier gas flow (m^3/s);
t	experiment duration (s).

Results and discussions

The results of the two experiments studying the evaporation of Te from liquid LBE using the thermosublimatography method are shown in figure 1. The black line represents deposition of Te species in a dry He atmosphere, the blue line is for the deposition profile (left axis) in humid He atmosphere and the red dash line represents temperature gradient along the column (right axis).

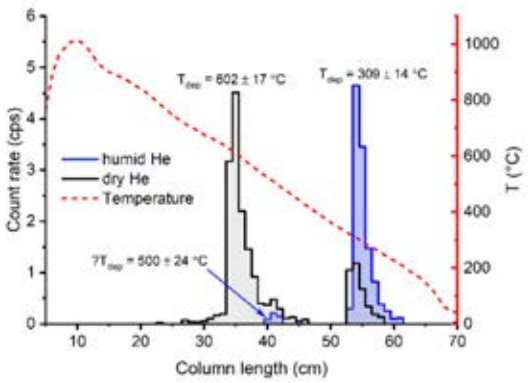

Figure 1: Experimental results of thermosublimatography on LBE doped with irradiated Te

In the dry atmosphere, two peaks are clearly formed at 602 ± 17 °C and 309 ± 14 °C. The peak at 602 ± 17 °C corresponds with the predicted deposition temperature of PbTe (T_{dep} = 592 °C) calculated using equation (1) and thermodynamic data from the Barin handbook [3]. Another Te compound, dioxide (TeO_2), has a close calculated deposition temperature of 612 °C, but since the experiment was conducted in pure He we assume that PbTe is the more probable correlation. This remains to be confirmed by SEM&EDX analysis.

The peak formed at 309 °C could not be associated with any Te compound for which sublimation enthalpy and entropy are known, but since it is the predominant peak in a humid atmosphere it might be some Te oxyhydroxide compound, as suggested in previous thermochromatography experiments on carrier-free amounts of tellurium [4].

Around 500 °C we can assume the presence of a small peak. This peak remains present in humid atmosphere, where it is more clearly visible due to the absence of the PbTe. This peak might indicate the evaporation of a small amount of Te as BiTe, for which the deposition temperature was predicted to be 476 °C.

Since in sublimatography we have macroscopic amounts of substances, further SEM&EDX analysis of the quartz surface from the peak regions would be informative as an additional method of chemical characterisation.

Further experiments to be performed within the PASCAL project - combined with thermodynamic assessments - will aim at clarifying the processes and chemical species underlying the different evaporation mechanisms that occur when Te-containing LBE is exposed to different chemical environments at elevated temperatures.

Acknowledgements

This work was funded by the PASCAL project under EURATOM HORIZON2020 Grant Agreement No. 945341 and additionally supported by the IAEA training program TC-ROM9038 fellowship EVT2105664-0001-ROM.

References

[1] A. Ivan et al. LRC Annual Report 2022, p .48 (2023)
[2] R. Eichler et al., Radiochim. Acta 87 151 (1999)
[3] I. Barin – Thermochemical Data of Pure Substances 3 ed. (1995)
[4] E. Maugeri et al., J. Nucl. Mat. 452 110 (2014)

A thermosublimatography study of volatilization and deposition of refractory metals and their compounds

M. Witschi (PSI&UniBern), J. Neuhausen (PSI), I. Zivadinovic (PSI), A. Ivan (RATEN-ICN&UPit), A. Vögele (PSI), V. Zobnin (PSI&UniBern), R. Eichler (PSI&UniBern)

Introduction

With the increasing demand for energy, the current energy crisis, and the ongoing challenge of high-level nuclear waste management and storage, there is a need for new and innovative reactor designs. Generation IV nuclear reactors are advanced reactor designs currently under development to address these issues. One of the key design features of Generation IV nuclear reactors is the utilization of fast reactors, which are capable of burning off minor actinides present in spent fuel [1]. However, water cannot be used as a primary coolant for these types of reactors as it would moderate the neutrons to thermal energies, which are not suitable for fissioning minor actinides. Alternative coolants such as gases, molten salts, or heavy liquid metals such as lead or lead-bismuth eutectic (LBE) are suggested as coolants for these reactors. The behaviour of fission and spallation products released from LBE samples is of importance in the comprehensive evaluation of the coolant performance characteristics of LBE in future (Generation IV) nuclear reactor systems [2,3]. In the present work, an experimental setup was developed to investigate the evaporation and deposition behaviour of refractory metals formed as fission and spallation products in accelerator driven systems when evaporated from LBE and deposited on quartz column surfaces. The initial thermosublimatographic investigations on rhenium metal samples were conducted to evaluate the functionality of the experimental setup. The outcome of similar studies on Re, Ru and Os dissolved in LBE is expected to provide new insights in their potentially safety-relevant volatilization behaviour and thus support future research endeavours aimed at improving the safety and efficiency of Generation IV nuclear reactors.

Experimental

Thermosublimatography is a technique applied to determine the deposition temperature of volatile species in vapors of a sample substance. The evaporation of macroscopic amounts of a given sample in a column with a negative temperature gradient and its deposition, which forms a multilayer coverage on a column surface, can be used to calculate the thermochemical parameters of sublimation enthalpy (ΔH_{sub}) and entropy (ΔS_{sub}). Conversely, the deposition temperature can be estimated if sublimation enthalpy (ΔH_{sub}) and entropy (ΔS_{sub}) for the volatile species are known. The deposition temperature (T_d) of evaporated species can be calculated by using the following equation:

$$T_d = \frac{-\Delta H^0_{sub}}{R\left(\ln\frac{mRT_0}{v_0 tMP_0}\right) - \Delta S^0_{sub}} \quad (1)$$

where:

T_d	deposition temperature (K)
$_{\Delta}H_{sub}$	sublimation enthalpy (J/mol)
$_{\Delta}S_{sub}$	sublimation entropy (J/mol·K)
P_0	pressure (Pa)
m	mass of evaporated species(g)
R	universal gas constant (J/molK)
T	temperature (K)
M	molar mass of evaporated species (g/mol)
v_0	carrier gas flow (m^3/s)
t	experiment duration (s)

and sublimation enthalpy (ΔH_{sub}) and entropy (ΔS_{sub}) are calculated according to:

$$-\Delta H^0_{sub} = \Delta H_g - \Delta H_s \quad (2)$$

$$-\Delta S^0_{sub} = \Delta S_g - \Delta S_s \quad (3)$$

where:

$_{\Delta}H_g$	enthalpy of compound in gas state (J/mol)
$_{\Delta}H_s$	enthalpy of compound in solid state (J/mol)
$_{\Delta}S_g$	entropy of compound in gas state (J/mol·K)
$_{\Delta}S_s$	entropy of compound in solid state (J/mol·K)

The newly constructed thermosublimatography furnace set-up, shown in figure 1, incorporates a regulated gas flow system for mixing gases, the ability to make ad-hoc changes to gas composition and flow, a Sicapent® moisture absorber through which the gas flows after mixing and before entering the set-up, and an attached vacuum-pump for evacuating the system to remove moisture and trace amounts of unwanted gases (air). To prevent unwanted contamination of the laboratory by eventual species with enhanced volatility, a charcoal filter was installed at the end of the set-up.

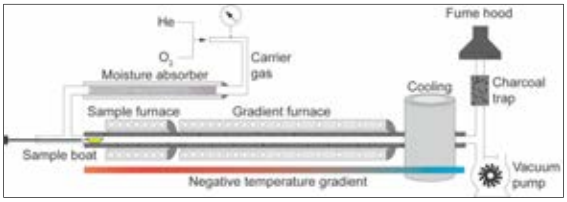

Figure 1: Thermosublimatography setup

First experiments were conducted with rhenium. Samples of rhenium foil, each weighing approx. 20 mg, were irradiated with thermal neutrons in the NAA facility of SINQ at PSI. The sample was placed in a stainless-steel sample boat and inserted into the experimental setup. The setup consisted of two columns, a quartz glass column (1250 mm, $\varnothing_{inside}$5 mm) which was placed inside a INCONEL® column (1250 mm, $\varnothing_{inside}$8 mm). The columns themselves were placed inside two furnaces, a sample furnace set at 1000 °C and a gradient furnace with a temperature gradient starting at 1000 °C and decreasing to ambient temperature. Before the experiment, the boat containing the sample was positioned upstream of the starting furnace. Two experiments were performed, one with pure helium as carrier gas and a second one using 80:20 mixture of helium and oxygen. The flow rate of the mass flow controller was fixed at 50 mL/min and previously calibrated using the gas flow measurement device Defender 530+ by MesaLabs. The experiment started when the correct gas flow was established and the system was flushed and evacuated several times with the respective carrier gas. Once both furnaces reached the intended operational temperature the sample was transferred into the sample furnace using a pushing mechanism. The evaporation process was conducted for 180 min. Subsequently, both furnaces were turned off and the setup cooled down to room temperature. Finally, the sample and the column were removed. The lateral distribution of rhenium activity within the quartz glass column was measured using an HPGe-detector through a 1-cm wide lead collimator yielding a sublimatogram as shown in figure 2 (red line).

Results and discussion

In the experiment using pure helium as carrier gas no transport of rhenium was detected. The results of the evaporation of rhenium in the helium-oxygen mixture using the thermosublimatography method are shown in figure 2. The plot of the activity distribution in the quartz column shows one peak at 86 cm with a corresponding deposition temperature of 130 °C. This indicates that rhenium forms only one compound when exposed to Helium/Oxygen carrier gas at high temperature. The rhenium compound was visible through the quartz column and the colour changed from blue (area with low activity) to black (area with high activity).

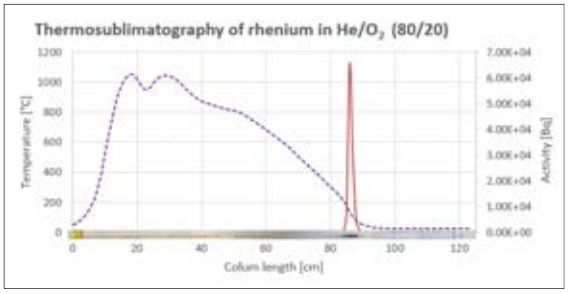

Figure 2: Thermosublimatography of rhenium. For details see text.

The deposition temperature (Td) for several possible rhenium species was calculated according to equation 1 and resulted in the following table of deposition temperatures of rhenium species:

Table 2: Deposition temperature of rhenium oxide species

Species	$_{\Delta}H_{sub}$	$_{\Delta}S_{sub}$	T_d [°C]	m_d [mg]	Ref.
Re	774.9	152.2	3155	9.75	[5]
ReO_2	723.7	251.1	1955	11.43	[4,5]
ReO_3	243.7	207.9	592	12.26	[4]
$HReO_4$	97.1	155.7	150	13.15	[4]
Re_2O_5	-	-	-	11.84	-
Re_2O_7	145.3	244.6	175	12.68	[6]

Although concerning the deposition temperature $HReO_4$ (Td = 150 °C) may be a reasonable fit for the species at 130 °C, it is unlikely that it is the correct molecule due to its yellow color reported in literature [7] and the fact that a dry gas was used in the present experiment. On the other hand, Re_2O_5 is described as a dark-blue substance in [6], which makes it a more likely candidate. A more precise research into the sublimation entalphy and entropy of Re_2O_5 is required to calculate its expected deposition temperature. Furthermore, EDX analytical method could be used to confirm the Re/O ratio and thus to identify the species.

References

[1] M.D. Mathew, Progress in Nuclear Energy 143 (2022).
[2] Aerts et al., Behavior of Spallation, Activation and Fission Products in LBE (2020)
[3] T. Schulenberg, Die vierte Generation der Kernreaktoren, Springer-Verlag GmbH (2020)
[4] R. Eichler et al., Radiochim. Acta 87 151 (1999)
[5] I. Barin, Thermochemical Data of Pure Substances 3 ed., VCH Publishers (1995)
[6] M. Binnewies et al., Thermochemical Data of Elements and Compounds 2nd Edition, WILEY-VCH (2002)
[7] N. Wiberg et al., Holleman Wiberg Lehrbuch der Anorganischen Chemie 102. Auflage, de Gruyter (2007)

Evaporation behavior of cesium and iodine from lead-bismuth eutectic revealed by thermosublimatography

L. Liu (PSI), I. Zivadinovic (PSI&ETHZ), D. P. Herrmann (PSI), A. Vögele (PSI), A. Ivan (RATEN-ICN&UPit), J. Neuhausen (PSI)

Introduction

The release of radionuclides from Lead-Bismuth Eutectic (LBE) is a threat for the safe application of LBE in nuclear installations such as LBE-cooled fast reactors and Accelerator Driven Systems (ADS). It is therefore important to understand the volatilization of radionuclides from LBE and develop efficient capture systems. Recent studies in our laboratories focus on the behavior of cesium and iodine. Indeed, apart from the evaporation of iodine and cesium alone, which has already been accessed in previous works [1], thermodynamic modelling indicates that the formation of CsI in LBE may enhance their evaporation if the solubility limit of CsI in LBE is exceeded [2]. In this context, the present work aims at experimentally investigating the interaction of cesium and iodine in LBE and their evaporation by means of thermosublimatography (TS).

Experimental

Sample preparation

Lead (II) iodide (99.999%, Alfa Aesar), cesium iodide (99.9%, Alfa Aesar) and cesium metal (99.95%, NOVAELEMENTS®) was used as received. LBE (99.999 %, SIDECH) was supplied by SCK•CEN. The oxygen content in LBE was reduced by H_2 gas using a transpiration setup as described in the work on solubility of CsI in LBE [3].

The methodology of sample preparation in these experiments was based on doping LBE homogenously with iodine and cesium containing radioactive tracers. Three types of LBE samples were prepared, including iodine-doped LBE (LBE-I), cesium-doped LBE (LBE-Cs) and cesium&iodine-doped LBE (LBE-Cs&I). For preparing LBE-I, PbI_2 was irradiated with neutrons at the PNA irradiation station at the SINQ facilities for one month to produce ^{126}I tracer. The irradiated PbI_2 was then mixed with LBE in an evacuated quartz ampoule at 550 °C. Finally, the sample was quenched from 475 °C in a water bath. Aliquots of the obtained LBE-I sample were taken and dissolved in 7 M HNO_3. From the activities measured via γ-spectroscopy, iodine was found to be homogenously distributed in LBE. Since the $^{126}I/^{127}I$ ratio is the same in activated PbI_2 and LBE-I, the mole fraction of iodine (x_I) can be deduced from the comparison of the specific activities of ^{126}I in PbI_2 and that in LBE-I. To prepare LBE-Cs samples, cesium metal was first mixed with LBE in an evacuated quartz ampoule at 275 °C for several hours. The mixture was then irradiated at SINQ for 7 h to produce ^{134}Cs tracer, together with a CsI reference. The analysis showed also homogenous distribution of cesium in LBE. The mole fraction x_{Cs} can be calculated by the ratio of the specific activities of ^{134}Cs in irradiated CsI and LBE-Cs. LBE-I or LBE-Cs containing lower dopant concentrations were prepared by diluting the stock sample with additional LBE. The x_I in diluted LBE-I can be precisely predicted knowing the mass of the initial components. In contrary, the x_{Cs} in diluted LBE-Cs is always lower than expected. The loss of cesium is due to its incorporation into the wall of the quartz ampoule.

For preparing the LBE-Cs&I sample, pieces of LBE-I and LBE-Cs samples containing radiotracers were mixed at 410 °C for 3 days in the proper ratio to ensure the presence of equal amounts of I and Cs.

Thermosublimatography

Thermosublimatography (TS) is a method for separating different species in a temperature gradient based on their volatility. The experimental setup is identical to thermochromatography. While in the latter the adsorption of micro-amounts is studied, the former investigates the desublimation of weighable amounts of substances, i.e. a condensed phase is formed. The deposition temperature can be predicted using the following equation knowing the experimental conditions and the mass of the studied species, as described in [4].

$$\ln\frac{m\cdot R\cdot T_0}{v_0\cdot t\cdot M\cdot P_0}=\frac{-\Delta H_{subl}}{R\cdot T_d}+\frac{\Delta S_{subl}}{R} \qquad (1)$$

In this work, the carrier gas was dry He with a flow rate of 45 mL/min, and the exposure time was 5 mins or 3 hours, depending on the experiments.
First studies on pure PbI_2 and CsI indicated that their deposition temperature calculated by equation (1) is in perfect agreement with the experimental results, no matter using quartz tube or stainless-steel tube.

Results and discussion

While the distribution of Cs and I in LBE-Cs and LBE-I is homogenous, in LBE-Cs&I with nominal $x_I \approx x_{Cs} \approx 10^{-3}$ we found a strongly inhomogeneous distribution. The reason for this is most likely the precipitation of CsI from the LBE. As shown in [3], even at 1000 °C the solubility of CsI is lower than the mole fractions of I and Cs in the present sample. The formation of CsI is also

supported by the fact that the ratio of Cs and I is close to 1:1 in all aliquots taken from the LBE-Cs&I sample.

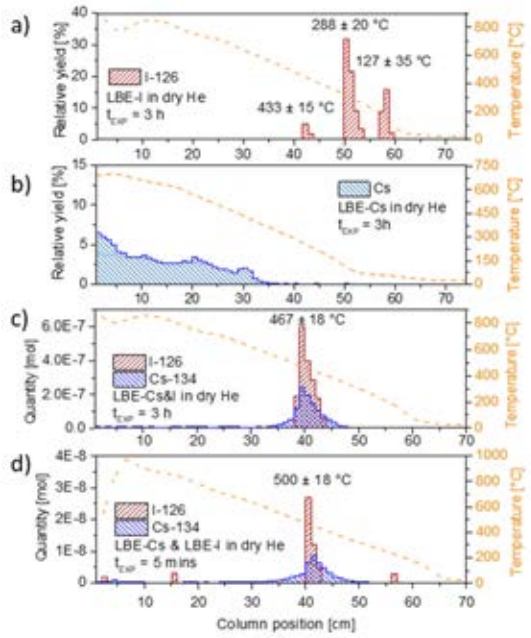

Figure 1: Histograms of iodine and cesium depositions in the tube deduced by activity measurement of the experiments with: a) LBE-I with $x_I \approx 10^{-3}$; b) LBE-Cs with $x_{Cs} \approx 3.10^{-2}$ [5]; c) LBE-Cs&I with average $x_I \approx x_{Cs} \approx 10^{-3}$; d) LBE-Cs & LBE-I with $x_I \approx x_{Cs} \approx 3.10^{-5}$ in the mixture.

Deposition	SEM & EDX	Prediction	Species
T_{dep} = 288 ± 20°C	at%(Pb:I) ≈ 1:2	$T_{dep}(PbI_2)$ = 309°C	PbI_2
T_{dep} = 127 ± 35°C	at%(Bi:I) ≈ 1:3	$T_{dep}(BiI_3)$ = 165°C	BiI_3
T_{dep} = 433 ± 15°C	at%(K:I) ≈ 1:1	T_{dep}(KI) = 461°C	KI?

Figure 2: Characterization of different depositions found in experiments with LBE-I.

A typical distribution of iodine activity is shown in figure 1a. Two major depositions and one minor deposition can be clearly observed, even by visual inspection of the fused silica column. The identification of the species was based on the combination of multiple indications, as shown in figure 2. Taking the deposition at 288±20 °C as an example, the yellow deposition is very similar to the deposition of pure PbI_2. Also, the SEM-EDX analysis indicates this deposition is composed of Pb and I with atomic ratio of about 1:2, supporting this species is PbI_2. Finally, using the mass of PbI_2 deduced by a semi-quantitative analysis of the total amount of iodine in the tube and its distribution as input in equation (1), we find a deposition temperature in good agreement with the experimental result. Therefore, the deposition at 288±20 °C is most likely PbI_2. Similarly, the deposition at 127±35 °C is identified as BiI_3. The minor deposition at 433±15 °C contained I together with K. Thus, it could be KI formed from unknown impurities. Further analysis is required for a safe identification and to find out its origin.
Results on LBE-Cs have already been published in [5]. The characteristic feature of these results was a very broad Cs deposition at high temperature, as shown in Figure 1b. This behavior was explained by the fact that cesium reacts with the column material. Therefore, it does not show the form of a peak.

In the result with LBE-Cs&I (figure 1c), the behavior of Cs and I has totally changed: they now occur in one main deposition at a well-defined temperature of 467 ± 18 °C. This indicates that a reaction has occurred between Cs and I dissolved in LBE. Assuming that the deposited compound is CsI, the calculated deposition temperature is 485 °C, in good agreement with the experiment. The most likely explanation is that CsI was formed from cesium and iodine in LBE during sample preparation and was then evaporated in the TS experiment.

In order to get some clue on the rate of the reaction of Cs and I in LBE, pieces of LBE-Cs and LBE-I with lower concentrations were put together in a sandwich for a TS experiment of only 5 mins. The result is shown in figure 1d. We can observe the same behavior of Cs and I as in figure 1c. The calculated deposition temperature for CsI is 509 °C, again in good agreement with the experimental result. This indicates that even at lower concentrations CsI is formed rapidly in LBE.

In conclusion, combining TS and other characterization techniques such as SEM&EDX, we identified 1) the major species evaporated from LBE-I to be PbI_2 and BiI_3; 2) the formation and evaporation of CsI by mixing Cs and I together in LBE, with a relative fast kinetics. Further investigations of the reaction kinetics should be carried out in the operation temperature range of the metal cooled reactors (about 400 °C). However, with lower temperature less substance will be evaporated, resulting in difficulties for the detection and identification.

Acknowledgements

This work was funded by the PASCAL project under EURATOM HORIZON2020 Grant Agreement No. 945341.

References

[1] I. I. Danilov et al., LRC Annual Report 2017 18 (2018)
[2] A. Aerts, SCK·CEN, private communication
[3] L. Liu et al. LRC Annual Report 2022, p .56 (2023)
[4] R. Eichler et al., Radiochim. Acta 87 151 (1999)
[5] E. Karlsson, PhD thesis, Univ. Bern (2020)

Solubility of cesium iodide in lead-bismuth eutectic at different temperatures

L. Liu (PSI), I. Zivadinovic (PSI&ETHZ), D. P. Herrmann (PSI), A. Vögele (PSI), A. Ivan (RATEN-ICN&UPit), A. Aerts (SCK CEN), J. Neuhausen (PSI)

Introduction

Understanding the release of radionuclides from heavy liquid metals (HLM) is essential for the safe application of HLM-cooled generation IV nuclear reactors and accelerator-driven systems. In the framework of the PASCAL project, the behavior of Cs and I in HLM is being investigated [1]. Previously, experiments have been performed on the solubility of CsI in LBE, Bi, and Pb metals without any pre-treatment. The results show that the dissolved amount of Cs is very different from that of I, presumably because insoluble Cs(Pb,Bi)-oxides form with the oxygen dissolved in metals [2]. In order to better understand the behavior of Cs and I inside, the present work investigates the solubility of CsI in LBE with reduced oxygen content.

Experimental

Cesium iodide (99.9%, Alfa Aesar) was used as received. LBE (99.999%, SIDECH) represents the material to be used in the MYRRHA project [3]. To reduce the amount of dissolved oxygen in the LBE sample, small pieces of LBE were placed in a transpiration setup [4] under circulation of H_2 gas. The sample was melted and reduced by H_2 successively at 450 °C, 330 °C and 200 °C, respectively. The duration for each temperature step was at least 6 hours. Afterwards, the melt was cooled down slowly to room temperature in the H_2 atmosphere. The surface layer of the obtained LBE piece was removed in order to remove residual metal oxide spots remaining on the surface.

To dissolve CsI in LBE, a protocol similar to that described in [2] was used. Briefly, reduced LBE and CsI salt with a mass ratio of roughly 1:100 was put into a clean quartz ampoule under Ar atmosphere. The ampoule was then evacuated to $P<10^{-4}$ mbar and sealed by a torch. Three ampoules were prepared and placed in a furnace set to 1000 °C, 1100 °C and 1200 °C, respectively. The heating lasted for 24 hours and the ampoules were shaken violently several times in order to well mix CsI and LBE during this period. Finally, the ampoules were quenched to room temperature by putting them into a water bath within a few seconds after their removal from the furnace.

The samples were examined by Scanning Electron Microscopy (SEM) and Energy-Dispersive X-ray (EDX) analysis to identify the present phases. The bulk metal phase was probed by core-drilling. The wire-like LBE samples were then activated by thermal neutrons at the SINQ facility at PSI, together with a pure cesium iodide reference sample. Two irradiations were performed; the first one with a duration of 300 s in order to produce ^{128}I, while the second irradiation lasted 10000 seconds to produce measurable amounts of ^{134}Cs. The activities of ^{128}I and ^{134}Cs in the LBE-samples as well as in the CsI reference sample were measured using a calibrated γ-spectrometer.

GEM calculations

For interpretation of the experimental results, Gibbs Energy Minimization (GEM) calculations were performed using the GEM module of HSC Chemistry® version 9.8.1.2 [5]. A system containing solid, liquid and gas phases was set up. The solid and gas phases comprised all solid- and gas- phase compounds of the studied elements (Bi, Pb, Cs, I, O, Ar) incorporated in the database of HSC Chemistry®. The solid compounds were treated as individual pure phases, while the gas phase was considered an ideal mixture. The liquid phase comprised the elements Bi, Pb, Cs, I and O. It was modelled as an ideal dilute solution of cesium, iodine and oxygen in lead and bismuth at the eutectic composition, with thermodynamic activity coefficients derived from phase diagrams and experiments [6,7]. The initial compositions of the calculated systems contained Bi, Pb, Cs and I in a molar ratio of 0.55:0.45:0.005:0.005, and a small amount of residual Ar. Calculations were performed for a constant volume corresponding to that of the used ampoules for a temperature range between 200 °C and 1250 °C. The oxygen content of the system was varied over a wide range between 1 and 10^4 atom ppm.

Results and discussion

SEM and EDX studies showed the coexistence of CsI and LBE phases in the samples, a mandatory requirement for studying the phase equilibrium. We assume that the bulk metal phase was saturated with dissolved CsI at the nominal temperature of each experiment.

The ratio of stable and radioactive cesium resp. iodine in the metal samples should be the same as that in the reference CsI sample because they received the same neutron fluence. Thus, the mole fraction of I (x_I) and Cs (x_{Cs}) in the metal samples can be deduced from activity measurements as described in [2].

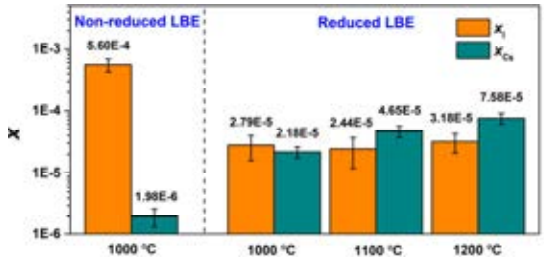

Figure 1: Mole fractions of I and Cs in reduced LBE-CsI and non-reduced LBE-CsI mixture prepared at different temperatures. Uncertainties correspond to 2σ.

Figure 1 shows the mole fractions of I and Cs in reduced LBE samples at different temperatures, together with results from a non-reduced LBE sample at 1000 °C. Compared to non-reduced LBE, it is obvious that Cs and I are uniformly dissolved in reduced LBE, confirming the influence of oxygen in LBE on the dissolution of CsI. For the reduced LBE samples, the mole fractions of Cs and I in LBE are in the order of 10^{-5} and show only a small increase with increasing temperature.

Figure 2 shows the amounts of the main species forming the condensed phases calculated by GEM for CsI mixed with O-free LBE and with LBE containing 1000 at-ppm O. The main component in the gas phase apart from Ar is a small amount of CsI(g). In the O-free system, we find a liquid metal phase (denoted as lbe) containing mainly the metals Pb and Bi in the eutectic ratio in equilibrium with a liquid salt phase containing CsI(l). The ratio of the amounts of these main components remains almost constant at the input ratio of 1:100 over the full temperature range. Apart from the main constituents, there are small and equal amounts of iodine and cesium dissolved in the liquid metal, denoted as I(lbe) and Cs(lbe). Converting the measured mole fractions to molar amounts (shown as symbols in the figure) we see that our solution model describes the behaviour observed in the experiments reasonably well. The calculated solubilities are in the same order of magnitude as the experimental results. However, the calculations predict a stronger temperature dependency. For the O-containing system a precipitation of solid $CsBiO_2$ is predicted by the calculations. Therefore, less Cs remains in the liquid metal. At the same time, the amount of iodine in the liquid metal is increased. This reflects the observations in the experiments made with non-reduced LBE. Summarizing we can state that our thermodynamic modelling is in good agreement with the experimental results. However, there are many factors both on the experimental and the calculation side that are not yet known with sufficient accuracy to consider the presented results and method as a means for precisely determining thermodynamic properties of solutes in liquid metals. Among these not well-known factors are: 1) reliable measurement of the actual O-content in the system; 2) experimental proof of the formed CsPbBiO-phases in equilibrium with the liquids; 3) proof of efficient quenching to capture the solubilities at the nominal temperatures. Finally, the temperature dependant thermodynamic activity coefficient data used for I(lbe) and Cs(lbe) in the calculations are derived from few and potentially not very reliable data. In conclusion, the presented results are rather a proof of principle than a precise determination of CsI solubility in LBE. Nevertheless, if the above-mentioned problems are overcome, experiments such as described here could prove a proper method for obtaining valuable data on the thermodynamic properties of solutes in liquid metals, complementary to other methods such as vapour pressure measurements.

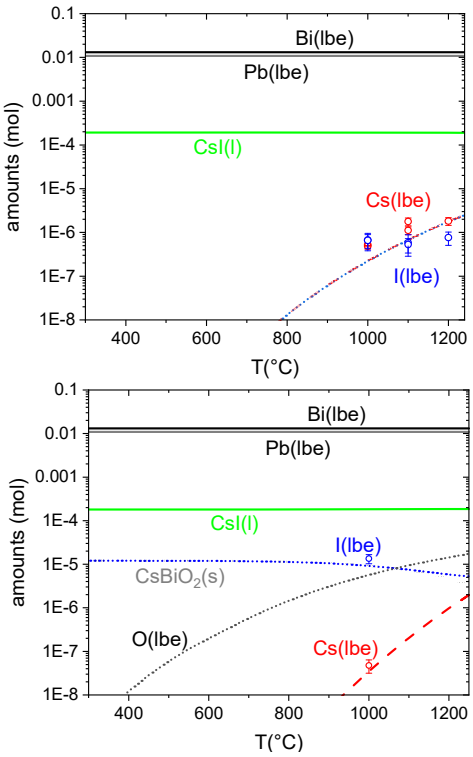

Figure 2: Calculated amounts of different species present in (a) oxygen-free LBE-CsI mixture and (b) LBE-CsI mixture containing 1000 ppm O at different temperatures

Acknowledgements

This work was funded by the PASCAL project under EURATOM HORIZON2020 Grant Agreement No. 945341.

References

[1] https://www.pascal-project.eu/
[2] L. Liu et al., LRC Annual Report 2021, 24 (2022)
[3] https://myrrha.be/
[4] I. I. Danilov et al., LRC Annual Report 2017, 18 (2018)
[5] A Roine HSC Chemistry® [Software], Outotec, Pori, Finland. Software available at www.outotec.com/HSC
[6] L. F. Yamshchikov et al., Rasplavy 2 34 (2001)
[7] I. G. Gvertdtsiteli et al., Russ. J. Phys. Chem. 58 1189 (1984)

Measuring Po in a matrix with a high β-background

I. Zivadinovic (PSI&ETHZ), R. Dressler (PSI), J. Neuhausen (PSI), M. Veicht (PSI&EPFL), P. Steinegger (PSI&ETHZ)

Introduction

Understanding the thermal release behavior of various safety-relevant radionuclides from liquid lead-bismuth eutectic (LBE) is of crucial importance for the licensing of accelerator driven systems (ADS) like the MYRRHA reactor. For the latter, LBE is foreseen as the coolant. From the radioelements in question, the element polonium is of particular importance due to its high radiotoxicity, potential volatility and its high production rate within the coolant [1]. Therefore, furthering the understanding of its evaporation behavior as well as its chemistry in LBE is supported within the framework of the Horizon2020 project PATRICIA.

Detailed investigations of the volatilization of polonium from LBE have already been reported by Gonzalez et al. [2], Ohno et al. [3] as well as others. The common shortcoming of all those studies concerns the fact that Po was evaporated from pure LBE in the absence of other radionuclide impurities. Hence, earlier experiments do not accurately address the complex chemical environment of the LBE coolant within an operating ADS, where a plethora of different radioisotopes is co-produced via various nuclear reactions. All of these trace impurities can potentially chemically interact with Po and may alter its release behavior. As such, a reference material is needed that can mimic and approximate this chemical environment in order to reinvestigate the release behavior of Po from LBE under more realistic conditions. The ITC group at PSI has access to such LBE material, originating from the demonstrator MEGAPIE (**Mega**watt **Pi**lot **E**xperiment) [4], which features the aimed diverse inventory of different, long-lived radionuclides.

Since Po is a pure α-emitter, a common and fast approach to measure its radioactivity within liquid solutions would be liquid scintillation counting (LSC). However, since the MEGAPIE samples contain a large number of β-emitting radionuclides, measuring the underlying Po activity becomes challenging. Here, we investigated whether we can selectively measure the Po activity within MEGAPIE samples in the presence of its high β-background. To do so, a pulse shape analysis (PSA) was employed in order to disentangle the α- and β-activities of dissolved MEGAPIE cuttings based on the different pulse shapes of signals from α- and β-decay. This approach leverages the fact that ^{208,209}Po are the sole α-emitters within those samples.

Experimental

The α- and β-activities of different solutions were measured with LSC by mixing them with the Ultima Gold™ AB LSC-cocktail (PerkinElmer) and employing the PSA as above-mentioned. In preparation of an LSC measurement, the following steps were generally carried out. First, aliquots of the different solutions (see below) were diluted to obtain a concentration of 0.1 M HNO_3. These aliquots were then mixed with 15 mL of the LSC cocktail and filled into a 20 mL plastic LSC vial. The vials were capped off, vigorously mixed and then measured. All measurements were done in triplicate.

The PSA was calibrated with pure in-house prepared α- and β^--standards. ^{210}Po was used as the α-source, while the ^{32}Si/^{32}P-pair was used as the β^--source. For this calibration, 1 kBq of each standard was measured to determine the different spillover values at various PSA discriminator settings. These measurements resulted in an optimum discriminator setting, which was then used for all further measurements.

To measure the associated uncertainty, a mixture containing around 1 kBq of ^{32}Si and 1 kBq of ^{210}Po was measured using the PSA three times.

In the last step, a MEGAPIE solution was analyzed, which was obtained by dissolving a small cutting (≈ 56 mg) of MEGAPIE LBE in 7 M HNO_3. Two samples were analyzed; the first contained only the MEGAPIE solution, whereas the second sample contained ≈ 1 kBq of the ^{210}Po standard in addition to the MEGAPIE solution for the uncertainty determination. The difference in Po activity between the spiked and unspiked samples were compared with the added Po amount.

Results and discussion

The LSC-spectrum of the sample containing the mixture of the α- and β^--standards is represented in figure 1. Visually, a clear separation of the two radionuclides is apparent, given their distinct peak shapes. All of the added activity could be fully accounted for. The calculated activities from the spectra deviated only by 0.3% from the individually measured activities.

The LSC-spectrum of the unspiked MEGAPIE sample is shown in figure 2. The resulting spectrum is more complex due to the different, long-lived radionuclides still present within the MEGAPIE sample. Nevertheless, the Po activity could be successfully disentangled from the comparably high β-background. The α-peak

appears at the same position as the Po peak in the previous graph (i.e. ^{210}Po standard), indicating that it is indeed Po.

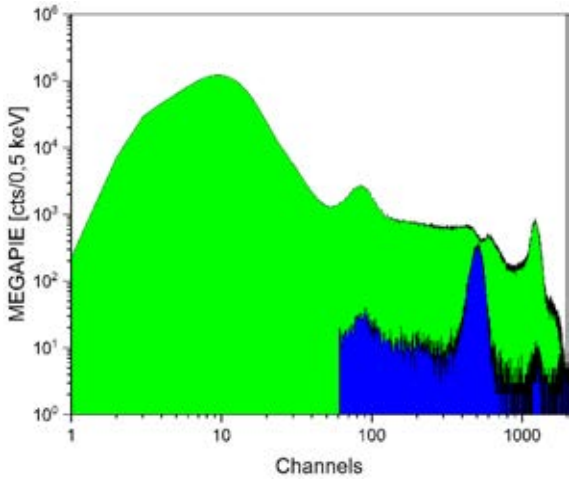

Figure 1: LSC-PSA spectrum of the ^{32}Si/^{32}P/^{210}Po mixture. The α-spectrum is represented in blue, while the β-spectrum is represented in green.

The associated uncertainty of the analysis of the α-activity in MEGAPIE samples was determined to be 3.3%, making this method acceptable to be used for our analysis purposes. The slightly increased uncertainty, in comparison to the standard measurements has multiple reasons. Generally, the PSA performs best if the measured sample resembles the used calibration sources. However, the Po activity in the MEGAPIE samples is lower by about one order of magnitude. Furthermore, the ratio between the α- and β-activity is not 1:1, which has been shown to affect the efficiency of the PSA. Lastly, our sample contains a sizable amount of high-energy β-emitters. This type of radiation can produce a higher amount of triplet states in the cocktail, which take longer to de-excite and thus are more likely to be misidentified as α-activity by the PSA.

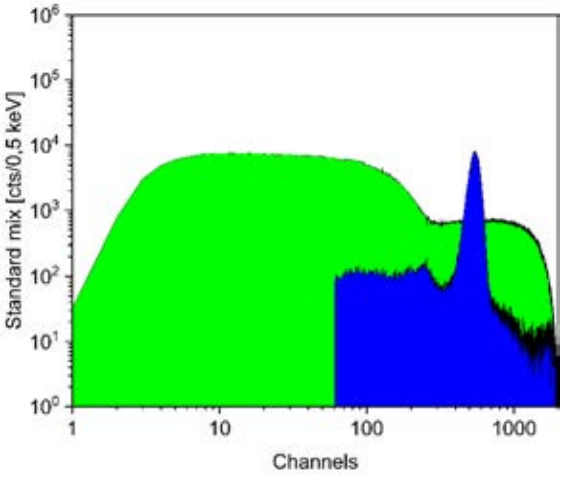

Figure 2: LSC-PSA spectrum of the MEGAPIE sample. The α-spectrum is represented in blue, while the β-spectrum is represented in green.

Acknowledgements

This work was funded by the PATRICIA project under EURATOM HORIZON2020 Grant Agreement No. 945077.

References

[1] A. Aerts er al., Nucl. Mater. Energy 5 735-765 (2020)
[2] B. Gonzalez et al., J. Nucl. Mater. 450 299–303 (2014)
[3] S. Ohno et al. J Nucl Sci Technol. 43:11, 1359-1369 (2006)
[4] C. Fazio et al. Nucl. Eng. Des. 238 1471–1495 (2008)

Is the half-life of ^{42}Ar correct?

D. Schumann (PSI), E. Maugeri (PSI), Y. Dai (PSI), R. Dressler (PSI), U. Köster (ILL)

Introduction

Early estimations of the half-life of ^{42}Ar are reported by *S. Katcoff* [1] in 1952 as a lower limit of 3.5 y and ≈30 y by *R.W. Stoenner* et al. in 1960 [2]. The currently adopted value is (32.9±1.1) y [3], which is based on one measurement by the same authors [4], performed in 1965. In this work, the half-lives of ^{37}Ar, ^{39}Ar and ^{42}Ar were determined simultaneously using mass spectrometry for the determination of the numbers of atoms as well as β– and γ-ray spectrometry for the determination of the activity. The half-life of ^{37}Ar ($t_{1/2}$ = (35.14 ± 0.05) d [4]) was determined following the decay, whereas for ^{39}Ar and ^{42}Ar the direct method was applied in relation to the ^{37}Ar half-life. The advantage of the approach was, for the latter two, that only isotope and activity ratios needed to be determined and no absolute measurements were necessary. Note, that – in contrary to the uncertainty of 3% given in [3] - the authors additionally consider possible systematic errors in the mass spectrometry, in sample transfer and in measurements of counter efficiency, finally leading to an estimated uncertainty of 6%. Because of the astrophysical importance of the isotope and due to the fact that there is only one experimental determination so far, a re-measurement of the half-life of ^{42}Ar is highly desirable [5].

Experimental approach

Figure 1: Photos of six samples (1-4: Ti; 5&6: Cu) before irradiation in the SINQ at PSI in the frame of the STIP IV material investigation program. Sample No. 4 was used for the half-life determination of ^{42}Ar

One of the possibilities for producing ^{42}Ar is spallation induced by high-energetic protons or neutrons on elements heavier than potassium, for instance Ti or V. For the current measurement, we have a Ti sample available, which had been irradiated for two years in the target of the SINQ facility at PSI (end of beam December 2005) in the frame of the STIP IV program [6]. In figure 1, a photo of several specimen irradiated in STIP IV is shown. Our sample is No. 4. The first γ-ray spectrometry of this sample was performed on 16.3.2010 with a HPGe detector. Besides the ^{42}Ar of interest, which can be easily detected using the γ-line of its short-lived daughter ^{42}K (1525 keV), also ^{22}Na, ^{54}Mn, $^{57/60}$Co and, in particular, ^{44}Ti via its short-lived decay product ^{44}Sc were identified as the main reaction products.

A second measurement of this sample using a different HPGe detector was performed on 9.12.2022. In figure 2, the γ-ray spectrum is shown. The GENIE2000 software program was used in both cases for the data acquisition and analysis.

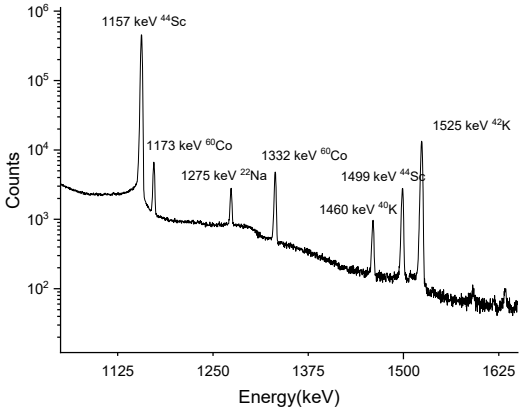

Figure 2: Part of the γ-ray spectrum of sample No. 4, showing the relevant energy region. Measured at 9.12.2022.

The 1157 keV γ-ray line of the ^{44}Ti daughter ^{44}Sc was used as internal standard for the half-life determination of ^{42}Ar. This approach allows the determination with minimum impact of the efficiency calibrations by directly using the peak area ratios of the two corresponding γ-lines. Since the half-life of ^{44}Ti is precisely known, the uncertainty budget is then dominated by the counting statistics only.

Results, discussion and outlook

In table 1, the peak areas of the ^{44}Sc γ-line at 1157 keV and the ^{42}K γ-line at 1525 keV are summarized for the two measurements in 2010 and 2022. Based on the adopted values for the half-lives of ^{44}Ti (59.1±0.3) y [7] and ^{42}Ar (32.9±2.0) y [4], the expected peak areas on 9.12.2022 are calculated and shown in column 3. The ratios ^{44}Ti (1157 keV) / ^{42}Ar (1525 keV) are also given table 1.

Table 1: Peak areas of the 1157 and 1525 keV γ-ray lines of sample No. 4, measured on 16.3.2010 and 9.12.2022, respectively, as well as their respective measured and expected ratios.

Isotope/γ-line	^{44}Ti 1157 keV	^{42}Ar 1525 keV
Peak area 16.3.2010	607733 ±818	22881 ±161
Expected peak area 9.12.2022	523630 ±809	17527 ±307
Measured peak area 9.12.2022	6731000 ±4990	225400 ±946
Ratio peak area ^{44}Ti/^{42}Ar measured at 16.3.2010	26.56 ±0.19	
Ratio peak area ^{44}Ti/^{42}Ar expected at 9.12.2022	29.92 ±0.53	
Ratio peak area ^{44}Ti/^{42}Ar measured at 9.12.2022	29.86 ±0.13	

The uncertainty budget is as follows:

counting statistics 1157 keV	
16.3.2010	0.13%
9.12.2022	0.07%
counting statistics 1525 keV	
16.3.2010	0.70%
9.12.2022	0.42%
estimation of the low-tail uncertainty	3.0%
half-life ^{42}Ar	6%
overall for expected ratio	1.8%

However, the present determination suffers from some shortcomings. After end of beam in 2005, the entire SINQ target had been stored for cooling till 2010. Then, it was opened and the samples from the STIP IV program were removed from the target assembly. A γ-ray measurement was performed with sample No. 4 to get an overview on the produced activity of the samples 1-6 shown in figure 1. The peak shapes of the relevant peaks in this spectrum are not ideal, but show low-energy tailing that increases the uncertainties in the area determination.

The six samples were then stored together in an aluminium box in the dry storage of the Hotlab at PSI till December 2022. The appearance of ^{60}Co and ^{54}Mn could be caused by a cross contamination due to the storage together with the Cu samples. Moreover, a different detector has been used for the measurement in December 2022, which could course slight differences in the energy dependence of the photon efficiency.
The main problem, however, is that with this type of storage – the samples had not been individually sealed in air tight vessels - it cannot be ruled out that part of the Ar has outgassed during the storage period.

We now sealed the sample in a quartz ampoule (figure 3) and will repeat the measurement during the next 10 years. The data analysis and evaluation should then also include the peak area ratios obtained using the areas of the ^{22}Na and ^{60}Co γ-ray peaks.

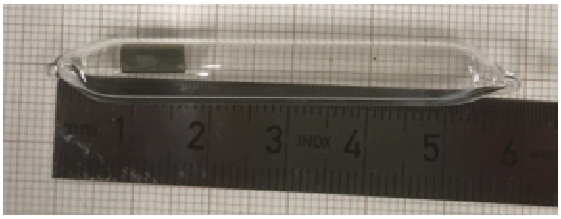

Figure 3: Photo of sample No. 4 (irradiated Ti), sealed in a quartz ampoule.

References

[1] S. Katcoff, Phys.Rev 87, 886 (1952)
[2] R.W. Stoenner, O.A. Schaeffer, R. Davis, Jr., J. Geophys. Res. 65, 3025 (1960)
[3] J. Chen, B. Singh, Nuclear Data Sheets for A=42, Nuclear Data Sheets 135 1–192(2016)
[4] R.W. Stoenner, O.A. Schaeffer, S. Katloff, Science 148 1325(1965)
[5] St. Heinitz, I. Kajan, D. Schumann, Radiochim. Acta 110(6–9): 589–608 (2022)
[6] Y. Dai et.al., Journal of Nuclear Materials 431 (2012) 2–9
[7] Jun Chen Balraj Singh, J.A. Cameron, G. Plancque, Nuclear Data Sheets for A = 44, Nuclear Data Sheets 112 2357 (2011)

Performance of SnO_2-based chemosensors after irradiation with γ–rays and α-particles – Part 1: CO sensing

N.M. Chiera (PSI), M. Kasprzak (PSI) P. Steinegger (PSI&ETHZ), G. Zonta (UNIFE), M. Astolfi (UNIFE), C. Malagù (UNIFE)

Introduction

In many radiochemical studies, a tightly controlled composition of the carrier gas is fundamental, either to target the synthesis of specific chemical species, or to predict the chemical behaviour of the studied elements in a given gas phase. In general, atmospheric mass-spectrometers (MS) are employed for such scope. However, MS show several shortcomings, e.g. impractical transport, high maintenance costs, and the inability to identify polyatomic or molecular interferences having the same charge-to-mass ratio. Hence, alternative detection techniques are highly desired. During the past decades, chemoresistive gas-sensors, based on semiconductor nanostructures, have received increasing attention due to their high sensitivity to a wide range of volatile compounds, their low production cost, fast response, and stability.

Here, two types of SnO_2-based materials were selected and their sensing performance before and after α- and γ-irradiation was tested. Chemoresistive SnO_2(Au), i.e. SnO_2 decorated with gold nanoparticles, and STN, i.e. an oxide mixture $(Sn,Ti,Nb)_xO_y$, sensors were prepared at the University of Ferrara (UNIFE, Italy). Irradiation of the sensors with moderate doses of α-particles and γ-rays was performed at PSI. The sensing properties of both materials towards CO, a strong reducing agent generally employed for sensors calibration, were evaluated by employing an open-ended gas-flow setup at the Sensing Laboratory (SL) of UNIFE. The performance of the SnO_2(Au) and STN sensors before and after irradiation is discussed.

Experimental

Eight n-type SnO_2-based semiconductor sensors were prepared in the clean rooms of the Department of Physics and Earth Sciences of UNIFE. Both SnO_2(Au) and STN sensing materials were synthesized applying the sol-gel technique [1]. Before irradiation, all eight sensors were simultaneously inserted in the hermetically sealed chamber in the stationary gas-sensing device described in [2]. First, the sensors were stabilized under a synthetic dry airflow (80% N_2 and 20% O_2, 500 sccm), and the steady-state sensor voltage V_{air} for each sensor was recorded at a working temperature of 400 °C. After the baseline acquisition, the gas flow was switched to 500 sccm of dry air containing 200 ppm of CO (99.99% purity). The gas was introduced in the chamber until each sensor reached saturation, i.e. there was no further change of the steady-state sensor voltage V_{gas} measured upon contact with the carrier gas containing CO. Successively, the gas was switched back to pure dry air, allowing the sensors to return to their baseline. The sensor response (R) was calculated as:

$$R = V_{gas} / V_{air} \quad (1)$$

The same process was repeated three times, in order to verify the signal stability and repeatability. The average response <R> for each sensor was calculated by averaging the R values from the three separate measurements. Subsequently, the sensors were irradiated with α-particles and γ-rays as follows. Two sensors (one per type of sensing material) were irradiated with α-particles at the Laboratory of Radiochemistry of PSI. For this, a ^{241}Am (half-life $t_{1/2}$ = 432.6 y, $E_{\alpha1}$ = 5485 keV (84%), $E_{\alpha2}$ = 5442 keV (13%)) certified point source (Al-6886 Eckert & Ziegler source, activity = 15.06 kBq on 05/23/2022, radius of radioactive source = 4 mm) was used. Each irradiation took place over the duration of 48 h, at a source-to-sensor distance of 3 mm at normal laboratory conditions. Each sensing film was irradiated with a particle fluence of $5.5 \cdot 10^8$ α particles/cm^2. Four sensors (two per type of sensing material) were irradiated with γ-rays using a sealed ^{137}Cs ($t_{1/2}$ = 30.09 y, Eγ = 662 keV) 4π source (0002GS The Radiochemical Center Ltd. source, activity = 2.9 GBq on 05/23/2022) at the Calibration Laboratory of PSI. The sensors were placed at a distance of 18 cm from the radioactive source, together with an electronic dosimeter (DMC 3000TM, Mirion Technologies, Inc.). The latter quantified a total γ-dose of 0.18 Sv after 22 h of irradiation. The photon fluence was estimated as $4.75 \cdot 10^{10}$ photons/cm^2. Two sensors (one per type of sensing material) were not subjected to any irradiation and therefore were employed as non-irradiated controls. Successively, CO-sensing tests were performed at the identical experimental conditions as applied before irradiation.

Results and Discussion

The responses <R> of each SnO_2(Au)- and STN-based sensor in the CO-sensing experiments before and after irradiation are shown in figures 1 and 2, respectively. By comparing the averaged responses of both control sensors towards CO, it emerges that the STN material shows a higher sensitivity to the target gas. This is in agreement with the observations made earlier [3],

where the STN responses to different volatile organic compounds were higher by a factor of ≈1.3 in comparison to SnO_2(Au).

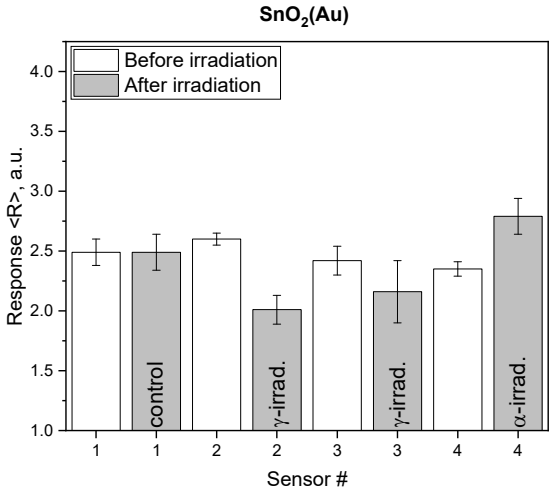

Figure 1: Average SnO_2(Au) -based sensor responses <R> to a dry airflow containing 200 ppm of CO before (white bars) and after (grey bars) irradiation; the irradiation type to which each sensor was subjected is indicated in individual bars.

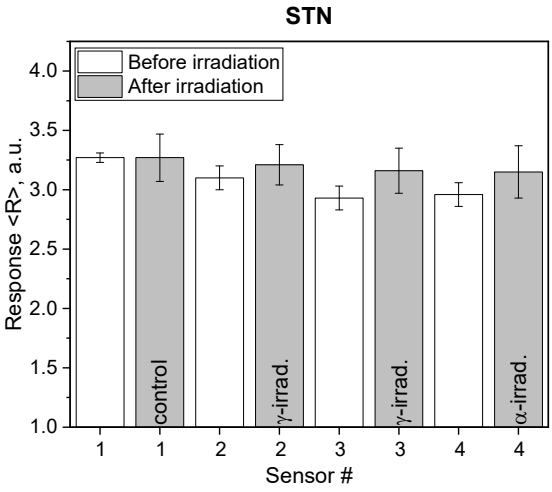

Figure 2: Average STN-based sensor responses <R> to a dry airflow containing 200 ppm of CO before (white bars) and after (grey bars) irradiation; the irradiation type to which each sensor was subjected is indicated in individual bars.

An increased response of the α-irradiated SnO_2(Au) sensor towards CO is observed. This is in line with previous works [4, 5], where it was shown that the exposure of SnO_2 films to moderate doses (i.e., a particle fluence below 10^{13}) of protons or heavy-ions enhanced the gas-sensing performance towards reducing gases (e.g., SO_2, CO), due to the creation of oxygen vacancies by particle irradiation. For the α-irradiated STN-based sensor, the increase in response to CO is statistically not significant. This can be explained by the higher dissociation energies for the Nb-O (726.5 kJ/mol) and Ti-O (666.5 kJ/mol) bonds, in comparison to the Sn-O ones (528 kJ/mol) [6], which might result in overall less oxygen vacancies. In case of photons, the moderate γ-irradiation of the SnO_2(Au) and STN materials produce more homogenously distributed changes in the bulk of the sensors in comparison to an α-irradiation. Thus, such γ-induced changes may affect predominantly the electrical characteristics of the sensors, instead of creating oxygen vacancies. Whereas this not significantly affects the sensing properties of the STN material, an apparent trend of a lower response to CO for the SnO_2(Au) one is observed. This is in agreement with the slight decrease of the gas-sensing response towards CO in SnO_2-based sensors after an exposure to a γ-dose below 50 Gy [7]. These first results point to the feasibility of using these materials in radiochemical environments with low radiation doses. First observations lead to the possibility of exploiting different types of irradiation (i.e., α-particles or γ-rays) to selectively increase the sensitivity of each material towards specific gas components. In order to corroborate this hypothesis, further systematic studies with higher radiation doses are envisaged.

References

[1] M.L. Traversa et al., J. Sol-Gel Sci. Technol. 22, 12 (2001)
[2] G. Zonta et al., Sens. Actuators B 218, 6 (2015)
[3] M. Astolfi et al., Molecules 26, 12 (2021)
[4] P. Tyagi et al., Nucl. Instrum. Methods Phys. Res., Sect. B, 379, 4 (2016)
[5] O. M. Merdrignac et al., Sens. Actuators B 7, 4 (1992)
[6] Y. R. Luo, Comprehensive Handbook of Chemical Bond Energies, Crc Press, Boca Raton, Fl, 2007
[7] N. Lavanya et al., Nanotechnology 27, 7 (2016)

Performance of SnO_2-based chemosensors after irradiation with γ–rays and α-particles – Part 2: H_2O sensing

N.M. Chiera (PSI), M. Kasprzak (PSI) P. Steinegger (PSI&ETHZ), G. Zonta (UNIFE), M. Astolfi (UNIFE), C. Malagù (UNIFE)

Introduction

In the second part of this project, the performance of irradiated SnO_2(Au)- and STN-based chemosensors in the detection of H_2O traces was tested. The experiments were conducted by employing a gas-loop system available at the Laboratory of Radiochemistry of PSI. The real-time performance of the α- and γ-irradiated SnO_2(Au) and STN sensors when changing the H_2O content in the gas carrier is here discussed.

Experimental

SnO_2- and STN-based semiconductor sensors were prepared at UNIFE and irradiated at PSI following the procedure described in the first part of this project [1]. Two sensors (one per type of sensing material) were not subjected to any irradiation and therefore were employed as non-irradiated controls. For the real-time H_2O detection experiments, a portable gas-sensing unit, capable of hosting simultaneously up to four sensors, was connected to a gas-loop system as depicted in figure 1. The gas was introduced into the gas loop via separate mass flow controllers (Brooks Instruments) up to a certain system pressure. Once isolated from the gas-feed, metal bellow pumps (Senior Metal Bellows) ensured the gas flow within the loop, regulated by mass flow controllers (Brooks Instruments, 50-1000 mL/min range). The pulsed gas flow originating from the bellow pumps was minimized by a 10-liter buffer volume. The gas was then increasingly dried by continuously passing through a drying unit containing a mixture of silica zeolites and phosphorus pentoxide (SICAPENT®, Merck Millipore). The drying unit could be bypassed using manually operated three-way valves. After exiting the drying unit, the gas passed through the portable gas-sensing device, containing the chemoresistive sensors, to be then fed back to the loop system. The gas-sensing device was connected to the gas-loop system via two short polytetrafluoroethylene tubes (internal Ø = 4 mm) used as a gas-input and a gas-output, respectively. The gas-loop system was equipped with a dew point meter (CS Instruments) and an electronic manometer (Kobold). The portable gas-sensing device hosted four hermetically sealed single-sensor chambers, placed in series. The electronic system consisted of five dedicated electronic boards (one for each sensor and one for the power supply, MD® s.r.l.) that established the connection to the power supplies and to the sensor heating controls, thus, allowing for the digitalization and the acquisition of all the sensor signals. The gas-sensing unit was connected to a touch screen (Raspberry Pi®) and a custom-made software for the on-line visualization of the sensor response as a function of time. The online measurements were performed by testing the SnO_2(Au) and the STN materials separately. First, the SnO_2(Au)-based sensors were inserted in the portable gas-sensing device and connected to the gas-loop system. After evacuating the system from any residual air, pure He (>99.99 vol% purity) was fed into the gas-loop. The pressure in the system was kept at 0.625 bar (absolute pressure) during the whole experiments. In a first step, the gas-loop, with the drying cartridge bypassed, was used to continuously cycle the carrier gas for 2 hours at 500 mL/min over the sensor units, while recording the sensor V_{air} voltages. In a second step, the gas carrier was passed through the drying cartridge before continuing to the sensors, while again recording the measured voltage (V_{gas}) as a function of time. The sensor response (R) was calculated as:

$$R = V_{gas} / V_{air} \quad (1)$$

During the conducted experiments, the drying unit was repeatedly bypassed on and off multiple times. Discrete dew point values were registered at different measurement intervals. The STN-based chemosensors were tested following the same procedure.

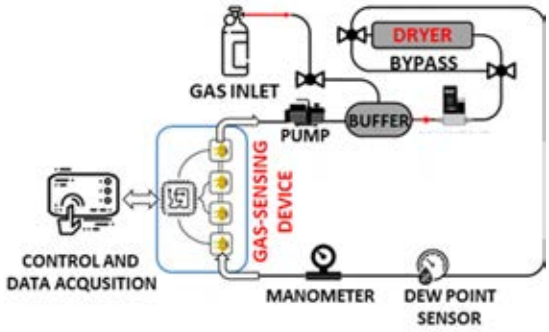

Figure 1: Gas-loop system coupled to the portable gas-sensing device. The gas flow direction is indicated (white arrows).

Results and discussion

It is known that the sensing property of the SnO_2 material towards H_2O is based on the adsorption of water onto the SnO_2 surface, followed by the dissociation of the H_2O molecule and the simultaneous oxidation of SnO_2 [1]. Recent theoretical calculations

[2] showed that the occupation of the oxygen vacancies in SnO_2 materials by atmospheric oxygen stabilizes the associatively adsorbed H_2O molecule and prevents the oxidation of SnO_2. Therefore, the electron transfer from the SnO_2 material to the target gas does not occur, which translates into a decreased gas sensing response towards H_2O. This effect is indeed observed for the α-irradiated SnO_2(Au)-based sensor (see figure 2), in which oxygen vacancies are created after the particle irradiation. As pointed out in the first part of this project, due to the stronger bonds of the STN material, α-irradiation does not favour the creation of oxygen vacancies in this type of semiconductor. Instead, other changes that affect predominantly the electrical characteristics of the sensors are promoted. As shown in figure 3, the electrical changes upon α-irradiation lead to an increase of the response of the STN-based sensor towards H_2O by a factor of ≈ 3.5. In the first part of this project it was assumed that γ-irradiation of the SnO_2(Au) and the STN materials leads to similar electrical changes in both materials, as for example, the creation of free charge carriers.

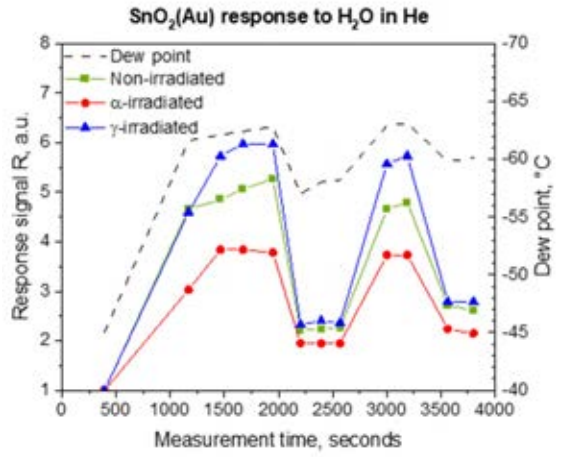

Figure 2: Responses of the non-irradiated (green line), α-irradiated (red line), and γ–irradiated (blue line) SnO_2(Au)-based sensors. The dashed line indicates the measured dew point values.

This translates into a higher sensitivity of both SnO_2(Au) and STN sensors towards H_2O, in comparison to the respective non-irradiated ones. As shown in figure 3, the improvement in the sensitivity of the γ-irradiated STN-based sensors towards H_2O is not as pronounced as after α-irradiation.

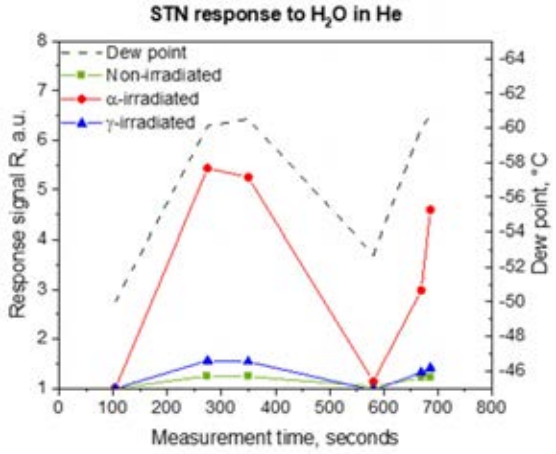

Figure 3: Responses of the non-irradiated (green line), α-irradiated (red line), and γ–irradiated (blue line) STN-based sensors. The dashed line indicates the measured dew point values.

This could be explained by the lower ionizing power and linear energy transfer of γ-rays in comparison to the one of α-particles, which leads to the creation of a lower amount of structural changes in the irradiated material. Having said that, an in-depth understanding of the underlying physical phenomena governing the sensor performance after exposure to α- or γ-radiation needs dedicated experimental studies.

Both material types showed a rapid real-time response to sudden changes of water vapour. As in the gas-sensing of CO, these first results point to the possibility of exploiting different types of irradiation to increase the sensitivity of each material towards specific gas components, confirming the observations made in [5]. Additional studies will envisage the real-time gas-sensing response of the SnO_2(Au) and STN materials while being subjected to an increasing dose of γ-radiation at the Calibration Laboratory of PSI.

References

[1] K. Watanabe et al., Proceedings IMCS P2.0, 3 (2012).
[2] G. Santarossa et al., Langmuir 29, 12 (2013).
[3] O. M. Merdrignac et al., Sens. Actuators B 7, 4 (1992).

Report on the 30th Conference of the International Nuclear Targets Development Society, INTDS 2022, 25 – 30 September 2022 at PSI

D. Schumann (PSI)

Society

The International Nuclear Targets Development Society – INTDS (https://www.intds.org/) - is a non-profit organization that focuses on establishing and fostering a target preparation network and the support of target producing research groups to enable successful experiments in a broad variety of scientific research fields in physics, chemistry and related sciences.

The society performs annual member meetings and a scientific conference every second year. INTDS2020, originally foreseen to be performed in September 2020, had to be postponed for two years due to the pandemic. The more we were happy to eventually host the conference in September 2022 at PSI as INTDS2022.

Scope of INTDS 2022

Despite the importance of beam facilities, detectors and elaborated data analysis, the target is one of the indispensable components in scientific experiments aimed to investigate nuclear reactions. Targets play also an important role for the performance of nuclear installations, for instance spallation neutron sources. Correspondingly, there is a strong influence of the target quality on the quality of the final experimental result. The INTDS conferences are aimed to bring together target makers and users from all over the world to report about newest developments, share their knowledge, share their problems, build up synergies for efficient use of the available resources and foster their networks to be able to produce:

"Tailored Targets for Science".

Topics

- Preparation techniques for thin films, e.g., vacuum evaporation/condensation, sputtering, electro-chemical deposition, powder distribution, rolling etc.
- Separation and chemical processing of stable and radioactive isotopes
- Preparation and characterization of high-purity and special materials
- Development of highly material-conservative methods of preparation
- Effects of contaminants
- Target and sample encapsulation
- Radiation and beam heating effects
- Targets for radionuclide production
- Liquid and gas targets
- Availability of isotopes
- Target and sample thicknesses from gas densities up to kg/cm^2
- Isotopically enriched and radioactive targets
- Beam charge strippers (foil, liquid, gas, plasma)
- Targets for high intensity beams
- Target characterization
- Targets for special applications (medical, industrial, controlled fusion)

Event

The conference took place in the main Auditorium of the Paul Scherrer Institut in Villigen, Switzerland. Around 80 participants from Africa, Asia, Europe and North America attended the conference. A total of 51 scientific contributions were presented in 12 sessions.

Figure 1: Participants of the 30th conference of the International Nuclear Targets Development Society

The scientific program covered reports on the development of new target preparation methods, advances in target characterization, recent results in the production of targets for medical applications, gas targets and much more (https://indico.psi.ch/event/7834/). It is particularly gratifying that we had been able to establish a session on new developments in high-power target technology again this year. We also heard news about targets for ion beams and recent research results in the field of stripper films.

Besides the broad field of stable targets, which was covered in two sessions, radioactive targets play an essential role in many areas of nuclear research. In addition to the targets, there is an increasing demand for the availability of radioactive starting material. Therefore, both a special session on isotope production

and one on actinide target production had been included.

INTDS places special emphasis on supporting young scientists. This concern was reflected both in the financial support and in the large number of contributions from students. To emphasize the importance of teaching, a special session on educational topics was established.

Members meeting and executive board elections

The annual meeting of the members of the INTDS was held on Thursday, 29th September 2022, afternoon. Besides the usual service business, the membership and financial status report, the minutes of the previous meeting, the newsletter etc., two members were elected as new directors to the executive board: Emilio A. Maugeri (PSI) and Wim Weterings (CERN). The complete list of the executive board directors can be found on the website https://www.intds.org/societys-board/ .

The next conference has been scheduled for autumn 2024 and will be hosted by Oak Ridge National Laboratory (ORNL, USA).

Social events

The conference started with a Welcome reception on Sunday evening with the excellent catering service of PSI OASE.

On Wednesday afternoon, we visited the beautiful city of Lucerne – unfortunately under very bad weather conditions. After a guided tour through the city, we enjoyed a typical Swiss dinner during a boat trip on Lake Lucerne including an exciting mental close-up performance by S. Taut: the ART OF THE MARVELOUS (http://www.steffentaut.de).

Figure 2: The mentalist S. Taut presenting his show of the "marvelous" during the boat tour at lake Lucerne

A visit to the PSI accelerator facilities was performed on Friday morning.

Proceedings

Conference proceedings will be published online, with open access, in the European Physics Journal Web of Conferences.

EPJ Web of Conferences

Acknowledgements

Numerous colleagues helped to make the conference a success. In particular, we acknowledge the work of the scientific advisory board and the local organizers A. Blattmann, M. Veicht, N. Cerboni, E. Maugeri, R. Dressler, D. Kiselev and Z. Talip.

Excellent work was done by the PSI facility managing service, the printing office, the visitor centre, the kitchen team of the canteen OASE and the colleagues from PSI West who performed the guided tour through the accelerator facilities.

Special thanks go to P. Grundler for taking the conference photos.

Finally, we would like to thank all the sponsors, whose generous donations helped to put together an interesting and varied social program.

NuPECC
Tektronix KEITHLEY
TRISKEM Expertise in Separation Chemistry
GoodFellow Your global supplier for materials
MIRION TECHNOLOGIES
Eckert & Ziegler wir helfen zu heilen
MICROMATTER TECHNOLOGIES INC.

PAUL SCHERRER INSTITUT

LABORATORY OF RADIOCHEMISTRY OF THE PAUL SCHERRER INSTITUT

31.12.2022

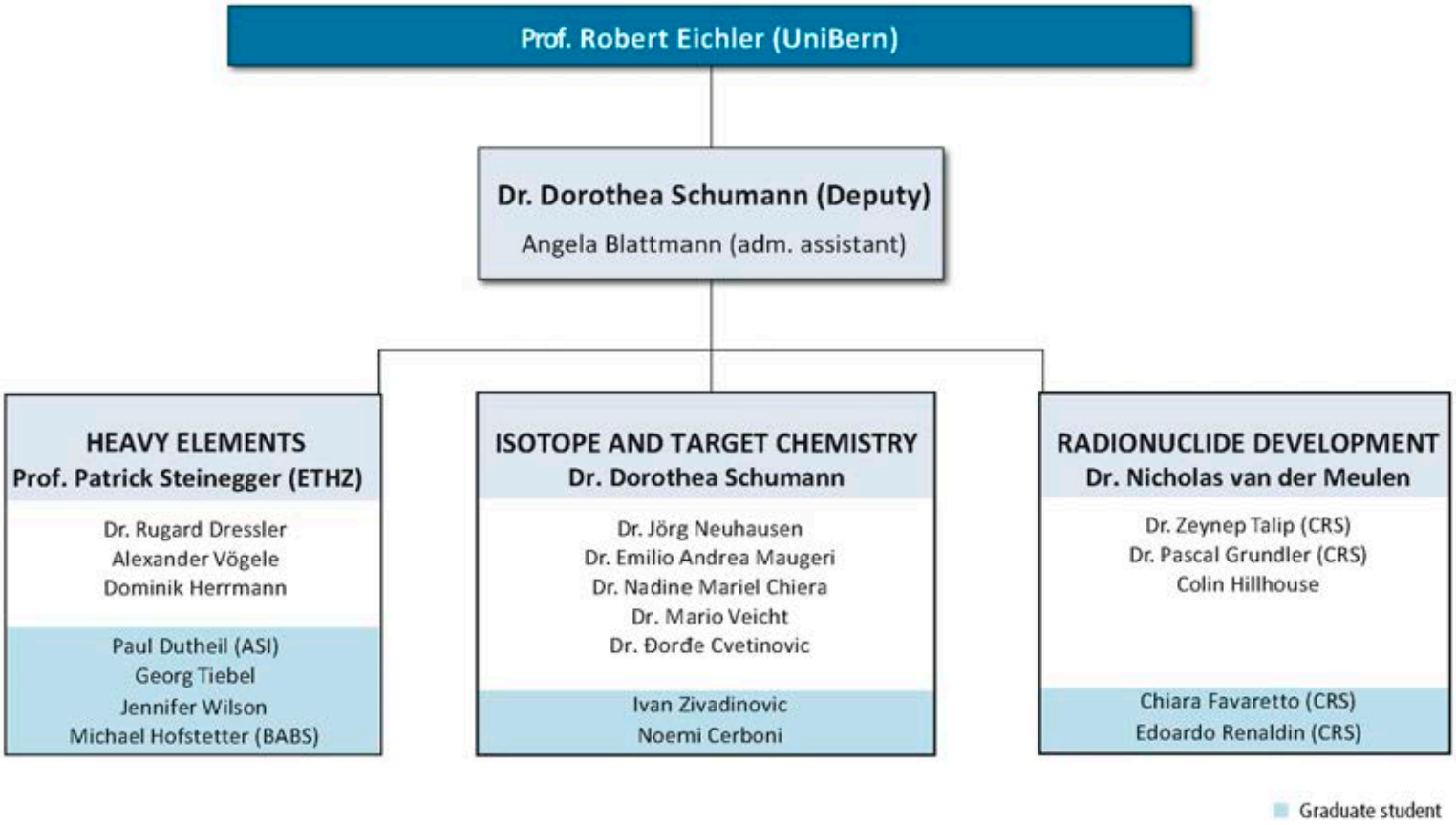

List of publications

Ayyad, Y.; Mittig, W.; Tang, T.; Olaizola, B.; Potel, G.; Rijal, N.; Watwood, N.; Alvarez-Pol, H.; Bazin, D.; Caamaño, M.; et al.
Evidence of a near-threshold resonance in ^{11}B relevant to the b-delayed proton emission of ^{11}B
Phys. Rev. Lett. 2022, 129 (1), 012501 (5 pp.), https://doi.org/10.1103/PhysRevLett.129.012501

Babiano-Suarez, V.; Balibrea-Correa, J.; Caballero-Ontanaya, L.; Domingo-Pardo, C.; Ladarescu, I.; Lerendegui-Marco, J.; Tain, J. L.; Calviño, F.; Casanovas, A.; Tarifeño-Saldivia, A.; et al.
First $^{80}Se(n,\gamma)$ cross section measurement with high resolution in the full stellar energy range 1 eV - 100 keV and its astrophysical implications for the s-process
EPJ Web Conf. 2022, 260, 11026 (8 pp), https://doi.org/10.1051/epjconf/202226011026

Biswas, S.; Gerchow, L.; Luetkens, H.; Prokscha, T.; Antognini, A.; Berger, N.; Cocolios, T. E.; Dressler, R.; Indelicato, P.; Jungmann, K.; et al.
Characterization of a continuous muon source for the non- destructive and depth-selective elemental composition analysis by Muon Induced X- and gamma-rays
Appl. Sci. 2022, 12 (5), 2541 (14 pp.), https://doi.org/10.3390/app12052541

Borgna, F.; Haller, S.; Monné Rodriguez, J. M.; Ginj, M.; Grundler, P. V.; Zeevaart, J. R.; Köster, U.; Schibli, R.; van der Meulen, N. P.; Müller, C.
Combination of terbium-161 with somatostatin receptor antagonists - a potential paradigm shift for the treatment of neuroendocrine neoplasms
Eur. J. Nucl. Med. and Molecular Imaging 2022, 49, 1113-1126, https://doi.org/10.1007/s00259-021-05564-0

Braccini, S.; Carzaniga, T. S.; Dellepiane, G.; Grundler, P. V.; Scampoli, P.; van der Meulen, N. P.; Wüthrich, D.
Optimization of ^{68}Ga production at an 18 MeV medical cyclotron with solid targets by means of cross-section measurement of ^{66}Ga, ^{67}Ga and ^{68}Ga
Appl. Radiat. Isot. 2022, 186, 110252 (9 pp.), https://doi.org/10.1016/j.apradiso.2022.110252

Chiera, N. M.; Dressler, R.; Sprung, P.; Talip, Z.; Schumann, D.
High precision half-life measurement of the extinct radio-lanthanide Dysprosium-154
Sci. Rep. 2022, 12 (1), 8988 (10 pp.), https://doi.org/10.1038/s41598-022-12684-6

Chiera, N. M.; Maugeri, E. A.; Danilov, I.; Balibrea-Correa, J.; Domingo- Pardo, C.; Köster, U.; Lerendegui-Marco, J.; Veicht, M.; Zivadinovic, I.; Schumann, D.
Preparation of PbSe targets for ^{79}Se neutron capture cross section studies
Nucl. Instrum. Methods Phys. Res. A 2022, 1029, 166443 (7 pp.), https://doi.org/10.1016/j.nima.2022.166443

De Gerone, M.; Bevilacqua, A.; Biasotti, M.; Borghesi, M.; Cerboni, N.; Ceruti, G.; De Bodin De Galembert, G.; Faverzani, M.; Fedkevych, M.; Ferri, E.; et al.
Commissioning of the ion implanter for the HOLMES experiment
J. Low Temp. Phys. 2022, 209, 1135-1142, https://doi.org/10.1007/s10909-022-02752-6

De Gerone, M.; Alpert, B.; Balata, M.; Becker, D. T.; Bennett, D. A.; Bevilacqua, A.; Borghesi, M.; Ceruti, G.; De Bodin De Galembert, G.; Dressler, R.; et al
Status of the HOLMES experiment
J. Low Temp. Phys. 2022, 209, 980-987, https://doi.org/10.1007/s10909-022-02895-6

Dellepiane, G.; Casolaro, P.; Favaretto, C.; Grundler, P. V.; Mateu, I.; Scampoli, P.; Talip, Z.; van der Meulen, N. P.; Braccini, S.
Cross section measurement of terbium radioisotopes for an optimized ^{155}Tb production with an 18 MeV medical PET cyclotron
Appl. Radiat. Isot. 2022, 184, 110175 (14 pp.), https://doi.org/10.1016/j.apradiso.2022.110175

Durán, M. T.; Juget, F.; Nedjadi, Y.; Bailat, C.; Grundler, P. V.; Talip, Z.; van der Meulen, N. P.; Casolaro, P.; Dellepiane, G.; Braccini, S.
Half-life measurement of ^{44}Sc and ^{44m}Sc
Appl. Radiat. Isot. 2022, 190, 110507 (10 pp.), https://doi.org/10.1016/j.apradiso.2022.110507

Ferri, E.; Alpert, B.; Balata, M.; Becker, D. T.; Bennett, D. A.; Borghesi, M.; De Gerone, M.; Dressler, R.; Faverzani, M.; Fedkevych, M.; et al.
Multiplexed superconducting detectors for a neutrino mass experiment
IEEE Trans. Appl. Supercond. 2022, 32 (45), 2100204 (4 pp.), https://doi.org/10.1109/TASC.2021.3135794

Gallucci, G.; Bevilacqua, A.; Biasotti, M.; Borghesi, M.; Cerboni, N.; Ceruti, G.; De Bodin De Galembert, G.; De Gerone, M.; Faverzani, M.; Fedkevych, M.; et al.
Status of the HOLMES experiment: commissioning of the ion implanter. In The 22nd international workshop on neutrinos from accelerators (NuFact2021), presented at the The 22nd international workshop on neutrinos from accelerators (NuFact2021), Cagliari, Italy, September 6-11, 202
Proceedings of science; Sissa Medialab srl: Trieste, 2022; Vol. 402, p 161 (6 pp.),
https://doi.org/10.22323/1.402.0161

Gäggeler, H. W.; Eichler, B.; Jost, D. T.; Eichler, R.
On the volatility of protactinium in chlorinating and brominating gas media
Radiochim. Acta 2022, 110 (6-9), 495-504, https://doi.org/10.1515/ract-2021-1128

Heinitz, S.; Kajan, I.; Schumann, D.
How accurate are half-life data of long-lived radionuclides?
Radiochim. Acta 2022, 110 (6-9), 589-608, https://doi.org/10.1515/ract-2021-1135

Hemmingsson, J.; Svensson, J.; van der Meulen, N. P.; Müller, C.; Bernhardt, P.
Active bone marrow S-values for the low-energy electron emitter terbium-161 compared to S-values for lutetium-177 and yttrium-90
EJNMMI Phys. 2022, 9 (1), 65 (13 pp.), https://doi.org/10.1186/s40658-022-00495-7

Juget, F.; Talip, Z.; Nedjadi, Y.; Durán, M. T.; Grundler, P. V.; Zeevaart, J. R.; van der Meulen, N. P.; Bailat, C.
Precise activity measurements of medical radionuclides using an ionization chamber: a case study with Terbium-161
EJNMMI Phys. 2022, 9 (1), 19 (18 pp.), https://doi.org/10.1186/s40658-022-00448-0

Kajan, I.; Pommé, S.; Heinitz, S.
Measurement of the ^{171}Tm half-life
J. Radioanal. Nucl. Chem. 2022, 331, 645-653, https://doi.org/10.1007/s10967-021-08108-w

Kneip, N.; Studer, D.; Kieck, T.; Ulrich, J.; Dressler, R.; Schumann, D.; Wendt, K.
Separation of manganese isotopes by resonance ionization mass spectrometry for ^{53}Mn half-life determination
EPJ Appl. Phys. 2022, 97, 19 (7 pp.), https://doi.org/10.1051/epjap/2022210270

Lederer-Woods, C.; Aberle, O.; Andrzejewski, J.; Audouin, L.; Bécares, V.; Bacak, M.; Balibrea, J.; Barbagallo, M.; Barros, S.; Battino, U.; et al.
^{74}Ge(n, γ) cross section below 70 keV measured at n_TOF CERN
Eur. Phys. J. A 2022, 58 (12), 239 (9 pp.), https://doi.org/10.1140/epja/s10050-022-00878-5

Lerendegui-Marco, J.; Babiano-Suárez, V.; Balibrea-Correa, J.; Babiano-Suárez, V.; Caballero, L.; Calvo, D.; Domingo-Pardo, C.; Ladarescu, I.; Real, D.; Calviño, F.; et al.
Compton Imaging and Machine-Learning techniques for an enhanced sensitivity in key stellar (n,γ) measurements
EPJ Web Conf. 2022, 260, 10002 (8 pp.), https://doi.org/10.1051/epjconf/202226010002

Liu, L.; Maurice, R.; Galland, N.; Moisy, P.; Champion, J.; Montavon, G.
Pourbaix diagram of astatine revisited: experimental investigations
Inorg. Chem. 2022, 61 (34), 13462-13470, https://doi.org/10.1021/acs.inorgchem.2c01918

Mastromarco, M.; Amaducci, S.; Colonna, N.; Finocchiaro, P.; Cosentino, L.; Barbagallo, M.; Aberle, O.; Andrzejewski, J.; Audouin, L.; Bacak, M.; et al.
High accuracy, high resolution ^{235}U(n,f) cross section from n_TOF (CERN) from 18 meV to 10 keV.
Eur. Phys. J. A 2022, 58 (8), 147 (13 pp.), https://doi.org/10.1140/epja/s10050-022-00779-7

Moreno-Soto, J.; Valenta, S.; Berthoumieux, E.; Chebboubi, A.; Diakaki, M.; Dridi, W.; Dupont, E.; Gunsing, F.; Krtička, M.; Litaize, O.; et al.
Constraints on the dipole photon strength for the odd uranium isotopes
Phys. Rev. C 2022, 105 (2), 024618 (14 pp.), https://doi.org/10.1103/PhysRevC.105.024618

Schlomberg, M.; Vockenhuber, C.; Synal, H. A.; Veicht, M.; Mihalcea, I.; Schumann, D.
Isobar separation of ^{32}Si from ^{32}S in AMS using a passive absorber
Nucl. Instrum. Methods Phys. Res. B 2022, 533, 56-60, https://doi.org/10.1016/j.nimb.2022.09.029

Tagliente, G.; Kopecky, S.; Heyse, J.; Krtička, M.; Massimi, C.; Mengoni, A.; Milazzo, P. M.; Plompen, A. J. M.; Schillebeeckx, P.; Valenta, S.; et al.
^{92}Zr(n, γ) and (n,tot) measurements at the GELINA and n_TOF facilities
Phys. Rev. C 2022, 105 (2), 025805 (14 pp.), https://doi.org/10.1103/PhysRevC.105.025805

Tiebel, G.; Dutheil, P.; Dressler, R.; Eichler, R.; Herrmann, D.; Steinegger, P.
The SINQ gas-jet facility as a source for radionuclides from neutron-induced fission of ^{235}U
Nucl. Instrum. Methods Phys. Res. A 2022, 1041, 167360 (9 pp.), https://doi.org/10.1016/j.nima.2022.167360

Tosato, M.; Verona, M.; Favaretto, C.; Pometti, M.; Zanoni, G.; Scopelliti, F.; Cammarata, F. P.; Morselli, L.; Talip, Z.; van der Meulen, N. P.; et al.
Chelation of theranostic copper radioisotopes with S-rich macrocycles: from radiolabelling of copper-64 to in vivo investigation
Molecules 2022, 27 (13), 4158 (19 pp.), https://doi.org/10.3390/molecules27134158

Veicht, M.; Mihalcea, I.; Gautschi, P.; Vockenhuber, C.; Maxeiner, S.; David, J. C.; Chen, S.; Schumann, D.
Radiochemical separation of ^{26}Al and ^{41}Ca from proton-irradiated vanadium targets for cross-section determination by means of AMS
Radiochim. Acta 2022, 110 (10), 809-816, https://doi.org/10.1515/ract-2022-0036

Weiss, C.; Wilson, J.; Tiebel, G.; Steinegger, P.; Griesmayer, E.; Frais- Kölbl, H.; Dressler, R.; Camarda, M.; Areste, M. del M. C.
High- temperature performance of solid-state sensors up to 500 °C.
Nucl. Instrum. Methods Phys. Res. A 2022, 1040, 167182 (4 pp.), https://doi.org/10.1016/j.nima.2022.167182

Book chapter

Heinz Gäggeler, Soenke Szidat
Nuclear Dating
Nuclear- and Radiochemistry, Vol. 2, 2nd Ed. (Frank Rösch, Editor), pp 137-173 ISBN 978-3-11-074267-1 2022 Walter de Gruyter GmbH, Berlin/Boston

Internal reports

Eichler, R.; Kiselev, D.; Koschik, A.; Knecht, A.; van der Meulen, N. P.; Scheibl, R.; Barth, L.; Baumgarten, C.; Caminada, L.; Chang, J.; et al.
IMPACT conceptual design report
PSI Bericht; Report No.: 22-01; Paul Scherrer Institut: Villigen PSI, 2022; 302

Contributions to conferences, workshops and seminars

N. Cerboni
Development of Electrochemical Methods for the Production of Thin Film Lanthanides
LRC Seminar, Paul Scherrer Institut, Villigen PSI, Switzerland, April 08, 2022

N. Cerboni
Preparation of Thin Film Sources of Radiolanthanides for the Measurement of Auger Electron Energies and Branching Ratios
NES PhD Day 2022, Paul Scherrer Institut, Villigen PSI, Switzerland, May 03, 2022

N. Cerboni
Preparation and Characterization of Holmium Sources for the HOLMES Experiment
Seminar for the HOLMES Project, National Institute of nuclear Physics (INFN), Genoa, Italy, May 12, 2022

N. Cerboni
Preparation of Thin Film Sources of Radiolanthanides for the Measurement of Auger Electrons
19th Radiochemical Conference (RadChem-2022), Marianske Lazne, Czech Republic, May 15 – 20, 2022

N. Cerboni
Analysis of Thin Tb/Pd Intermetallic Targets Prepared by the Coupled Reduction Reaction
30th Conference of the International Nuclear Target Development Society (INTDS2022), Villigen PSI, Switzerland, September 25 – 30, 2022

N. M. Chiera
PbSe targets for nuclear physics studies
20th Young Researchers' Conference, Belgrade, Serbia, November 30 – December 02, 2022

N. M. Chiera
Revival of gas-phase chemistry with oxychlorides of transactinides: The case of Dubnium, element 105
Jahrestagung der Fachgruppe Nuklearchemie 2022, Germany, October 04 – 06, 2022

N. M. Chiera
Production of PbSe targets for neutron capture cross section studies
30th Conference of the International Nuclear Target Development Society (INTDS2022), Villigen PSI, Switzerland, September 25 – 30, 2022

N. M. Chiera
Latest half-life measurements of ^{146}Sm, ^{148}Gd, and ^{154}Dy at Paul Scherrer Institute
Nuclear Physics in Astrophysics – X (NPAX), Switzerland, September 04 – 09, 2022

N. M. Chiera
High precision re-determination of the half-lives of ^{146}Sm, ^{148}Gd, and ^{154}Dy
15th International Conference on Nuclear Data for Science and Technology (ND2022) – USA, July 24 – 29, 2022 (online)

N. M. Chiera
Updating the nuclear databases: re-measurement of the half-life of ^{146}Sm, ^{148}Gd, and ^{154}Dy
19th Radiochemical Conference (RadChem-2022), Marianske Lazne, Czech Republic, May 15 – 20, 2022

N. M. Chiera
Half-life measurement of the exotic radio-lanthanides ^{148}Gd, ^{146}Sm, and ^{154}Dy
LRC Seminar, Paul Scherrer Institut, Villigen PSI, Switzerland, March 18, 2022

Đ. Cvjetinović
^{32}Si Geochronometer: Radiochemical separation and purification of ^{32}Si for half-life redetermination
20th Young Researchers' Conference, Belgrade, Serbia, November 30 – December 02, 2022

Đ. Cvjetinović
Glucosomes: Magnetically induced controlled release of glucose modified liposomes
20th Young Researchers' Conference, Belgrade, Serbia, November 30 – December 02, 2022

R. Dressler
Evaluation of Adsorption Enthalpies in Isothermal Chromatography Experiments under non-optimal Conditions - the case of Tl and TlOH on fused silica
19th Radiochemical Conference (RadChem-2022), Marianske Lazne, Czech Republic, May 15 – 20, 2022

R. Dressler
Neutron capture cross-section measurements of ^{53}Mn
15th International Conference on Nuclear Data for Science and Technology (ND2022) – USA, July 24 – 29, 2022 (online)

R. Dressler
Isotope Production at PSI
30th Conference of the International Nuclear Target Development Society (INTDS2022), Villigen PSI, Switzerland, September 25 – 30, 2022

P. Dutheil
Further steps towards electrochemical separation of transition metal radionuclides
LRC Seminar, Paul Scherrer Institut, Villigen PSI, Switzerland, March 18, 2022

P. Dutheil
Electrochemical separation of ^{60}Co from electropositive radionuclides for radioanalysis
MARC XII, Kona, Hawaii, United States, April 03 – 08, 2022

R. Eichler
TATTOOS - Plans for The New Swiss Isotope Production Facility @ PSI
19th Radiochemical Conference (RadChem-2022), Marianske Lazne, Czech Republic, May 15 – 20, 2022

R. Eichler
IMPACT-TATTOOS as part of the "Infrastructure Roadmap" Initiative: Challenges of the Design Concepts
30th Conference of the International Nuclear Target Development Society (INTDS2022), Villigen PSI, Switzerland, September 25 – 30, 2022

R. Eichler
IMPACT-TATTOOS The Future Swiss Isotope Production Facility for Nuclear and Life Science
Jahrestagung GDCh Fachgruppe Nuklearchemie 2022, Bergisch Gladbach, Germany, October 04 – 06, 2022

R. Eichler
Emerging opportunities for radionuclide delivery for radiochemical research in Switzerland (invited online)
SESTEC 2022, Mumbai, India, November 22 – 26, 2022 (online)

C. Favaretto
Production and radiochemical separation of terbium-155 from enriched gadolinium target material and its preliminary application in SPECT imaging
iSRS 2022, Nantes, France, 30 May – June 02, 2022

C. Favaretto
Production and radiochemical separation of the radiolanthanide terbium-155 for potential application in SPECT imaging
SCR 2022, Fribourg, Switzerland, June 23, 2022

P. V. Grundler
Purification of ^{67}Ga towards preclinical studies
NRP78 Covid-19 Research Seminar, April 08, 2022

M. Hofstetter
Unravelling the Origin of Uranium Material
LRC Seminar, Paul Scherrer Institut, Villigen PSI, Switzerland, December 09, 2022

L. Liu
Status of Task 3.1 – Fission product release from HLM and deposition from the gas phase
4th PASCAL progress meeting, Bologna, Italy, October 17 – 19, 2022 (online)

L. Liu
Task 3.1 – Fission product release from HLM and deposition from the gas phase
3rd PASCAL progress meeting, Gothenburg, Sweden, May 02 – 04, 2022

L. Liu
Investigation on the chemical behavior of cesium and iodine in lead-bismuth liquid metal solution
19th Radiochemical Conference (RadChem-2022), Marianske Lazne, Czech Republic, May 15 – 20, 2022

L. Liu
Investigation on the chemical behavior of cesium and iodine in lead-bismuth liquid metal solution
LRC Seminar, Paul Scherrer Institut, Villigen PSI, Switzerland, October 14, 2022

E. A. Maugeri
Target production at PSI: a brief overview
SANDA WP3-Target Preparation for improvement of Nuclear Data Measurements, March 10, 2022

E.A. Maugeri
Improvement of targetry methods for nuclear data measurements
15th International Conference on Nuclear Data for Science and Technology (ND2022) – USA, July 24 – 29, 2022 (online)

E. A. Maugeri
The importance of targetry in nuclear physics and astrophysics experiments
Nuclear Physics in Astrophysics – X (NPAX), Switzerland, September 04 – 09, 2022

E. A. Maugeri
Targetry of Rare Isotopes at PSI
30th Conference of the International Nuclear Target Development Society (INTDS2022), Villigen PSI, Switzerland, September 25 – 30, 2022

E. A. Maugeri
Sample production at PSI
One-day meeting on (n,cp) reactions at n_TOF, Catania, Italy, July 20, 2022

J. Neuhausen
WP12- Chemistry control experiments and modelling
4th PATRICIA Technical Coordination Board Meeting, March 22, 2022 (online)

J. Neuhausen
WP12- Chemistry control experiments and modelling
PATRICIA Reporting period 1 Technical Review Meeting, March 30, 2022 (online)

J. Neuhausen, A. Aerts
Radionuclide release from HLM, Chemical aspects
3rd PASCAL progress meeting, Gothenburg, Sweden, May 02 – 04, 2022
J. Neuhausen
WP12- Chemistry control experiments and modelling
5th PATRICIA Technical Coordination Board Meeting, Karlsruhe, Germany, November 02, 2022 (online)

J. Neuhausen
WP12- Chemistry control experiments and modelling
5th PATRICIA Technical Review Meeting, Karlsruhe, Germany, November 03, 2022 (online)

D. Schumann
Target Preparation for Improvement of Nuclear Data Measurements – Status report
SANDA workshop March 06 – 11, 2022 (online)

D. Schumann
Radiochemistry – just a tool or an essential part in nuclear science?
19th Radiochemical Conference (RadChem-2022), Marianske Lazne, Czech Republic, May 15 – 20, 2022 (invited)

D. Schumann
Half-life determination of long-lived hard-to-measure radionuclides: examples ^{53}Mn and ^{93}Mo
15th International Conference on Nuclear Data for Science and Technology (ND2022) – USA, July 24 – 29, 2022 (online)

D. Schumann
Harvesting Exotic Radionuclides at PSI
6th INCC, August 29 – September 02, 2022 (invited online)

D. Schumann
Status of the SINCHRON project
5th SINCHRON Meeting Lausanne, Switzerland, August 25 – 26, 2022

D. Schumann
WP3: Target Preparation for Improvement of Nuclear Data Measurements
SANDA REVIEW meeting, November 30, 2022 (online)

P. Steinegger
Chemistry with Superheavy Elements at FLNR and PSI
19th Radiochemical Conference (RadChem-2022), Marianske Lazne, Czech Republic, May 15 – 20, 2022, (invited)

P. Steinegger
Prospects in experimental superheavy element chemistry
REHE Conference 2022, Assisi, Italy, September 26 – 30, 2022 (invited)

P. Steinegger
Status and perspectives of chemistry studies with superheavy elements at the SHE Factory in Dubna
TASCA Workshop 2022, GSI Helmholtzzentrum für Schwerionenforschung, Darmstadt, Germany, May 10 – 12, 2022 (invited online)

Z. Talip
Production of high-specific-activity erbium-169, ytterbium-175 and thulium-167
Terachem 2022, Bressanone, Italy, September 16, 2022

Z. Talip
Target Preparation for Radionuclide Development towards Medical Application at Paul Scherrer Institute
30th Conference of the International Nuclear Target Development Society (INTDS2022), Villigen PSI, Switzerland, September 25 – 30, 2022

Z. Talip
Radiolanthanide toolbox in Nuclear Medicine
PSI Public Tenure Talk, Paul Scherrer Institut, Villigen PSI, Switzerland, October 10, 2022

Z. Talip
WP12 Progress
PRISMAP Consortium Meeting 3, June 16, 2022 (online)

Z. Talip
Radiolanthanides for Nuclear Medicine
DIRK Tenure Talk, Paul Scherrer Institut, Villigen PSI, Switzerland, November 23, 2022

Z. Talip
WP12 Progress
PRISMAP Consortium Meeting 4, November 25, 2022 (online)

G. Tiebel
Chemistry with Transactinide Elements beyond Copernicium and Flerovium
LAC Symposium, ETHZ, Campus ETH Hönggerberg, Zürich, Switzerland, May 11, 2022

G. Tiebel
Nuclear fission products from the SINQ gas-jet facility
19th Radiochemical Conference (RadChem-2022), Marianske Lazne, Czech Republic, May 15 – 20, 2022 (invited)

G. Tiebel
Assessment of the speed of vacuum adsorption chromatography for transactinide research
Jahrestagung GDCh Fachgruppe Nuklearchemie 2022, Bergisch Gladbach, Germany, October 04 – 06, 2022

G. Tiebel
The ion-funnel-to-IVAC system for tests at Texas A&M University
LRC Seminar, Paul Scherrer Institut, Villigen PSI, Switzerland, November 04, 2022

N. P. van der Meulen
Tb radionuclides for imaging and therapy: how far have we progressed?
IAEA Consultants' Meeting on Various routes of production of Tb radionuclides and future radiopharmaceuticals, March 01, 2022 (invited online)

N. P. van der Meulen
Pursuing the theragnostic principle at Paul Scherrer Institute, University of Geneva (UNIGE)
Radiopharmaceutical lecture April 28, 2022 (invited online)

N. P. van der Meulen
The use of PSI's High Intensity Proton Accelerator (HIPA) Complex Towards Medical-Radionuclide Development
International Conference on Accelerators for Research and Sustainable Development, Vienna, Austria, May 23, 2022 (hybrid)

N. P. van der Meulen
Terbium radioisotope production: new opportunities in Switzerland
6th Theranostics World Congress, Wiesbaden, Germany, June 24, 2022 (invited)

N. P. van der Meulen
Pursuing the theragnostic principle at Paul Scherrer Institute
Chinese Society of Nuclear Medicine iSRS meeting, August 19, 2022 (invited)

N. P. van der Meulen
Auger-emitting Radionuclides for Therapy: How Far Have We Progressed?
IAEA Technical Meeting on Auger Electron Emitters for Radiopharmaceutical Developments, Vienna, Austria, September 05, 2022 (invited online)

N. P. van der Meulen
Introduction to Swiss interest in membership of ISOLDE
95th ISOLDE Collaboration Committee meeting, November 07, 2022 (online)

N. P. van der Meulen
Targeted Alpha Tumour Therapy and Other Oncological Solutions (TATTOOS) as part of Paul Scherrer Institute's IMPACT Large Facilities project
PRISMAP Workshop on Emerging Infrastructures and Technical Developments, Legnaro, Italy, November 21, 2022 (online)

N. P. van der Meulen
Is there any new radionuclides of interest out there?
ESRR'22, Verona, Italy, November 27, 2022 (invited)

N. P. van der Meulen
The recent campaign of collection and chemical separation of ^{149}Tb, along with its subsequent application for preclinical therapy studies
ISOLDE Users Workshop, Geneva, Switzerland, December 02, 2022

N. P. van der Meulen
Radionuclide Development – to infinity and beyond!
BIO Audit, May 24, 2022

N. van der Meulen
Radionuclide Development – to infinity and beyond!
PSI-Kazatomprom meeting, November 02, 2022 (online)

M. Veicht
Settling the half-life of ^{32}Si: PSI's contribution to solving a long-lasting issue
NES PhD Day 2022, Paul Scherrer Institut, Villigen PSI, Switzerland, May 03, 2022

M. Veicht
Towards implementing new isotopes for environmental research: The half-life of ^{32}Si
15th International Conference on Nuclear Data for Science and Technology (ND2022), USA, July 24 – 29, 2022 (invited online)

M. Veicht
Re-determination of the ^{32}Si half-life: Status PSI
5th SINCHRON Collaboration Meeting, August 25 – 26, 2022

M. Veicht
A Missing Link: Towards the preparation of a ^{32}Si target for nuclear astrophysics experiments
30th Conference of the International Nuclear Target Development Society (INTDS2022), Villigen PSI, Switzerland, September 25 – 30, 2022

M. Veicht
SINCHRON: A New Chronometer For Nuclear Dating
NES Bereichsleiterkonferenz (BerK), June 23, 2022

J. Wilson
Homolog Studies for Future Chemistry Experiments with Nh
NES PhD Day 2022, Paul Scherrer Institut, Villigen PSI, Switzerland, May 03, 2022

J. Wilson
Online Gas Adsorption Chromatography of Tl/TlOH for Future Nh/NhOH Experiments
19th Radiochemical Conference (RadChem-2022), Marianske Lazne, Czech Republic, May 15 – 20, 2022

J. Wilson
4H-SiC Alpha-Detectors for Future Superheavy Element Experiments
Jahrestagung GDCh Fachgruppe Nuklearchemie 2022, Bergisch Gladbach, Germany, October 04 – 06, 2022

J. Wilson
Preparations for Future Superheavy Element Experiments
LRC Seminar, Paul Scherrer Institut, Villigen PSI, Switzerland, November 04, 2022.

I. Zivadinovic
Transpiration experiments with Po from MEGAPIE samples
5th PATRICIA progress meeting, November 02 – 04, 2022

I. Zivadinovic
Evaporation of polonium from LBE-cooled reactors
20th Young Researchers' Conference, Belgrade, Serbia, November 30 – December 02, 2022

I. Zivadinovic
Sample preparation, radionuclide analytics and radionuclide release experiments
4th PATRICIA progress meeting, March 28 – 30, 2022 (online)

I. Zivadinovic
Determination of the α-activity of polonium in MEGAPIE samples by liquid scintillation counting
19th Radiochemical Conference (RadChem-2022), Marianske Lazne, Czech Republic, May 15 – 20, 2022

I. Zivadinovic
Temperature-dependence on the composition in Ga-doped Ge nanostructures
LRC seminar, Paul Scherrer Institut, Villigen PSI, Switzerland, June 24, 2022

Poster presentations

N. Cerboni
Preparation of Thin Film Sources of Radiolanthanides for the Measurement of Auger Electron Energies and Branching Ratios
NES PhD Day 2022, Paul Scherrer Institut, Villigen PSI, Switzerland, May 03, 2022

N. Cerboni
Investigation of Different Deposition Techniques of Holmium Sources for the Measurement the Electron Neutrino Mass
SCS Fall Meeting 2022, Universität Zürich (Campus Irchel), Zürich, Switzerland, September 08, 2022

N. Cerboni
Investigation of Targets Prepared by the Coupled Reduction Reaction
Jahrestagung GDCh Fachgruppe Nuklearchemie 2022, Bergisch Gladbach, Germany, October 04 – 06, 2022

R. Dressler
Neutron capture cross-section of ^{53}Mn
Nuclear Physics in Astrophysics – X (NPAX), Switzerland, September 04-09, 2022 (online)

P. Dutheil
An electrochemical flow-cell for fast separation of radionuclides
Jahrestagung GDCh Fachgruppe Nuklearchemie 2022, Bergisch Gladbach, Germany, October 04 – 06, 2022.

P. Dutheil
Development of an electrochemical strategy for routine separations of radionuclides
SCS Fall Meeting 2022, Universität Zürich (Campus Irchel), Zürich, Switzerland, September 08, 2022

P. Dutheil
Electrochemical separation of Co-60 for radioanalytics
NES PhD Day 2022, Paul Scherrer Institut, Villigen PSI, Switzerland, May 03, 2022

C. Favaretto
The development of terbium-155 and terbium-161 towards radiotheragnostic clinical applications
Terachem 2022, Bressanone, Italy, September 14 – 17, 2022

P. V. Grundler
Improving the quality of Ga radionuclides to achieve high radiolabeling yields
Terachem 2022, Bressanone, Italy, September 14 – 17, 2022

M. Hofstetter
Lanthanide Isotopes in Uranium Products
SCS Fall Meeting 2022 Universität Zürich (Campus Irchel), Zürich, Switzerland, September 08, 2022

M. Hofstetter
Lanthanide Isotopes in DU Penetrators
Jahrestagung GDCh Fachgruppe Nuklearchemie 2022, Bergisch Gladbach, Germany, October 04 – 06, 2022

L. Liu
Investigation on the chemical behavior of cesium and iodine in lead-bismuth liquid metal solution
SCS Fall Meeting 2022, Universität Zürich (Campus Irchel), Zürich, Switzerland, September 08, 2022

G. Tiebel
Transactinide chemistry in the sup-second regime using vacuum adsorption chromatography
SCS Fall Meeting 2022, Universität Zürich (Campus Irchel), Zürich, Switzerland, September 08, 2022

G. Tiebel
High temperature α-spectroscopy with wide bandgap semiconductor solid-state detectors
NES PhD Day 2022, Paul Scherrer Institut, Villigen PSI, Switzerland, May 03, 2022

N. P. van der Meulen
Targeted Alpha Tumour Therapy and Other Oncological Solutions (TATTOOS) as part of Paul Scherrer Institute's IMPACT Large Facilities project
Terachem 2022, Bressanone, Italy, September 14 – 17, 2022

M. Veicht
Settling the half-life of ^{32}Si: PSI's contribution to solving a long-lasting issue
NES PhD Day 2022, Paul Scherrer Institut, Villigen PSI, Switzerland, May 03, 2022

M. Veicht
Experiment-based determination of the excitation function for the production of 44Ti in proton-irradiated vanadium samples
15th International Conference on Nuclear Data for Science and Technology (ND2022), USA, July 24 – 29, 2022 (online)

J. Wilson
High Temperature Studies with 4H-SiC α-Detectors for Future Superheavy Element Experiments
SCS Fall Meeting 2022, Universität Zürich (Campus Irchel), Zürich, Switzerland, September 08, 2022

I. Zivadinovic
Evaporation of polonium from heavy-liquid-metal-cooled reactors
SCS Fall meeting, ETH Zürich, Zürich, Switzerland, September 08, 2022

I. Zivadinovic
Determination of the α-activity of polonium in MEGAPIE samples by liquid scintillation counting
NES PhD Day 2022, Paul Scherrer Institut, Villigen PSI, Switzerland, May 03, 2022

G. Zonta (presented by N. M. Chiera)
Performance of chemoresistive nanosensors in the detection of gas-phase impurities after irradiation with gamma-rays and alpha particles
SCS Fall Meeting 2022, Universität Zürich (Campus Irchel), Zürich, Switzerland, September 08, 2022

Public relations and outreach activities

P. Steinegger
Women in their element
Rotaract Zürich, Haus zum Rüden, Zürich, Switzerland, May 03, 2022

P. Steinegger
Speeddating mit radioaktiven Schwergewichten
Studieninformationstage 2022, ETHZ (HG), Zürich, Switzerland, September 08, 2022

P. Steinegger
Fantastic elements and where to find them
Inaugural lecture, ETHZ (HG), Zürich, Switzerland, November 09, 2022

P. Steinegger
Fantastische Elemente und wo sie zu finden sind
ETH Unterwegs: Kantonsschule Schaffhausen, Schaffhausen, Switzerland, November 30, 2022

M. Hofstetter, J. Wilson, P. Steinegger
Unterwasserwelten (chemistry experiments with children)
Ferienbetreuung Stiftung kihz, ETHZ (Campus Hönggerberg), Zürich, Switzerland, August 17, 2022

P. Dutheil, M. Hofstetter, G. Tiebel, J. Wilson, I. Zivadinovic
Meeting support + technical support of the meeting organizers
SCS Fall Meeting 2022, Universität Zürich (Campus Irchel), Zürich, Switzerland, September0 08, 2022

Staff of LRC
Radionuklide – Vom Urknall bis zur Anwendung am Patienten
Tag der offenen Tür 2022 (day of the open doors), PSI, Villigen PSI, Switzerland, October 25, 2022

P. Dutheil
Entwicklung von elektrochemischen Methoden für die Radioanalytik
Tag der offenen Tür 2022 (day of the open doors), PSI, Villigen PSI, Switzerland, October 25, 2022

D. Schumann, Z. Talip, E. A. Maugeri, R. Dressler, A. Blattmann, M. Veicht, N. Cerboni
Conference organization, 30th Conference of the International Nuclear Target Development Society
30th Conference of the International Nuclear Target Development Society (INTDS2022), Villigen PSI, Switzerland, September 25 – 30, 2022

B. Osterath (mit D. Herrmann et al.)
Marke Eigenbau
Spectrum 03/2022, PSI, Villigen PSI, Switzerland

Membership in scientific committees and external activities

Prof. Dr. Robert Eichler

Associate Editor of the International Journal of Modern Physics E (IJMPE) World Scientific Publishing
Labor für Ionenstrahlphysik ETH Zürich, Member of Curatorial Board (on behalf of PSI)
Radiochimica Acta, Member of the Scientific Advisory Board

Prof. Dr. Patrick Steinegger

Nuklearforum Schweiz, member
Board Platform Chemistry, Swiss Academy of Sciences

Dr. Nicholas Philip van der Meulen

United States Department of Energy (DOE Isotope R&D FOA), Panel Reviewer
ARRONAX International Scientific Committee
PSI internal research commission (FoKo), member
International Advisory Committee for the Workshop on Targetry and Target Chemistry
Academic Editor for Public Library Of Science (PLOS)
Reviewer Board member: Instruments (MDPI)
Editorial Board member: EJNMMI Radiopharmacy and Chemistry
PSI Team Leader at CERN-ISOLDE

Dr. Dorothea Schumann

Associated editor *nature* Scientific Reports
PSI team leader at n_TOF CERN
SANDA work package leader

Dr Zeynep Talip

PRISMAP work package leader

Dr. Jörg Neuhausen

PATRICIA Work Package Leader

Noemi Cerboni

Co-editor of the International Nuclear Target Development Society (INTDS) newsletter

Lectures and Courses

R. Eichler
Nuclear and Radiochemistry
DCBP University of Bern

R. Eichler
Nuclear Energy Systems (151-0160-00L)
D-MAVT, ETHZ, fall semester 2022

N. Cerboni
Praktikum Allgemeine Chemie (529-0011-04L)
D-CHAB, ETHZ, fall semester 2022

P. Steinegger
Anorganische Chemie I (529-0121-00 V/U)
D-CHAB, ETHZ, fall semester 2022

G. Tiebel
Praktikum Allgemeine Chemie (529-0011-04L)
D-CHAB, ETHZ, January 03 – 24, 2022

J. Wilson
Praktikum Allgemeine Chemie (529-0011-04L)
D-CHAB, ETHZ, January 03 – 24, 2022

E. A. Maugeri
ARIEL-H2020
Samples for nuclear data experiments.
International On-Line School on Nuclear Data: The Path from the Detector to the Reactor Calculation – NuDataPath February 25, 2022

C. Favaretto
Praktikum Biopharmazie (535-0240-00L)
D-CHAB, ETHZ, April – June, 2022

Awards

Noemi Cerboni
Best Presentation Award (1st year PhD)
NES PhD Day 2022, Paul Scherrer Institut, Villigen PSI, Switzerland, May 03, 2022

Mario Veicht
Best Presentation Award (4th year PhD)
NES PhD Day 2022, Paul Scherrer Institut, Villigen PSI, Switzerland, May 03, 2022

Chiara Favaretto
NMB/Eckelman Young Investigator Award 2022
iSRS 2022, Nantes, France, 30 May – June 02, 2022

Noemi Cerboni
1st place students' poster presentation
Jahrestagung GDCh Fachgruppe Nuklearchemie 2022, Bergisch Gladbach, Germany
October 04 – 06, 2022

G. Tiebel
Best Poster Presentation Award (runner-up), SCS Fall Meeting 2022, Universität Zürich (Campus Irchel), Zürich, Switzerland, September 08, 2022

M. Hofstetter
Second Poster Prize, Jahrestagung GDCh Fachgruppe Nuklearchemie 2022, Bergisch Gladbach, Germany, October 04 – 06, 2022

Doctoral thesis

Mario Veicht (EPFL)
Towards implementing new isotopes for environmental research: Redetermination of the ^{32}Si half-life
Dr. Dorothea Schumann (PSI)
Prof. Dr. Andreas Pautz (PSI & EPFL)
July 13, 2022 (oral exam), September 30, 2022 (public defense)

Chiara Favaretto (ETHZ)
Development of Terbium Radioisotopes Towards Clinical Theragnostics Applications in Nuclear Medicine
Dr. Nicholas van der Meulen (PSI)
Prof. Dr. Roger Schibli (ETHZ)
December 14, 2022

Master thesis

Edoardo Renaldin (Politecnico di Milano, Italy)
Cyclotron production of Tm-167 for medical applications
Dr. Zeynep Talip (PSI)
Prof. Dr. Mario Mariani (Politecnico di Milano, Italy)
April 28, 2022

Bachelor thesis

Balàzs Szekér (ETHZ)
Distribution of Terbium in Intermetallic Tb-Pd produced via Coupled Reduction
Dr. Emilio Maugeri (PSI)
Prof. Dr. Anna Soter (ETHZ)
February 14 - June 03, 2022

Internships and Semester projects

Jasmin Huber (ETHZ)
Systematic Studies of Molecular Plating of Gadolinium
Dr. Emilio Maugeri (PSI)
Prof. Dr. Patrick Steinegger (PSI/ETHZ)
September 09 – December 20, 2022

Vladislav Zobnin (Institute for Nuclear Research (INR), Moscow, Russia)
Ion-imprinted resins for a $^{44}Ti/^{44}Sc$ generator
Dr. Đjorde Cvjetinović
Prof. Dr. Patrick Steinegger (PSI/ETHZ)
August 01, 2022 - January 31, 2023

Grants/funding

Swiss Roadmap for Research Infrastructures 19, titled "IMPACT - Isotope and Muon Production using Advanced Cyclotron and Target technologies" – submitted January 2022, along with Conceptual Design Report. SNSF reviewers awarded it an **A** in all categories (July 2022), recommended for inclusion into the Swiss Roadmap, December 08, 2022, Robert Eichler

EUROpean Laboratories for Accelerator Based ScienceHORIZON-INFRA-2021-SERV-01 (EUROLABS) – approved January 18, 2022, Dorothea Schumann

Mobility Grants, Young Researchers' Exchange Programme – Japan Society for the Promotion of Science (via Leading House ETH Zurich) approved November 01, 2022, Jennifer Wilson

Advanced Nuclear Safety Evaluation of Liquid Metal Using Systems HORIZON-EURATOM-2021-NRT-01 (ANSELMUS N. 101061185), funded September 2022, Robert Eichler & Rugard Dressler

Courses attended

C. Favaretto
TERACHEM 2022 International Summer School, Bressanone, September 12 – 14, 2022

P. V. Grundler
Schulung Neue Begleitende Person für Gefahrguttransporte, July 13, 2022
ASI-seminar (DIE ZÄHMUNG DES «HÖLLISCHEN PROTEUS» – Die Stilllegung eines Forschungsreaktors am PSI), February 15, 2022

Visiting guests

Frederic Juget (IRA/CHUV, Lausanne, Switzerland)
Calibration experiment of ionization chambers with ^{44}Sc using different geometries, along with half-life determination, April 01, 2022 & July 26, 2022

Marian Meckel, Mark Harfensteller, Carina Dirks-Fandrei, Konstantin Zhernosekov (ITM, Garching, Germany)
Laboratory/facility visit, along with collaboration discussion. October 26 – 27, 2022

Greg Severin (MSU, East Lansing, USA)
PSI colloquium: *Isotope Harvesting at the Facility for Rare Isotope Beams*, September 30, 2022

Gil Bodmer (Kantonsschule Freudenberg, Zürich, Switzerland)
Introduction into Analytical Chemistry and Research Goals of the Isotope and Target Chemistry Group (Berufspraktikum), February 7 – 11, 2022

Ana Maria Ivan (RATEN-ICN, Mioveni, Romania)
Improving the capacity for long term safe management of radioactive waste and spent nuclear fuel, Training in methods for the study of volatilization of radionuclides from liquid metals (IAEA Fellowship No. 2105664 within the TC project ROM 9038), September 01, 2022 – February 28, 2023

Presentations in LRC seminars

Tejpreet Kaur (Panjab University, India)
Investigating the origin of short-lived radionuclides in the Early Solar System with Galactic Chemical Evolution
October 14, 2022

Steffen Happel (Triskem International, France)
Application of extraction chromatography to the separation of radionuclides from irradiated samples
Mar 18, 2022 (online)

Ondrej Benes (Joint Research Centre, Belgium)
Fuel behavior studies at JRC Karlsruhe
June 10, 2022 (online)

Evgeny Tereshatov (Texas A&M University, USA)
Radiochemistry at Texas A&M University
November 4, 2022 (online)

Affiliation index

AEC-LHEP	Laboratory for High energy Physics, University of Bern, Sidlerstrasse 5, 3012 Bern, Switzerland
ANL	Argonne National Laboratory, 9700 S Cass Ave, Lemont, IL 60439, USA
CERN	Centre Europeen de Recherche Nucleaire, Espl. des Particules 1, 1211 Meyrin, France
EPFL	École polytechnique fédérale de Lausanne, Route Cantonale, 1015 Lausanne, Switzerland
ETHZ	Eidgen. Technische Hochschule Zürich, 8092 Zürich, Switzerland
FRIB/MSU	Facility for Rare Isotope Beam, Michigan State University, 640 South Shaw Lane, East Lansing, USA
IGFAE	Instituto Galego de Física de Altas Enerxías - Campus Vida, Universidade de Santiago de Compostela, E-15782 Santiago de Compostela, Spain
ILL	Institut Laue-Langevin - 71 avenue des Martyr, CS 20156, 38042 GRENOBLE Cedex 9 - France
IRA	Institute de radiophysique, Rue du Grand-Pré 1, 1007 Lausanne, Switzerland
IRB	Ruđer Bošković Institute, Bijenička cesta 54, 10000 Zagreb, Croatia.
Nesca	South African Nuclear Energy Corporation, P.O Box 582, Pretoria 0001, South Africa
LLNL	Lawrence Livermore National Laboratory, 7000 East Ave, Livermore, CA 94550, USA
LNS-INFN	Istituto Nazionale di Fisica Nucleare - Laboratori Nazionali del Sud, Banchina 19, Via Cardinale Dusmet, 175, 95121 Catania, Italy
PSI	Paul Scherrer Institut, Forschungsstrasse 111, 5232 Villigen PSI, Switzerland
PTB	Physikalisch-Technische Bundesanstalt, Bundesallee 100, 38116 Braunschweig, Germany
RATEN-ICN	Regia Autonoma Tehnologii Pentru EnergiaNucleara, Institutul de Cercetari Nucleare, Campului Street No.1, Mioveni City, Arges County 115400, Romania
SCK CEN	Research Centre Mol, Boeretang 200, 2400 Mol, Belgium
SenSiC	SenSiC GmbH, Park Innovaare, deliveryLAB, 5234 Villigen, Switzerland
SpiezLab	Spiez Laboratory, Austrasse, 3700 Spiez, Switzerland
TAMU CI	Cyclotron Institute, Texas A&M University, College Station, TX 77843, USA
TAMU Chem	Department of Chemistry, Texas A&M University, College Station, TX 77843, USA
TUBAF	Technische Universität Bergakademie Freiberg, Akademiestraße 6, 09599 Freiberg, Germany
UniBern	Departement für Chemie und Biochemie, Universität Bern, Freiestr. 3, 3012 Bern, Switzerland
UNIFE	University of Ferrara, Via Savonarola, 9, 44121 Ferrara FE, Italy
UNIO	University of Osaka, 1-1 Yamadaoka, Suita, Osaka 565-0871, Japan
UPit	University of Pitesti, Str. Târgul din Vale nr. 1, Pitești 110040, Romania
USC	Praza do Obradoiro, 0, 15705 Santiago de Compostela, A Coruña, Spain
UZ	University of Zagreb, Trg Republike Hrvatske 3, 10000, Zagreb, Croatia

Paul Scherrer Institut :: 5232 Villigen PSI :: Switzerland :: Tel. +41 56 310 21 11 :: Fax +41 56 310 21 99 :: www.psi.ch